Summer 2014

# Numerical Analysis of Biodiesel Combustion in a Direct Injection Compression Ignition Engine

Kyle D. Morse

NUMERICAL ANALYSIS OF BIODIESEL COMBUSTION IN A DIRECT INJECTION COMPRESSION IGNITION ENGINE

by

KYLE DEVON MORSE

(Under the Direction of Cheng Zhang)

**Abstract**

In this work, simulations of the combustion reaction within an optical Sandia/Cummins N14 direct-injection compression ignition engine are conducted. First, validation of the spray model against liquid and vapor penetration data was conducted using a trial and error method. Secondly, the overall engine model was validated against pressure and temperature data across high and low temperature combustion regimes. The third phase of the work was focused on creating a combustion model for biodiesel. The fourth and final phase was to test the biodiesel combustion model in the pertinent combustion regimes. The agreement with common trends in emissions of biodiesel combustion models were only verified in a few cases. Negative changes in combustion quality, based on fundamental differences in fuel physical properties, were reflected in the combustion characteristics of biodiesel. The negative effects of biodiesel fuel impingement on the piston and wall, as a result in high viscosity fuel nozzle flows, accurately throttled the combustion process. Overall comparison indicates that the interplay of the spray, collision, breakup, and autoignition models must be further understood to improve the accuracy of predictions.

INDEX WORDS: Biodiesel, Emissions, Computational, Fluid, Dynamics, Combustion

# NUMERICAL ANALYSIS OF BIODIESEL COMBUSTION IN A DIRECT INJECTION COMPRESSION IGNITION ENGINE

by

**Kyle D. Morse**

B.S., Georgia Southern University, 2009

A Thesis Submitted to the Graduate Faculty of Georgia Southern University in Partial Fulfillment of the Requirements for the Degree

MASTER OF SCIENCE

STATESBORO, GEORGIA

2014

# NUMERICAL ANALYSIS OF BIODIESEL COMBUSTION IN A DIRECT INJECTION COMPRESSION IGNITION ENGINE

by

KYLE MORSE

| | |
|---|---|
| Major Professor: | Cheng Zhang |
| Committee: | Aniruddha Mitra |
| | Shaowen Xu |

Electronic Version Approved:
June 2014

## ACKNOWLEDGMENTS

I would like to thank my advisor Dr. Cheng Zhang for his extensive assistance during my research. I thank Pawel Gronowski for the introduction to Linux. I thank Mr. Andrew Michaud for sharing some of his knowledge about clusters and computing technology, in general. I'd also like to thank Dr. Annirudha Mitta and Dr. Shaowen Xu for sharing their knowledge in engineering topics over the years, their insight, and their work as my committee members. I can't forget Dr. Brian Vlcek, Dustin Gaddis, Parker Bussey, the man now known as "Ish The Engineer", Richard Stone, and Philip Lee for introducing me to Eagle Motorsports and Formula Society of Automotive Engineers (FSAE). There are other tens of experiments and projects that got rolling because of the influence of the Eagle Motorsports project. I would also like to thank Spencer Harp, Chris Davis, Noel Murray, for all of the help throughout the years. The EMS07, EMS08/09R, EMS10TR, EMS11R, EMS12R, EMS13R, and EMS14R have brought many people into the fold of engineering.

# TABLE OF CONTENTS

## LIST OF TABLES

## LIST OF FIGURES

## NOMENCLATURE

| | |
|---|---|
| AHRR | Apparent Heat Release Rate |
| AMG | Algebraic Multi-grid |
| ATDC | After Top Dead Center |
| CAD | Crankshaft Angle Degrees |
| CFD | Computational Fluid Dynamics |
| CI | Compression Ignition |
| CME | Canola Methyl Ester |
| $C_p$ | Specific Heat (J/kg*K), |
| CSME | Cotton Seed Methyl Ester |
| DI | Direct Injection |
| EGR | Exhaust Gas Recirculation/Residual |
| EVC | Exhaust Valve Closing |
| EVO | Exhaust Valve Opening |
| FAAE | Fatty-Acid Alkyl Ester |
| FAME | Fatty-Acid Methyl Ester |
| FOME | Fish Oil Methyl Ester |
| GVWR | Gross Vehicle Weight Rating |
| HCCI | Homogeneous Charge Compression Ignition |
| HPCC | High Performance Computing Cluster |
| HTC | High Temperature Combustion |
| IMEP | Indicated Mean Effective Pressure |
| IVC | Intake Valve Closing |
| IVO | Intake Valve Opening |
| LTC | Low Temperature Combustion |
| NHTSA | National Highway Traffic Safety Administration |
| P | Pressure |
| PCCI | Premixed Charge Compression-Ignition |
| PISO | Pressure Implicit with Splitting of Operators |
| PPM | Parts Per Million |
| RCCI | Reactivity Control Compression Ignition |
| RME | Rapeseed Methyl Ester |
| SCORE | Sandia Compression-Ignition Optical Research Engine |
| SI | Spark Ignition |
| SIMPLE | Semi-Implicit Method for Pressure-Linked Equations |
| SME | Soy Methyl Ester |
| SNL | Sandia National Laboratory |
| SOI | Start of Injection |
| ULSD | Ultra Low Sulfur Diesel |
| USEPA | United States Environmental Protection Agency |

# CHAPTER 1

# INTRODUCTION

## 1.1 Motivation and Objectives

Compression ignition engines are used in many areas to support the logistical activities associated with industry. Diesel powered locomotives and heavy-duty trucks move unprocessed commodities, chemicals, intermediate materials between manufacturing processes, and finished goods to the places in which they are all needed. Diesel also plays a considerable role mitigating the problems of waste management. Heavy mobile equipment moves wastes such as plastics, metals, and wastes to large bailing and compacting machines and other processing equipment. diesel engines also provide most of the shaft power and thermal energy that drives waste processing equipment such as bailers at incineration plants. In the near future, several industrial pollution problems will have to be addressed. It will be possible to reduce some of the relatively high levels harmful emissions from the industrial sectors by using bio fuels. One of the immediately recognizable benefits of biodiesel, which was identified by Toscano and Duca [1], is its non-renewable energy content of less than 3%. The circumstances resulting from the efforts of engine and heavy duty vehicle manufacturers to comply with increasingly more stringent emissions standards around the world and demands of reduced fuel consumption, from governments as outlined by the USEPA[2] and consumers, are the prime motivating factors for this work. The application of computational fluid dynamics (CFD) during the design of medium and heavy-duty diesel engines is the prime focus of this work. After the mid 20th century, industry has always had to acquire many new tools to keep up with customer demands while keeping overall costs relatively low. Most of the preliminary design phase, in

engines, has been accelerated with advancements in computer aided design and mass multinational outsourcing of engine subsystems. Outsourcing and coordinated design with many companies makes numerous prototyping and experimentation, during development, prohibitively expensive as shown by Liang et al. [7]. Given the short duration of the overall product design cycle, the fuel system, engine, exhaust aftertreatment, and other industry partners typically can't use physical prototyping within their operations as well. Some types of experiments are not a viable option for companies trying to develop and apply advanced engine technology currently under development early on in partnership. Most new technologies are reserved for government laboratories only. Numerical simulations of all types including kinematic and dynamic alike are necessary to simulate most aspects of engine operation quickly and efficiently with low cost. The key areas where CFD is widely applied during design iteration are the cooling system heat exchangers, the engine block water jacket, cylinder head lubrication systems, simulation of wall interactions between the piston rings and liner as demonstrated by Kortendijk [3], intake flow, exhaust system flow, and flows occurring throughout the fuel delivery system including the injectors. The macroscopic features of combusting flows are modeled well with basic approaches in CFD as shown by Wang et al. [4] and Belal et al. [5]. Those basic models also allow base calibration of the underlying engine control system models which reduce development time and costs of embedded control software. Felsch [6] In the future, advanced reaction simulation on top of current in-cylinder flows will be used beyond the basic reaction mechanisms for predicting engine power and functional performance even more accurately. CFD models will have to predict more detailed microscopic characteristics of reacting in-cylinder flows, harmful combustion emissions, and help predict fuel consumption across a wide

variety of combustion regimes. CFD combustion models and codes will still have to allow engineers the ability to finely tune more advanced engine control models, maximize engine performance within constraints, and adapt the whole powertrain package to conform to outsourced original equipment requirements. Combustion models with higher numbers of species and higher fidelity will be possible to simulate widely in the future as access to computational resources such as, more specialized open-source codes, compute cloud rental, and cheaper high-performance cluster hardware becomes available to potential customers. Sophisticated solution techniques as used by Liang et al. [7] will also be incorporated into commercial codes as simulation becomes more popular for design.

The objectives of this research work were to:

1. Create a surrogate gas-phase diesel material, which is appropriate for multidimensional numerical simulation in a heavy-duty compression ignition (CI) engine.

2. Compare, with reasonable accuracy, the reduction amount of certain regulated pollutants; which could allow a scaling down of the expensive exhaust aftertreatment systems currently in use.

## 1.2 Overview of Compression Ignition Engines

The Diesel cycle was initially conceived by Rudolf C. K. Diesel in 1893, when he first introduced his thermodynamic theories. He continued to work develop ideas and on his engines until his death in 1913. His goal was to create a new form of heat engine which didn't use steam or spark ignition to initiate combustion. The Diesel cycle is a four stage thermodynamic cycle based originally on the Otto cycle but with a few key changes. The four stages or strokes of the diesel cycle are induction, compression, injection/combustion, and the exhaust strokes. The main differences, particular to the Diesel cycle, are the lack of air throttling, the use of middle distillate fuels, and the employment of direct injection. The intake valve opens (IVO) just before the piston is travels toward the crankshaft during the induction stroke. The intake valve closes near bottom dead center (BDC) and the then piston travels away from the crankshaft. Nearing the end of the compression cycle, the average pressure and temperature is around 50bar to 80bar and 800K to 1100K respectively. Near top dead center (TDC), the injection valve needle lifts and a particular amount of fuel is introduced into the cylinder through the fine orifices. The axes of the several high precision orifices are positioned equi-azimuthally with negative elevation toward the piston crown and cylinder wall liner. The high pressure liquid fuel spray travels radially out in the form of jets. The swirling air deforms the fuel jets and they eventually break up into mists of fine droplets around the jet peripheries. The fine mist of droplets vaporize when shear overcomes surface tension. Since there is no spark plug unlike the Otto cycle, the combustion reaction must ignite automatically. There is enough thermal energy in the air, after compression, to activate the combustion reaction. Ignition occurs automatically when an appropriate air and fuel according to a particular range of stoichiometric ratios is locally

reached near the vaporized droplet. The rapid increase of average cylinder pressure comprises the combustion stroke. The expansion of cylinder volume is driven partially by the thermal and mostly the kinetic energies released during combustion of the charge. The combustion takes place around the crown of the piston. The violent action of the combustion process causes the remaining fuel to be mixed with the leftover air and the increase in cylinder pressure. The energy conversion process is facilitated by the piston, connecting rod, and crankshafts present orientation which is all a function of the crankshaft angular position, which is why injection timing is important. Finally, The exhaust valve opens (EVO) as the piston is moving away from the crankshaft again. At that time, the products of the reaction are expelled from the cylinder. When the operating conditions of the engines are optimum, the combustion process is self sustaining. The entire 4-stroke cycle is completely repeated for every two subsequent rotations of the crankshaft. The Diesel cycle is depicted pictographically, in more detail, within figure 1.

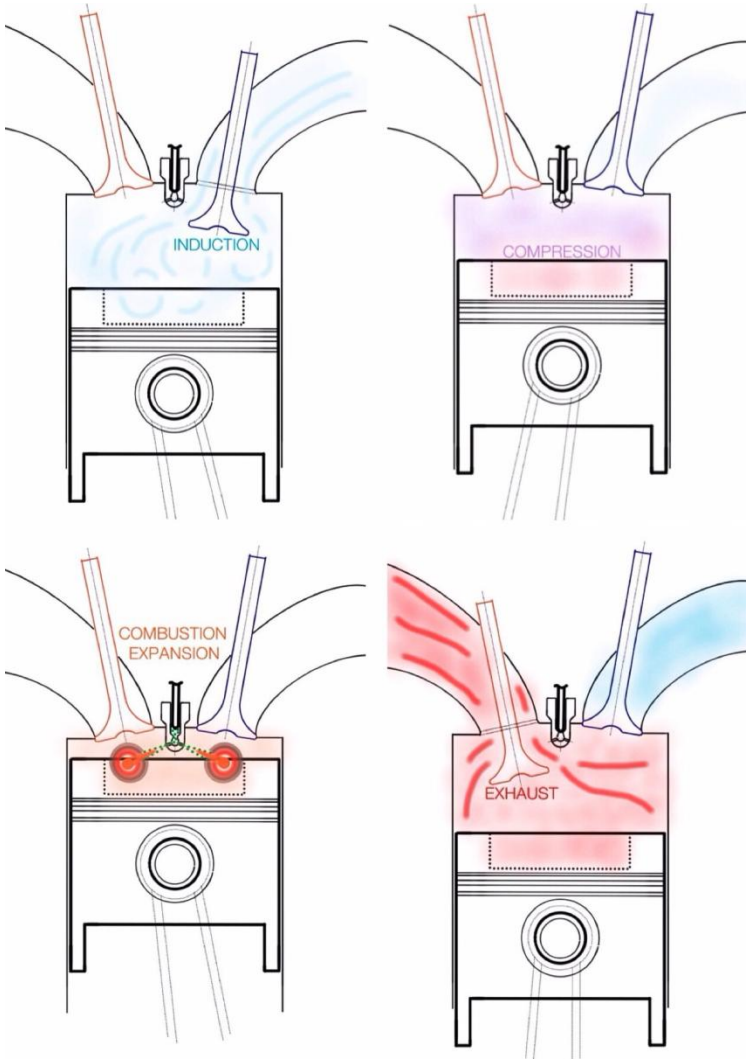


**Figure 1: The 4 strokes of the Diesel cycle.**

The hallmark of the diesel cycle is its relatively high thermal and mechanical efficiencies when compared to other reciprocating internal combustion (IC) cycles such as the Otto, Miller, and Atkinson. The average light to medium duty reciprocating gasoline engine has an overall efficiency of 20%. [8] Diesel engines can, depending on size and intake configuration, can range from 27% to 40%. The largest Diesel engine in the world, the RTA96-C for maritime application, manufactured by Wärtsilä-Sulzer of Finland can reach an overall efficiency of 51.7%. This level of efficiency is reached because of some of the key idiosyncrasies of the diesel cycle. Unlike the Otto cycle, the

atmospheric air inducted to into the engine is not throttled using a butterfly valve upstream of the intake valve situated in the cylinder head. Crankshaft angular kinetic energy, beyond losses imparted from inherent wall friction and fluid internal viscous forces, do not occur in the Diesel cycle because it is not throttled using a butterfly valve. The volumetric efficiency of diesel engines is thus higher because of the absence of those pumping losses. Also, diesel engine compression ratios are not heavily limited by the fuel and other thermomechanical factors as they are in the premixed cycles. Compression ratio is not limited, in common diesel combustion regimes or strategies, because the fuel does not enter the combustion chamber in the premixed condition. Combustion knock, or the sudden detonation of the combustion charge before the ideal cylinder condition and corresponding crankshaft angular position, is not a highly relevant factor in diesel engine design. Overall pressure levels must be kept within ranges appropriate to the particular engine's structural strength. Typically, in reciprocating internal combustion engines, increases in compression ratio correlate with increases mechanical efficiency. [8] Diesel engines rely on the autoignition phenomenon associated with high cetane number fuels, so they can take full advantage of turbochargers. Turbochargers use the wasted kinetic and thermal energy of the exhaust stream to increase the mass of air that reaches the combustion chamber. They have become a common aspect of modern diesel engine design. Turbochargers allow generous increases in combustion torque because of an increase in the mass of air that enters the cylinder. Because of the cylinder pressure levels (>100bar in many turbo-diesel engines), Diesel engines typically have heavy-duty components and relatively larger connecting rod length to crankshaft journal radius ratios, which limit their maximum crankshaft speed. The disadvantages to all this is that Diesel engines

typically operate at fuel lean conditions. The amount of fuel injected into the cylinder controls the crankshaft speed and resistance to load. As engine speed increases with constant load, increasing amounts of fuel are introduced into the cylinder with less time to diffuse into air and combust. Spatially, within the cylinder, there are large variations in equivalence ratio and temperature which provide ideal conditions for the formation of several types of harmful pollutants. The Equivalence ratio is defined as the actual mass ratio of fuel to oxidizer over the stoichiometric ratio.

$$\emptyset = \frac{m_{fuel}/m_{air}}{\left(m_{fuel}/m_{air}\right)_{st}} \quad (1)$$

Medium temperature (900K to 1700K) fuel-rich (Φ>1) regions allow pyrolysis, or breakdown because of high heat without oxygen, of alkanes near the central axis of the fuel jet. Formation of sulfates and carbon particulates absorb intermediary hydrocarbons species leads to sulfuric acid formation and carcinogen exposure. High temperature (1800K to 2800K) fuel lean (Φ<1) regions at the periphery of the of the combusting fuel jet are where oxides of nitrogen form which lead to nitric acid and smog. These regions can be viewed within the cross-section of a fully developed fuel spray. Optically measured nitric oxide and hydroxyl are used to identify the shape and orientation of the jet cross-section as done by Demory [9].

These regions can be viewed within the cross-section of a typical fully developed fuel spray in figure 2.

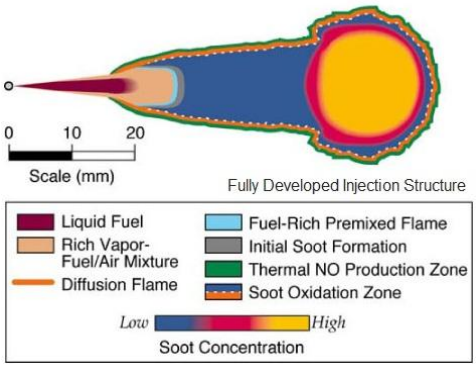


**Figure 2: Fully developed fuel nozzle spray [10]**

The small carbon particles, typically called soot, which are produced by the pyrolysis process leave the cylinder and exit the exhaust systems in large plumes. It is those phenomenon which have precluded Diesel engines in the US from occupying a larger share of the consumer market. [10] Figure 3 is a photograph of a diesel truck accelerating and releasing a large volume of soot.

**Figure 3: Emission of soot while accelerating under load. [11]**

Pollution problems can be minimized with biodiesel fuels and the overall efficiency increased further, diesel engines can be taken advantage of during the quest to reduce the detrimental affects toward the biosphere.

### 1.3 Specifications of the Simulated Engine

Sandia National Laboratory maintains several optical engines specifically redesigned for the study of several regimes of combustion in compression ignition engines. The Sandia/Cummins N14 Compression-Ignition Engine was the focus of this research work. The research engine is a single cylinder DI, 4-stroke Diesel engine based on the Cummins N14 inline 6 engine widely used exclusively in heavy duty on and off-road vehicles. A particular version of the Cummins N14 is depicted in figure 4.


**Figure 4: Cummins N14 heavy duty diesel engine. [12]**

Optical research engines are special because chemiluminescence and laser-induced fluorescents are applied to the analysis of in-cylinder chemical events trough

transparent window near the combustion chamber. The Sandia/Cummins N14 is equipped with several high-strength transparent windows positioned in the piston crown, cylinder wall, and the cylinder head. The highly-augmented piston and head geometries allow high-energy lasers to be aimed into the cylinder for planar laser infrared fluorescence (PLIF). Characteristics of the spray such as liquid penetration length and flame lift off can be visualized can be visualized as fuel is injected and combusts. After post processing, the spray visualization can be viewed alongside average cylinder pressure and injector needle lift.  Analysis of the luminosity data results in the ability to quantify the  formation of methyl radicals (CH), hydroxide (OH), aldehydes, polycyclic aromatic hydrocarbons, and particulate matter (PM). Figure 5 is a depiction of the Sandia/Cummins N14 engine.

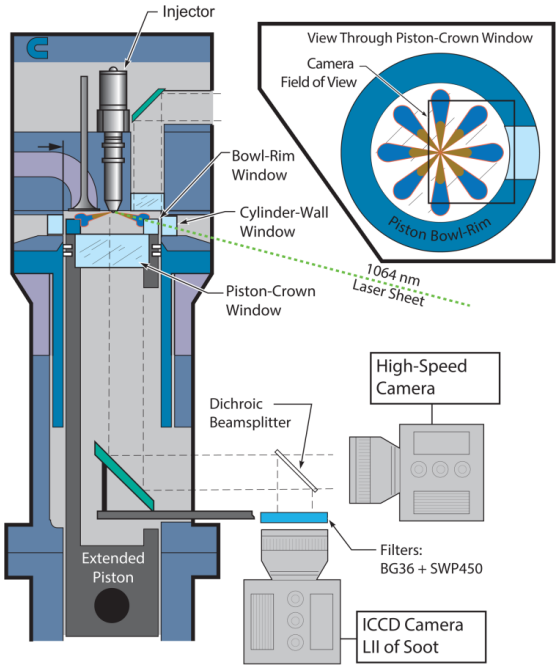


**Figure 5: Sandia/Cummins N14 diagram [13]**

The N14's cylinder head is designed to establish an in-cylinder flow swirl number of 0.52 around TDC. The swirl number is defined as the ratio of the angular velocities of the air swirling around the cylinder to that of the crankshaft.

$$S = \frac{\dot{\theta}_{swirl}}{\dot{\theta}_{crank}} \tag{2}$$

The piston bowl is purely cylindrical so that the index of refraction is not such that the data retrieved from the soot imaging system are not warped. Fuel is only injected once every ten cycles to keep the overall operating temperatures of the engine low. The N14 engine specifications extensively used in this work are summarized in Figure 6.

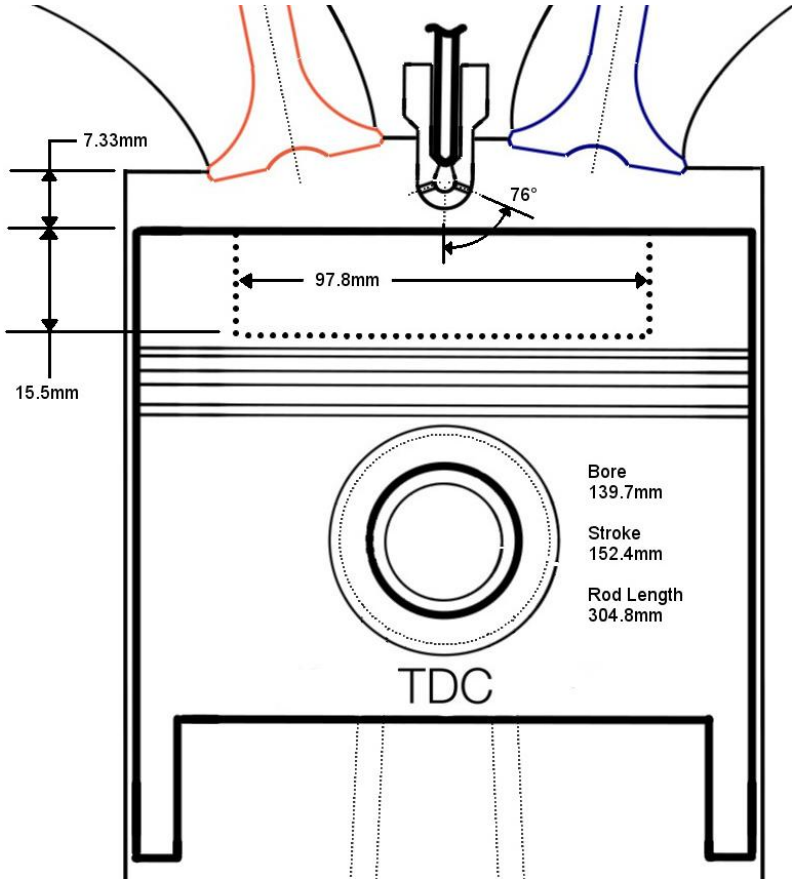


**Figure 6: SCORE Piston geometry**

The Fuel injector is an eight orifice solenoid actuated unit. Typically solenoid driven injectors are not capable of firing multiple injections or altering the injection rate several times during the spray. The nozzles are declined 14˚ away from the cylinder head and spaced 45˚ apart circumferentially. The geometry and pressure settings are listed in table 1

**Table 1: Sandia/Cummins N14 engine specifications**

| Sandia/Cummins N14 Engine Specifications | |
|---|---|
| Base | Cummins N-14, DI Diesel |
| Bore x Stroke | 139.7mm x 152.4mm |
| Connecting rod length | 304.8mm |
| Piston bowl profile | Cylindrical |
| Bowl width, depth | 97.8mm, 15.5mm |
| Squish Distance | 7.33mm |
| Compression ratio | 11.2:1 |
| Number of cylinders | 1 |
| IVC | 540° APTDC |
| EVO | 845° APTDC |

High-temperature and low-temperature combustion regimes have been extensively tested in the Cummins N14 engine by Singh [11]. The doctoral research work of Singh focused on petroleum diesel fuel exclusively while validating several KIVA combustion models against experimental data. There was also an extensive focus on processing data signals from the array of sensors used to visualize in cylinder events. Combustion conditions were arrived at by altering injection timing and fuel mass amount. Exhaust gas recirculation was simulated by reducing the volumetric concentration of oxygen in the intake air stream by controlling nitrogen content. The various engine operating conditions focused on during this work are summarized in Table 2

**Table 2: Sandia/Cummins N14 operating conditions**

| N14 Operation States | High-T Short-ID | High-T Long-ID | Low-T Early-Inj | Low-T Late-Inj | Low-T Double-Inj |
|---|---|---|---|---|---|
| **$O_2$ Volume (%)** | **21** | | **12.7** | | |
| **Intake Temperature (K)** | 384 | 320 | 363 | 343 | 363 |
| **Temperature at BDC (K)** | 379 | 335 | 365 | 351 | 365 |
| **Initial Absolute Pressure (Pa)** | 233000 | 192000 | 214000 | 202000 | 214000 |
| **Motored Temperature (K)** | 905 | 800 | 870 | 840 | 870 |
| **Motored Density (kg/m$^3$)** | 24 | 22.3 | 22.9 | 22.5 | 22.9 |
| **Injection Pressure (MPa)** | **120** | | **160** | | |
| **SOI BTDC (CAD)** | 7 | 5 | 22 | 0 | 22, +15 |
| **DOI(CAD)** | 10 | 10 | 7 | 7 | 4, 4 |
| **Injected Quantity(kg)** | 6.1E-05 | | 5.6E-05 | | 3.1E-5, 3.3E-5 |
| **Peak Adiabatic Temp (K)** | 2760 | 2700 | 2256 | 2164 | 2132 |
| **Speed (RPM)** | **1200** | | | | |
| **IMEP (bar)** | 4.4 | 4.5 | 3.9 | 4.1 | 4.5 |

### 1.4 Future Emissions Standards in the US

The size range and applications for Diesel engines vary across off-road, on-road, and marine use. The modern applications of Diesel engines includes small-scale power generation, medium-scale power generation, light off-road equipment, medium off-road equipment, heavy off-road equipment, light-duty on-road vehicles, medium-duty on-road vehicles, locomotives, and all types of marine applications including pumping. The United States (US) Environmental Protection Agency (EPA) utilizes a system for classifying on-road engines by the model year and gross vehicle weight rating (GVWR) under tiers. The allowable Emissions from heavy-duty Diesel-fueled engines in the US have been on a consistent decline over the last 42 years as can be seen in figure 7. The emissions regulations on smaller vehicles are greater in number and tend to be more sophisticated. Between model years 1991 and 1997, the standards for vehicles up to

6,000lbs were initially established by using Federal Test Procedure 75 for highway driving. A supplemental test procedure was developed to further constrain highway emissions based on aggressive highway driving. Tier two was adopted in December of 1999 for the purpose of making entire fleets of manufactured vehicles fall under an average allowable emission quantity over regulated useful lifetimes with warrantees. Tier three, proposed in March of 2013, is an attempt to apply California's low-emission vehicle three (LEV III) standards at a federal level.

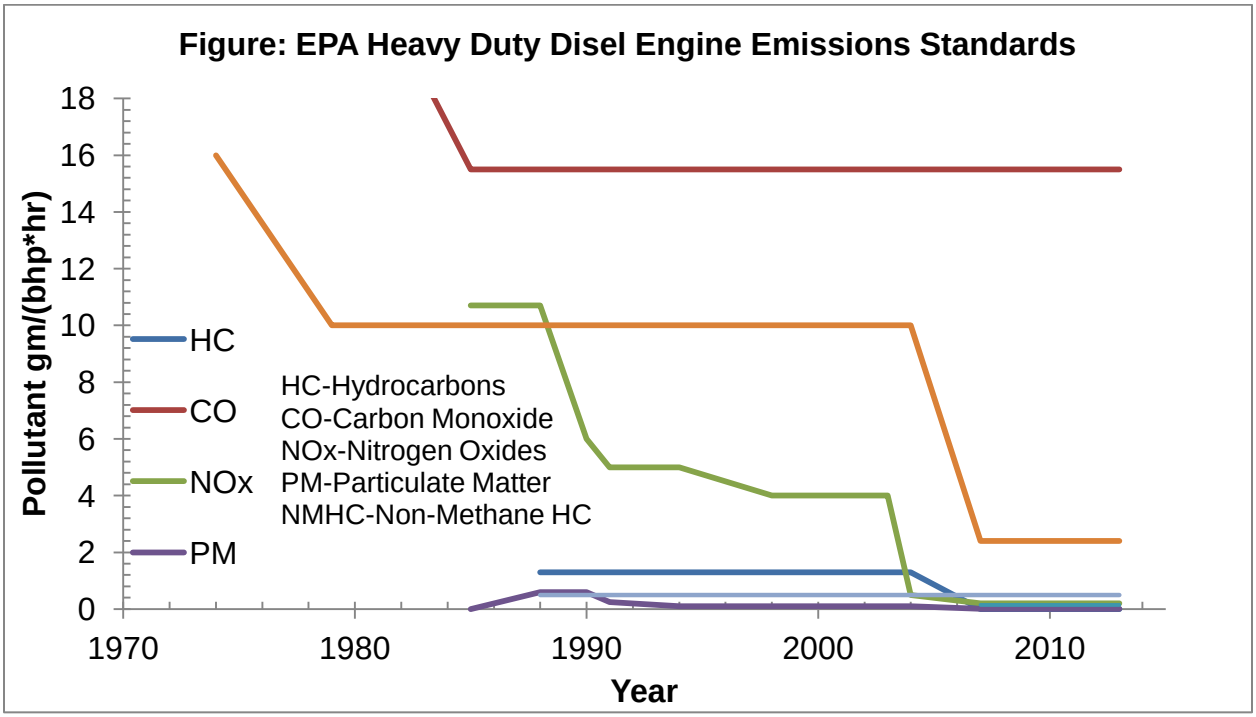


**Figure 7: US EPA allowable heavy duty diesel emission levels**

The reduction of regulated emissions output per engine comes after the introduction and mass implementation of several fuel and exhaust treatment technologies at various levels within the industrial and transportation technology sectors. Systems that have been implemented on most modern diesel engines for the reduction or elimination of harmful chemicals within high-temperature exhaust gas. Up until recently, the primary

focus of engine development was the maintenance and insurance of critical system performance.

The EPA and National Highway Transportation Safety Administration have both introduced new standards for the 2014 model year and beyond. The EPA NHTSA joint Heavy Duty program consists of pollutant and fuel mileage standards respectively. It is estimated that the plan will reduce $CO_2$ emissions by 270 million metric tons and save 530 million barrels of crude oil from 2014 to 2018. Up to 92 billion US dollars could be saved in fuel and technology costs. The standards for the greenhouse gas (GHG) $CO_2$ and fuel consumption are specifically for tractor-trailers or combination tractors of specific weight classes, cab types, and cabin roof heights. The standards are based on payload weight and will eventually reduce GHGs and fuel consumption by up to 23 percent in 2017. The proposed GHG and fuel consumption standards are shown in Table 3.

**Table 3: Typical EPA/USDOT emission and mileage standards beyond 2014**

| **Final (Model Year 2017) Combination Tractor Standards** | | | | | | |
|---|---|---|---|---|---|---|
| **Category** | **EPA $CO_2$ Emissions** | | | **NHTSA Fuel Consumption** | | |
| | g/ton-mile | | | gal/1,000 ton-mile | | |
| | **Low Roof** | **Mid Roof** | **High Roof** | **Low Roof** | **Mid Roof** | **High Roof** |
| Day Cab Class 7 | 104 | 115 | 120 | 10.2 | 11.3 | 11.8 |
| Day Cab Class 8 | 80 | 86 | 89 | 7.8 | 8.4 | 8.7 |
| Sleeper Cab Class 8 | 66 | 73 | 72 | 6.5 | 7.2 | 7.1 |

To see the implications of these standards, If a sleeper cab class 8 combination tractor with a low roof on I-16 is traveling from Savannah, Georgia to Macon, Georgia ,

with a load of 50,000lbs, and an average fuel consumption rate of 5 mi/gal, the truck will burn around 33 gallons of diesel fuel. In 2017, the truck will only be able to consume around 27 gallons of diesel over those 167 miles. To save six gallons of fuel and meet still $NO_x$ emissions standards while also not running the engines hot is a very difficult challenge with the current system of using high-temperature combustion and advanced aftertreatment systems. The future cost of aftertreatment systems will prohibit the current style of diesel combustion. Figure 8 is a depiction of the current array of aftertreatment systems included on most Tier 4 and heavy-duty, on-road diesel vehicles with staged turbo charging.

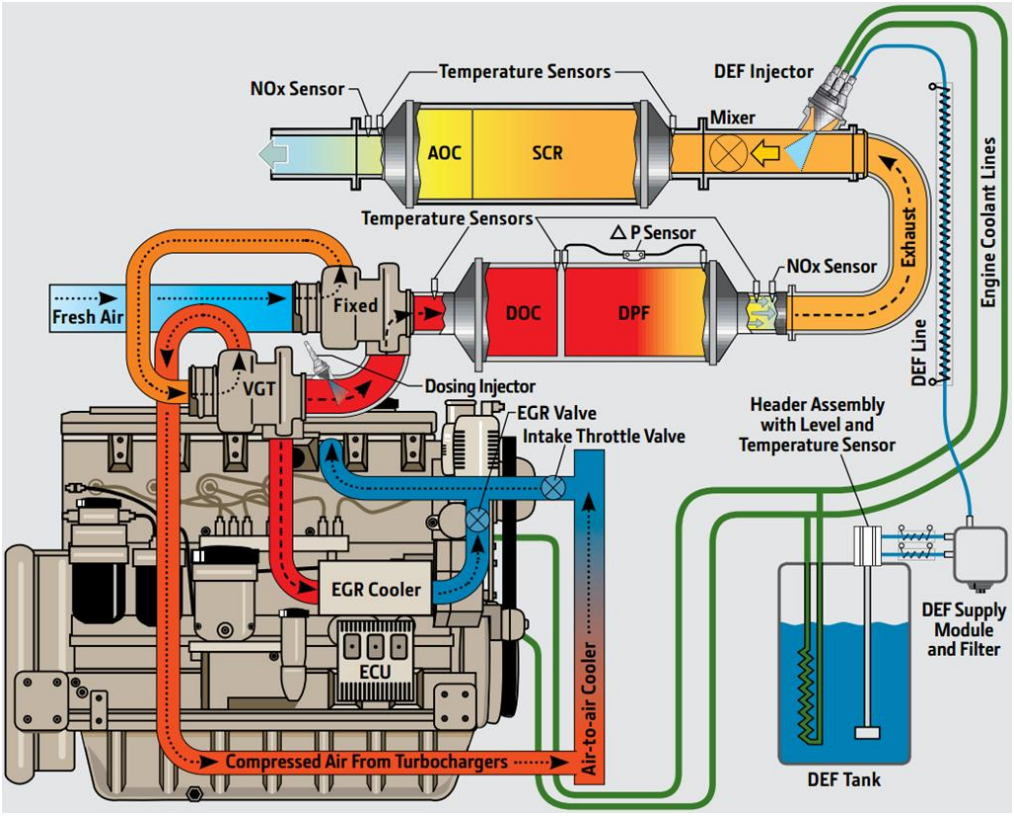


**Figure 8: EPA Tier 4 exhaust aftertreatment system. [14]**

Diesel exhaust fluid (DEF) systems are the latest addition to aftertreatment systems. A mixture of urea and water is injected into the exhaust stream in order to form ammonia and combine with NOx. The ammonia and NOx are mostly converted to nitrogen gas and water vapor within an ammonia oxidation catalytic (AOC) conversion device using selective catalytic reduction (SCR). Even before the AOC, the exhaust stream is run through a diesel oxidation catalyst (DOC) and diesel particulate filter (DPF) system. The after treatment systems basically either filter out or convert all regulated pollutants in the exhaust stream to $CO_2$, $H_2O$, $N_2$, and CO. Alternatives to conventional HTC will allow many components within the current typical aftertreatment system to be either scaled down or eliminated. Scaling down or elimination of certain aftertreatment component parts will also reduce exhaust system maintenance and overall cost. The current alternatives to conventional HTC are low temperature combustion (LTC), homogeneous-charge compression ignition (HCCI), and reactivity-controlled compression ignition (RCCI). The short term solution to the engineering problems provided by regulations always affect the long term solution because of massive organizational inertia. A combination of alternative combustion and reformulated fuels will be necessary to circumnavigate the short comings of diesel.

## 1.5 Biodiesel as an Alternative Fuel

Currently, many state-level, federal, and corporate level currently operate their heavy duty diesel distribution fleets using internally produced biodiesel blends. The US Foodservice corporation operates a program called Fuel Good. Waste cooking oil from customers is collected during shipments drop offs. This oil is processed to produce over

58 million tons of biodiesel annually according to Alptekin and Canakci [12]. Figure 9 is a picture of a Fuel Good shelf which is placed behind the US Foodservice customer's business.


**Figure 9: US Foodservice Fuel Good used cooking oil**

Individuals have been producing small personal batches biodiesel for low volume use from waste plant oils. Many of the restaurants local to them offer waste cooking free of charge. The basic process of producing biodiesel involves very simple equipment that can be purchased on the internet and the process can be done relatively cheaply. The costs of proper waste cooking oil disposal is often higher than freely allowing individuals to periodically remove it from the premises. Homebrew biodiesel production is popular because a small amount of attention to detail generally and repeatedly results in usable fuel. There are vehicles and equipment that require absolutely no modifications to operate safely on biodiesel such as cars or buses.

The typical process of biodiesel production starts by filtering feedstock oil and removing water by heating it to 170 degrees Fahrenheit. The oil must be titrated to measure its acidity before going forward with the manufacturing process. A catalyst, typically a strong base (pH > 7) such as potassium hydroxide, is needed for the batch and the presence of water in the feedstock is detrimental to the formation of biodiesel. The base must first be dissolved into an alcohol such as methanol. The titration process results are also an indicator of the level of free fatty acids or monoglycerides in the feed stock. Water in the feedstock oil, at the point where the base and methanol mixture is added to the feedstock, will cause hydrolyzation in the presence of monoglycerides and a corresponding amount of detergent or soap will be produced with the biodiesel. Transesterification is allowed to take place in a column. After the esterification reaction rate has had enough time to fall, glycerol is extracted from the bottom of the column after it has settled to the bottom. The final product after each of the three major biodiesel production stages is depicted in figure 10.


**Figure 10: Biodiesel from feedstock to finished B100**

Moser [16] studied the basics biodiesel manufacturing and identifies many of the feedstocks, bases, and alcohols which can be used to produce many of the popular types of methyl esters. A typical transesterification reactor system with a medium sized column is shown in figure 11.


**Figure 11: Biodiesel transesterification reactor. [17]**

Georgia lies within the South East EPA region enumerated as area four. Several municipalities and private organizations have come together to form the Southeast Diesel Collaborative at http://www.southeastdiesel.com within region four. The organization is part of the National Clean Diesel Campaign and its goal is to combine regulatory measures with voluntary initiatives to reduce pollution emitted from Diesel engines. It introduces technology and methods to operators of public fleets, freight operating private individuals, and operators of non-road diesel powered equipment. The

focus of guaranteed and potential customers of near future (2014-2018) diesel technology is being guided by the information that is accessible to them. Engine and equipment manufacturers have to guide their development between meeting EPA regulations and conforming to the fuel use and cost wishes of their customers. Ultimately, the technical specifications of the new generation of diesel technology will be decided by the engineering and manufacturing departments of companies involved in the Diesel engine industry. In the area of alternative fuels, those engines and the, emissions control regimes packaged with them will need to be very versatile as the chemical makeup, quality, and quantity of biodiesel and blends of it vary across EPA regions. The Diesel engine is very versatile when it immediately comes to the actual fuel but, fuel of low quality, in the long run, can damage the fuel lines, lift pump, injection pump, injectors, and aftertreatment systems. Because of the widely varying chemical and physical specifications of biodiesel, the American Society for Testing and Materials (ASTM) and the European Committee for Standardization (CEN) have come up with standards for 100 percent biodiesel by volume (B100) and blends of it with various grades of diesel. The ASTM has developed and published the D6751 family of physical property standards for pure biodiesel itself. The 13th edition of the standard specifically target the physical properties of biodiesel that, if out of range, can negatively affect the previously stated engine subsystems. Energy companies that offer blends of EPA ultra-low sulfur diesel (ULSD) at the pump and fatty-acid alkyl ester (FAAE) already ensure that their fuels conform to the ASTM D975-13 standard.

The large chemical and qualitative variety of biodiesel directly stems from the fact that it is can be manufactured from a large number of glycerides, alcohols, use various

transesterification methods, and bases. In the long run, the main challenge for engine designers is the identification of the appropriate type of biodiesel or blends to work with. There will come a period when injectors, injection strategy, combustion characteristics and piston bowl geometry will need to be redesigned to maintain performance, increase performance, and meet emissions and fuel consumption standards. There always has to be a balance between the solutions that alleviate emissions requirements issues, fuel consumption, and performance problems such as nozzle cavitation and customer or market wide satisfaction levels. Problems such as the food vs. fuel situation really only apply to a situation where there is a large scale production operation that utilizes virgin oil straight from field plant sources as feedstock. High quality biodiesel has been manufactured in large volumes using algae cultures and hemp oil as shown by Li and Wan [4]. Hemp's similarities to marijuana or cannabis, preclude it from being produced in the US. Currently, at the mass consumer level, a large volume of consistent blends of feedstock oils are needed along with a continuous production process instead of high volume batches. A mass movement to biodiesel really only requires that the selected oil and alcohol sources have high yield per acre if land is used to produce the feedstock and chemicals. There are several other plant-based fuel sources such as cotton seed oil (CSME) as tested by Keskin et al. [19]. More advanced transesterification methods such as ultrasonication have been developed for high volume continuous production. Singh and Singh [16] investigated several other methods of making biodiesel using 51 plant oils. Figure 12 is a diagram of a continuous flow system with an ultrasonic agitator. Reclamation of alcohols and reprocessing of other byproducts is used in commercial reactors to increase production efficiency and reduce wastes. Knothe et al. [21] overviews the logistics of quality control during mass production.

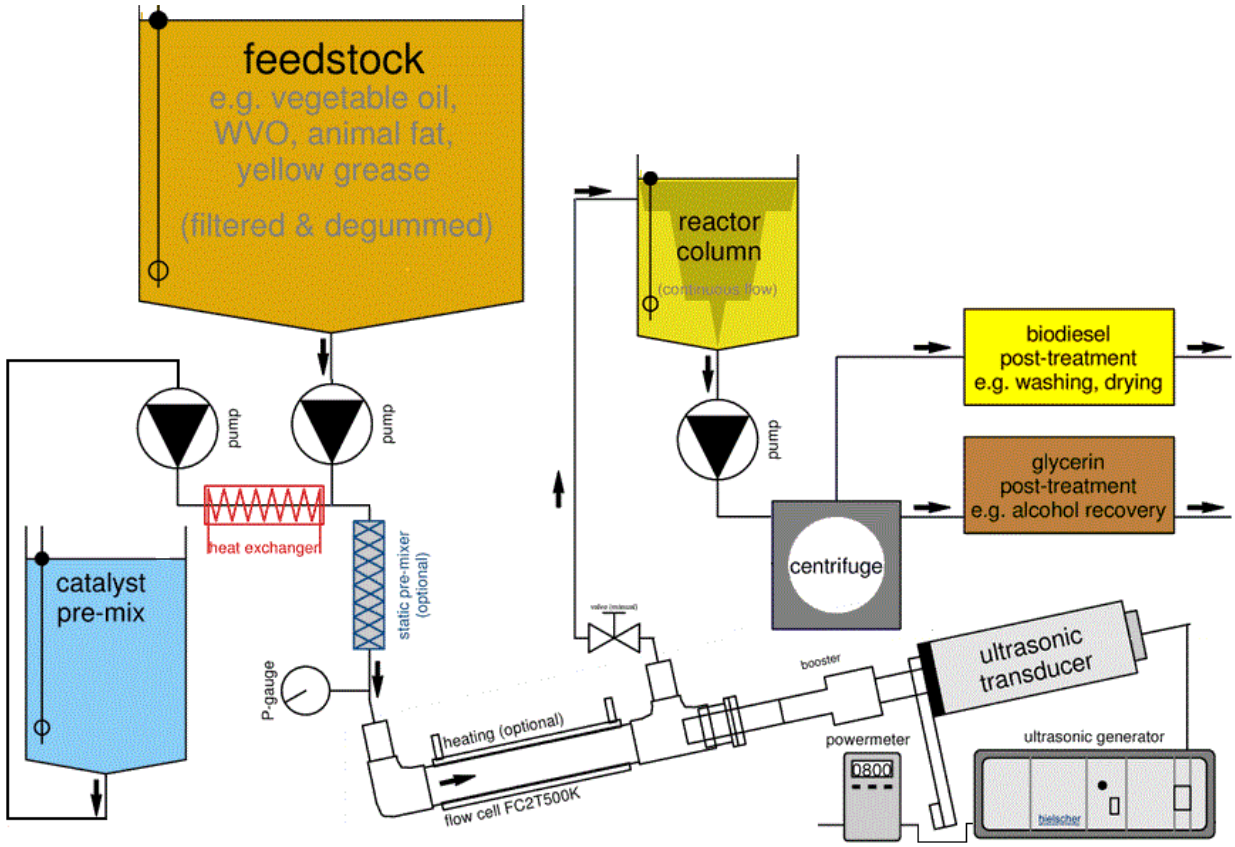


**Figure 12: Continuous biodiesel ultrisonification reactor**

Another continuous flow method, under development, is the membrane reactor discussed by Cao et al. [18]. The main feature of the membrane reactor is the ability to produce FAME with glycerin levels below the ASTM D6751-13 standard in one reaction step without washing afterward.

### 1.6 Scope of Computational Fluid Dynamics Simulation

The governing equations for fluid flows are all derived forms of the mass conservation laws, Newton's laws, and the laws of thermodynamics. They are stated in a continuous differential form and describe the rules for several continuous functions within the domain volume that is defined by a set of intersecting surface equations. Pressure terms are in the equations but there is no equation for pressure beyond

several sets of equations of state found elsewhere. With real world applications like pumps, aircraft, and engines, there is no analytical solution for the systems of equations which partially describe flows within and around those systems. There are several types of CFD solvers but the most robust and widely used type are the ones which using the finite volume method. To 'solve' the differential equations, they must be reformulated into volume and surface integral forms, the flow domain must be discretized by splitting it into finite volumes, and time also needs to be discretized. The discretization of the continuous domain is referred to as grid generation or meshing. The numerical methods, used in CFD, can now be applied because application of the integral equations to the mesh grid cells transforms the derivatives and integrals into algebraic terms. Iterative and interpolation techniques are then applied to the algebraic equations to estimate the value of the scalar variables at the cell centers and derivatives at the faces respectively. The values of conserved variables at the cell faces have to be interpolated using the cell center data. Because the mesh elements, or cells, can be made into a variety shapes and the tetrahedron and hexahedron are the most common. The selection of the spatial discretization scheme is important for convergence. Vectors such as gradient and velocity terms in the equations are typically computed using Green-Gauss methods. If the overall system and configuration parameters presented to the solver are sound, the residual inequalities between cells have a high probability of eventually stabilizing and being reduced within specified allowable limits. The case is then taken to be converged and the computation of the variable estimations ceases. The converged results can then be post processed to generate visual information such as contour and vector plots. Scalar and vector quantities such as the pressure or velocity through the domain can be visualized across time after post processing of

solution data at each timestep of a transient case. Validation can be carried out with comparison of images and the use of globally applied statistical methods to compare results to experimental data in graph form.

During operation of the Sandia/Cummins N14 engine, a crankshaft angular velocity of 1200 RPM is typically maintained. Each stroke takes place in around 21.9 milliseconds at 1200 RPM. As that time passes, turbulent air swirling around the cylinder, at approximately 10.4 revolutions per second, has had its temperature increase by 526˚C from 100˚C. At standard high temperature operating conditions for the Cummins N14, 81˚C fuel is injected at around 120 MPa through the eight 196μm nozzle orifices. The liquid fuel exits the orifices at approximately 530 meters per second. Cavitation occurs circumferentially along the walls of the injection orifice bores which lower their effective cross-sectional area by around 30% which increases the injection velocity to such a speed. Spray formation consists of the liquid jet of fuel breaking up into a series of ligaments and nano droplets due to shear and drag forces. Interaction with high temperature turbulent air causes a secondary breakup. Relatively large droplets that occupy the center of the spray continue to break up due to continual drag forces overcoming surface tension forces within the droplets. Premixed combustion with a high equivalence ratio occurs locally when droplets, that are about 10μm in diameter, start to vaporize about 0.5 milliseconds from the start of injection (SOI). Because the initial combustion starts around 27 millimeters from the injection orifices, and the injector sprays for 1.39 milliseconds, a second rich region of diffusion combustion develops and extends out to the edge of the top of the piston bowl. Spray impingement occurs and eddies, consisting of reacting multiphase fluid with high temperature, tumble and

impinge against the head, cylinder wall, and piston leading to surface reactions. Finite oxidation mechanisms, that can accurately resolve the complexity of diesel combustion across all temperature and pressure ranges including autoignition and delay, contain thousands of separate chemical species such as paraffins, aromatics, alkanes, and involve in tens of thousands of reactions taking place within milliseconds.

The main challenge, in the future, is the inclusion of nozzle sprays to the point of making engine simulations multiphase, the associated effects of cavitation within the injection orifice on atomization and impingement will then be directly simulated. Ning et al. [19] have introduced a spray model that incorporates time varying injection phenomenon, such as cavitation using Eulerian methods. The phenomenon of fuel droplet atomization and vaporization takes place over microscopic distances and periods of time on the order of microseconds. The injection of liquid fuel into the domain occurs at high velocity. The resulting spray formation, penetration, and reaction means that the spatial mesh grid must be more dense and the time step value be decreased beyond current computing capabilities if multiphase interaction is considered. The large velocity field characteristics of the flow, such as overall swirl and tumble of bulk air, may not necessarily need a relatively large dedication of computational resources to be resolved but, they are heavily affected by thermal energy and radiation coming from the combustion processes and heat transfer into engine part surfaces. Modeling heat transfer during the combustion process makes simulation more difficult because of scalar species conservation, energy, combustion, and energy equation coupling is steered by specified lists of conserved species according to mechanism reactions. When gas-phase kinetics are considered, the mass fraction of each chemical

species is considered to be a conserved scalar. Consideration of kinetics results in each cell having an additional set of mass and species conservation equations. The mass fraction conservation equation source terms values are decided according to the reaction mechanism. Source terms added into the various energy equations of each cell are also calculated using the reaction mechanism. The various source terms heavily couple several of the separate equations together resulting in a highly stiff system of equations for each cell. The difficulty of realistically modeling IC engine combustion chambers, if surpassed, results in new engineering opportunities for optimizing engine part geometry without the large cost of extensive experimentation.

# CHAPTER 2

# REVIEW OF LITERATURE

## 2.1 Combustion Simulation

### 2.1.1 Gas-Phase Kinetics and Initial Mechanisms

Kinetics is a chemistry research field concerning mathematical modeling of chemical reaction processes. Considerable effort has gone toward developing very detailed gas-phase combustion kinetics modeling. The main area of focus is the initial and subsequent formation of molecules or species after oxidation. Study of the extensive properties of combustible mixtures and intermediary species formation pathways, provides necessary information for the design of reactor vessels and support equipment. Modeling reactions across the wide domain of temperature and pressure can cause some difficulty in the selection of species, selection of reaction stages, and calculation of reaction parameters for three dimensional problems. Kinetics originally applies to zero dimensional well mixed systems concerned only with time. Two dimensional spacial problems, such as plug flow reactors and laminar flame simulations, were eventually added. For diesel engines, cylinder pressure and gas density variation stemming from volumetric compression affect the first steps of combustion significantly. Certain types of burners or common constant flow reactors that operate close to atmospheric pressure can use less advanced mechanisms. Autoignition in diesel engines is complex and can't be expressed with simple mechanisms accurately as can be seen in the work of Sheshadri [20]. Ignition phenomenon are also affected heavily by elevated pressure and high temperatures. The autoignition phenomenon that take place in diesel engines must be encompassed by the mechanism. Crua et al. [21] have shown that ignition delay is affected by cylinder

pressure at the SOI. As cylinder pressure, at the SOI, increases along isotherms, ignition delay tends to decrease, reach a minimum, and then increase again. Penyazkov et el. [22] provided some data for kinetics modeling validation at very high pre-ignition temperatures.

Mechanism files consist of a series of chemical reactions together with the associated coefficients and exponents within the Arrhenius equation. The numerical techniques needed to find the input terms of the Arrhenius equation are extensive and computationally costly because a large system of differential equations must be solved using a number of complex algorithms. A separate thermodynamic database is utilized to generate the thermodynamic property list for each of the species. The production rate $w_i$ of a particular species is found by considering the rate variables for the species defined by each reaction equation in which it is involved. The production rate of a chemical species is defined as

$$w_i = \sum_{j=1}^{J} v_{i,j} q_j \tag{3}$$

The list of reactions in the mechanism is balanced and number of reacting moles ${v_{i,j}}'$ is subtracted from the number of produced moles ${v_{i,j}}''$ of the species to find the stoichiometric difference.

$$v_{i,j} = v''_{i,j} - v'_{i,j} \tag{4}$$

The species rate of progress is defined using the forward $k_{f,j}$ and reverse $k_{r,j}$ reaction rates for each term.

$$q_i = k_{f,j} \prod_{j=1}^{J} [X_j] v_{i,j}^{'} - k_{r,j} \prod_{j=1}^{J} [X_j] v_{i,j}^{''} \tag{5}$$

$$k_{f,j} = A_j T^{b_j} e^{\frac{-E_j}{R_c T}} \tag{6}$$

$$k_{r,j} = \frac{k_{f,j}}{K_{c,j}} \tag{7}$$

The forward rate is defined using the Arrhenius equation, which is derived from differential reaction rate laws, and its terms depend on the order of the particular reaction within the mechanism as some reactants may be used at higher rates than others. The reverse reaction rate is defined in terms of the concentration-based reaction constant $K_{c,j}$

$$K_{c,j} = K_{p,j} \left( \frac{P_{atm}}{R_c T} \right)^{\sum_{j=1}^{J} v_{i,j}} \tag{8}$$

The pressure-based reaction constant $K_{p,j}$, which is defined using the entropy, $\Delta S_j^{\circ}$ and enthalpy, $\Delta H_j^{\circ}$ changes during the reaction, is needed to calculate $K_{c,j}$.

$$K_{p,j} = e^{\left( \frac{\Delta S_j^{\circ}}{Rc} - \frac{\Delta H_j^{\circ}}{R_c T} \right)} \tag{9}$$

$$\frac{\Delta S_j^\circ}{R_c} = \sum_{j=1}^{J} \left( v_{i,j} \frac{S_i^\circ}{R_c} \right)$$

(10)

$$\frac{\Delta H_j^\circ}{R_c T} = \sum_{j=1}^{J} \left( v_{i,j} \frac{H_i^\circ}{R_c T} \right)$$

(11)

The thermodynamic file contains a list of the several chemical species of the mechanism and has the coefficients $a_{0,i}$, $a_{1,i}$, $a_{2,i}$, $a_{3,i}$, $a_{4,i}$, $a_{5,i}$, and $a_{6,i}$ necessary to estimate the isobaric specific heat, entropy, and enthalpy differentials of each species, for a given temperature, during the reaction.

$$\frac{C_{p,i}^\circ}{R_c} = a_{0,i} + a_{1,i} T + a_{2,i} T^2 + a_{3,i} T^3 + a_{4,i} T^4$$

(12)

$$\frac{S_i^\circ}{R_c} = a_{0,i} \ln(T) + a_{1,i} T + \frac{a_{2,i} T^2}{2} + \frac{a_{3,i} T^3}{3} + \frac{a_{4,i} T^4}{4} + a_{6,i}$$

(13)

$$\frac{H_i^\circ}{R_c T} = a_{0,i} + \frac{a_{1,i} T}{2} + \frac{a_{2,i} T^2}{3} + \frac{a_{3,i} T^3}{4} + \frac{a_{4,i} T^4}{5} + \frac{a_{5,i}}{T}$$

(14)

The initial general assumption for gas phase kinetics is that the sum of all mass in the reactor is constant and the reactants are well mixed so as to disregard turbulent diffusion within the Kolmogorov scales. None the less, individual species mass terms in the global sum are each changing with time until they reach equilibrium and the change

rate is defined as the product of production rate $w_i$, the reactor volume $V$, and the species molecular mass $M_i$.

$$\frac{\mathrm{dm}_i}{\mathrm{dt}} = V w_i M_i \tag{15}$$

The combustion of middle distillate fuels is complex and has to be simplified and approximated using surrogates. Farrell et al. [23] working at the National Institute of Standards and Technology (NIST) have made considerable effort to devise a surrogate database to ease the process of generating mechanism. Harper [24] introduced software using linked libraries to automatically generate mechanisms to user specifications. In experiments, the individual species concentrations must be measured accurately but, current technology uses limited spectroscopy techniques.
[25] Mechanisms used in simulations are thus practically relegated to using models of surrogates for the purposes of verification. [26] Generating mechanisms is typically done by analyzing the pressure, thermal conditions, and analyzing the subsequent pathways of sub mechanisms for H2, CO, methane, and more complex hydrocarbons. Reactions can be combined depending on the products of chain initiating reactions. Typically several unimolecular reactions with high rates are used to initiate the breaking of the large surrogates into smaller chains and radicals such as hydroxyl. [27] Pyrolysis is naturally included in unimolecular reactions and offers a way to model soot formation in concert with PAH formation in detail. Biodiesel consists of several long chain methyl esters. Researchers and scientists at the Lawrence Livermore National laboratory have produced several detailed mechanisms for soy methyl ester (SME) and rapeseed methyl ester (RME) biodiesel. There are five main methyl ester components in biodiesel

which are C17H34O2 (methyl palmitate) , C19H38O2 (methyl stearate), C19H36O2 (methyl oleate), C19H34O2 (methyl linoleate), and C18H32O2 (methyl linolenate). Figure 13 shows the five main methyl esters within plant-based biodiesel.

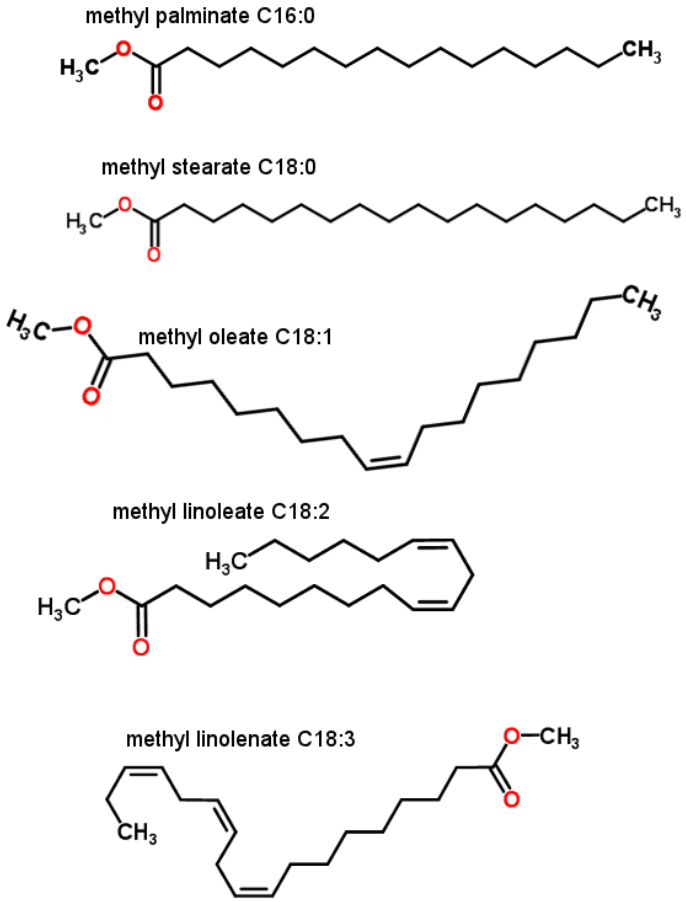


**Figure 13: Typical FAME molecules produced by transesterification**

The five methyl esters have been replaced with simpler surrogates called methal decanoate (MD) and methyl-9-decanoate (MD9D), in many complex mechanisms. At least two surrogates have to be used to reproduce the chemistry associated with saturated and unsaturated ester combustion. Skeletal mechanisms using MD and MD9D have been developed by Luo et al. [28] and many others. The differing volumetric ratio of the five main methyl esters in various biodiesel fuel types such as SME, RME, palm methyl ester (PME), or canola methyl ester (CME) is the main source

of their differing physical properties and combustion characteristics such as liquid spray penetration [29], cavitation, or ignition delay as shown by Dorri et al. [30]. The current version of the surrogate LLNL biodiesel mechanism proposed by Westbrook et al. [31] is comprised of 3299 species and 10806 reactions. It should be noted that detailed reaction models are typically too complex for addition into numerical fluid analyses running on workstations. The species count and number of equations in those mechanisms creates too many conservation equations and subsequent source terms in energy equations. Such stiff non-linear systems are too computationally intensive because of high sensitivity and require an investment in extensive computational resources which are impractical for most small development firms and researchers. That stiffness is compounded by the addition of turbulence modeling that is sometimes also necessary. The number of species must be reduced to a number less than 150 to allow a mechanism to be practical for CFD. The diesel cycle relies on turbulent diffusion to mix fuel sprays into the charge air. In reality, turbulence directly influences the combustion reaction pathways and the progress rates. Turbulence is thus affecting the types, amounts of product species, heat release, and the usable crankshaft torque. Engineers are typically only concerned with average solutions of the flow field. Ultimately, the results from several CFD case configurations will be used to predict mass or volumetric emission rates of a particular engine at discrete points within the FTP transient and European Union test cycles. Kokjohn and Reitz [32] have shown that the actual chemistry is more important that the subscale turbulence within the Kolmogorov microscales. Reduction of the mechanism is the way to allow the reaction to be modeled accurately yet, reduce the computational load which will be discussed in the next section.

### 2.1.2 Mechanism Reduction and Validation Techniques

The object of reduction is to identify and remove species and reactions that don't significantly affect the concentrations and flow solution. If discovery of the engine torque based on crankshaft angle and pressure is the goal, more species and reactions which only contribute to the accuracy of the emissions would be removed to streamline the computation. If prediction of the emission species and their quantities are to be investigated, less species are to be removed. Mechanism reduction can be carried out using three methods which are static, dynamic, and time scale separation. The actual process of reduction can be quite difficult by hand or inspection of the reaction paths, which is why several automated methods have been devised.

Reaction flow analysis (RFA) focuses on removing species with the least atomic transfer activity. There are several versions of RFA as it is the earliest form of mechanism analysis. Sensitivity analysis works by removing single species and noting the effects on the formation rates of other species in the mechanism using RFA techniques. If the absolute value of the change in the formation rates of certain species is too large, the affecting species is not removed. One early time-scale algorithm used for reduction is referred to, by Maas and Pope [33], as the intrinsic low dimensional manifold method (ILDM). The first problem, pertaining to the base mechanism, is identifying the chemical equilibrium state point's "distance" along a curve from the initial condition point along an isochore. The specific mole number of a series of radicals and products are tracked during a zero dimensional reaction solution for the main mechanism. The specific mole number of key species such as the fuel, radicals, and products are compared against a set of master curves produced from the original calculation. Species and reactions are removed, according to directives, and the

resulting system is solved and compared to the base mechanism. The solutions and comparisons are made until no more species and reactions can be removed without significantly deviating from the original solution. Several new automated methods of mechanism reduction have been devised such as the directed relation graph method (DRG). A DRG mechanism reduction scheme produces skeletal mechanisms by quantification of the importance of initial species to ones that occur later in the reaction. DRG methods are typically used as an intermediary process in automated reduction software. There have been several additions to the DRG method, such as directed relation graph with error propagation and sensitivity analysis (DRGEPSA), as described by Niemeyer et al. [34]. Nagy and Turanyi [35] have introduced a more task and use focused technique referred to as simulation error minimization (SEM). Some reduction methods may be better than others but, users are more concerned with tradeoffs between speed, accuracy, and efficiency. Mechanisms that are typically already reduced require combination of several methods as shown by Ng et al. [36].

Validation of base mechanisms is typically carried out in shock tube, plug flow, and jet-stirred reactors. The products flowing out of the reactor are analyzed extensively as the reactor operates at quasi-static conditions. The calculated species concentrations over time, ignition delay times, temperatures, and pressures resulting zero or two dimensional simulations are verified against analyzed data. In the case of Westbrook et al. [31], there is not a wide array of combustion data for biodiesel across various temperatures, pressures, and equivalence ratios. Predictions of combustion characteristics sometimes have to be used as a basis of validation until peers expand experimental research envelopes. Much of the experimentation that does exist is done with various other proposed methyl ester surrogates or mixtures of alkanes, with known

chemistry, and FAME such as Herbinet et al. [27]. Reduced mechanisms, for use within a certain range of conditions, are compared to the results of the base mechanism at the same conditions as was done by Brakora et al. [37]. Experiments done specifically on internal combustion engines or their systems don't typically focus on high order details of kinetics specifically because the mechanical idiosyncrasies and physical phenomenon of fuel atomization, happening in concert, make the overall subject far too complicated. Singh et al. [38] and Brakora [39] each focus directly on some aspect of modeling particular aspects of diesel engine operation with kinetics directly involved. Engines are directly tested so that all of the complexity of the chemistry can be bypassed and solutions to particular problems, such as high emissions, can be more directly solved. Spray parameters and piston geometry are the most practical areas to focus attention on.

## 2.2 Engine Focused Experiments

### 2.2.1 Injection Experiments

The process of injecting diesel, biodiesel, or a blend into the cylinder through orifices within the body of the injector leads to a naturally leads to a particular distribution of equivalence ratio. Diesel fuel being expelled from an injector is shown in figure 14. The type and quantity of harmful emissions thus depends on the cylinder conditions at the SOI, the physical properties of the fuel, the injector geometry, and the combustion chamber geometry. The injector, nozzle, and fuel properties directly affect the fuel droplet diameter distribution. Typically injection studies have been done at atmospheric pressure so that surface wave phenomenon, caused by drag, can be observed occurring on droplets as they travel away from the fuel nozzle. The effect of injection pressure on velocity and its subsequent affect on droplet size was studied extensively by Koo and Martin [40].

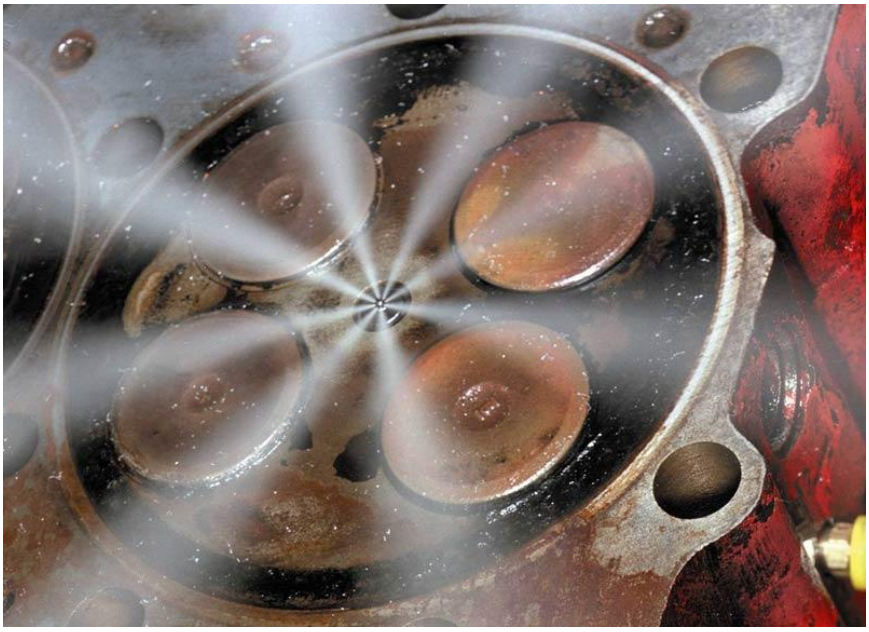

**Figure 14: Spray emitted from a high-pressure N14 diesel fuel injector.**

Injection studies tend to be done in high pressure spray boxes or in CFD. With advents in high-speed signal processing equipment, researchers are now able to study combusting dynamic sprays in high pressure environments. Kennaird et al. [41] used a combination of high speed and Schlieren cinematography to study combusting sprays. Injectors with various geometries and orifice diameters were tested to observe the effect on spray penetration lengths. Payri et al. [42] conducted an extensive study effects orifice diameter and injection pressure on CH after mixture and OH formation after ignition around the jet. A spray penetration model was introduced by Abani and Reitz [43] using jet theory for the incorporation of time varying injection into CFD models.

### 2.2.2 Engine Experiments

Engine experiments mostly test injection strategies on engines of particular displacements or piston geometries. Li et al. [44] investigated how the depth of omega piston geometry affects emissions and efficiency of diesel engines. Much like the injection experiments, either physical experimentation or numerical investigations are conducted. There have been quite a number of studies where researchers have measured the emissions of biodiesel combustion at various operating conditions and loads. Schumacher et al. [45] and the USEPA [46] demonstrate percentage decreases in oxides of carbon and nitrogen ($NO_X$) as well as particulate matter and unburned hydrocarbons using soybean B20 fuel. Cheng et al. [47] and Muller et al. [48] both used a Caterpillar SCORE similar to the one used by Brakora [39] to investigate the increase in oxides of nitrogen using SME fuel and attributed its cause to factors other than the start of combustion crank angle window. Increased NOx emissions can be attributed to a difference in flame lift-off length (LOL) and the higher elapsed time of combustion due

to increased viscosity between biodiesel and diesel according to Yuan and Hansen [49]. The engine and operating conditions used in this thesis were extracted from Singh [11] where several CFD combustion models were adjusted and tested fit experimental data retrieved from the Sandia/Cummins N14.

Experiments have been conducted using methyl esters made from several oils. Nabi et al. [50] produced several batches of cotton seed oil methyl ester (CSOME) and the trend of reduced emissions and increased NOx. Barabas et al. [51] used blends of diesel, biodiesel, and bio-ethanol and identified a decrease in engine thermal efficiency.

## 2.3 Properties of Biodiesel

### 2.3.1 Liquid Properties and Sprays

The liquid properties of biodiesel can negatively influence the quality of its movement throughout the fuel system of the engine as shown by Tefsa et al. [52]. Biodiesel of various types is known to dissolve fuel lines and clog filtration devices due to its chemical composition and other physical differences. Haseeb et al. [53] immersed several types of elastomers into palm methyl ester (PME) and recorded reduction in material strength. Electrochemical reactivity is not a typical focus of numerical flow studies however, some material properties are measured which are of concern. The fluid properties are needed in CFD studies to adjust the spray and breakup models. Pastor et al. [54] studied the effect of liquid fuel properties of five fuels on liquid penetration distance length in diesel engines and found that it is proportional to viscosity. Most literature, involving biodiesel, cites common proprieties at room temperature. For the best precision, it is necessary to have property curves as functions of temperature. Tate et al. [55] utilized a capacitance densitometer to measure the density of soy, canola, and fish oil methyl ester up to 573K. Silva et al. [56] measured and curve fit the specific heat and enthalpy of SME and several other biofuels. Distillation curves, density, and viscosity were generated from data gathered by Alptekin and Canakci [57], Ramírez-Verduzco et al. [58], Tate et al. [59] and Su [60]. Droplet surface tension was estimated by several researchers and most of the work was overviewed by (Doll et al. [60].

### 2.3.2 Vapor Properties and Combustion

The characteristics of biodiesel fuels must be known at temperatures in the vapor phase in order to model droplet atomization, evaporation, and combustion within the cylinder. There is not a sizable volume of literature with the vapor properties of plant oils or methyl esters verified using specialized experiments. There are experiments documented in literature where heat of combustion and boiling points are determined such as Ackers et al. [61] and Goodrum [62]. Biodiesel, as discussed in chapter 2.2.1, is typically composed mostly of no more than combustible 6 methyl esters. An assumption of high fuel purity is necessary to use the type of estimation methods in Reid et al. [63] and Poling et al. [64]. Several estimations using chemical group contribution methods were used to calculate critical parameters and properties for use in the spray modeling throughout this thesis work. Critical pressure and temperature of each pure methyl ester can be estimated using Ambrose's method as explained in chapter two of Reid et al.

$$T_c = T_b[1 + (1.242 + \sum \Delta_T)^{-1}] \tag{16}$$

$$P_c = M(0.339 + \sum \Delta_P)^{-2} \tag{17}$$

Critical specific volume of each methyl ester, $V_c$, can be estimated using the Lydersen-Joback method.

$$V_c = 17.5 + \Sigma \Delta_V \tag{18}$$

The terms $\Sigma\Delta_V$, $\sum\Delta_T$ and $\sum\Delta_P$ are the sums of bond contributions in each molecule which can be found in tables 2-1, and 2-2 in Reid et al.

The Lee-Kesler mixture property equations are used to calculate the critical temperature, $T_{\mathrm{cm}}$, pressure, $P_{\mathrm{cm}}$, and volume, $V_{\mathrm{cm}}$, of the methyl ester mixtures. The thermophysical properties of biodiesel, beside pour point, viscosity, cetane number, and liquid density, tend to not vary with the differing ratios of methyl oleate and methyl linoleate.

$$T_{\mathrm{cm}} = \frac{1}{V_{\mathrm{cm}}^{1/4}} \Sigma_i \Sigma_j y_i y_j V_{cij}^{1/4} T_{cij} \tag{19}$$

$$V_{\mathrm{cm}} = \Sigma_i \Sigma_j y_i y_j V_{cij} \tag{20}$$

$$T_{cij} = \left(T_{ci} T_{cj}\right)^{1/2} k_{ij}^{'} \tag{21}$$

$$V_{cij} = \frac{1}{8}\left(V_{ci}^{1/3} + V_{cj}^{1/3}\right)^3 \tag{22}$$

In equations 19, 20, manipulations of mole fraction, and binary mixture critical property matrices define the ultimate properties of the overall mixture. Binary critical temperature parameters, $k_{ij}^{'}$, are not currently published for individual constituent methyl esters and is estimated to be greater than 0.98 and less than 1.02, for all cases.

The index variables $i$ and $j$ indicate row and column positions in variable matrices of equations 19, 20, 21, and 22. The Pitzer acentric factor, $\omega_i$, of each constituent methyl ester is used to define the acentric factor of the biodiesel fuel mixture $\omega_m$.

$$\omega_m = \sum_i y_i \omega_i \tag{23}$$

$$\omega_i = \frac{\alpha}{\beta} \tag{24}$$

$$\alpha = -\ln P_{ci} - 5.97214 + 6.09648\theta^{-1} + 128862\ln\theta - 0.169347\theta^6 \tag{25}$$

$$\beta = 15.2518 - 15.6875\theta^{-1} - 13.4721\ln\theta + 0.43577\theta^6 \tag{26}$$

$$\theta = \frac{T_{bi}}{T_{ci}} \tag{27}$$

$P_{ci}$, $T_{bi}$, and $T_{ci}$ are the critical pressure, normal boiling point, and critical temperature of each pure methyl ester constituent.

$$P_{\mathrm{cm}} = \frac{(0.2905 - 0.085\omega_m)RT_{\mathrm{cm}}}{V_{\mathrm{cm}}} \tag{28}$$

The vapor pressure, $P_{vPr}$, was estimated using the Pitzer acentricity factor relation.

$$T_r = \frac{T}{T_{\mathrm{cm}}} \tag{29}$$

$$\ln P_{vPr} = f^{(0)}(T_r) + \omega_m f^{(1)}(T_r) \tag{30}$$

$$f^{(0)} = 5.92714 - \frac{6.09648}{T_r} - 1.28862 \ln T_r + 0.169347 T_r^6 \tag{31}$$

$$f^{(1)} = 15.2518 - \frac{15.6875}{T_r} - 13.4721 \ln T_r + 0.43577 T_r^6 \tag{32}$$

Latent heat of vaporization, $\Delta H_v$, curves were estimated using the Pitzer acentricity factor relation at high temperatures and the Fish-Lielmezs methods at low temperatures. All specific material property tables are listed in appendix A.

$$\Delta H_{v-low} = \Delta H_{vb} \frac{T_r}{T_{br}} \frac{\chi + \chi^{0.35298}}{1 + \chi^{0.13856}} \tag{33}$$

$$\chi = \frac{T_b}{T_r} \frac{1 - T_r}{1 - T_{br}} \tag{34}$$

$$\Delta H_{v-high} = R T_{\mathrm{cm}} [7.08(1 - T_r)^{0.354} + 10.95 \omega_m (1 - T_r)^{0.456}], \qquad 0.6 < T_r \leq 1.0 \tag{35}$$

# CHAPTER 3

# METHODOLOGY

## 3.1 Flow Modeling

The governing equations of the flow within the domain are the continuity, Navier-Stokes momentum, and the energy conservation equation. The equations are commonly expressed in the form of partial differential equations applied on stationary and infinitesimal fluid elements. The density, $\rho$, velocity, $\vec{v}$, pressure, $p$, temperature, $T$, and thermal energy, $E$, are the major variables to be solved given a typical compressible flow.

$$\frac{\partial \rho}{\partial t} + \nabla \cdot \rho\vec{v} = m_s \tag{36}$$

$$\frac{\partial \rho\vec{v}}{\partial t} + \rho\vec{v} \cdot \nabla\vec{v} = -\nabla p + \frac{\nabla \cdot \mathbf{T}}{R_e} \tag{37}$$

$$\frac{\partial \rho E}{\partial t} + E\nabla \cdot \vec{v} = -p\nabla \cdot \vec{v} + \nabla \cdot k_{eff}\nabla T_k + E_s \tag{38}$$

The Reynolds-Averaged Navier-Stokes (RANS) equations are a way to express the field variable fluctuations due to turbulence within the flow using time-averaging of all variables. Because of the addition of Reynolds stress terms, of the form, $\overline{\overline{\rho}u'v'}$, which are functions of several fluctuating variables, an extra method is needed to close the turbulence problem. The first method of modeling the Reynolds stress was proposed by Joseph Boussinesq by introducing the eddy viscosity theory. The transformation and

substitutions for the unknown turbulent Reynolds stress terms encompasses the area of turbulence modeling.

$$\frac{\partial \overline{\rho}}{\partial t} + \nabla \cdot \overline{\rho}\widetilde{\mathbf{U}} = 0 \tag{39}$$

$$\frac{\partial \overline{\rho}\widetilde{U}}{\partial t} + \nabla \cdot \overline{\rho}\widetilde{U}\widetilde{\boldsymbol{U}} = -\frac{\partial \overline{P}}{\partial x} + \nabla \cdot \mu \nabla \widetilde{U} - \frac{\partial \overline{\overline{\rho} u''^2}}{\partial x} - \frac{\partial \overline{\overline{\rho} u'' v''}}{\partial y} - \frac{\partial \overline{\overline{\rho} u'' w''}}{\partial z} + S_{Mx} \tag{40}$$

$$\frac{\partial \overline{\rho}\widetilde{V}}{\partial t} + \nabla \cdot \overline{\rho}\widetilde{V}\widetilde{\boldsymbol{U}} = -\frac{\partial \overline{P}}{\partial y} + \nabla \cdot \mu \nabla \widetilde{V} - \frac{\partial \overline{\overline{\rho} u'' v''}}{\partial x} - \frac{\partial \overline{\overline{\rho} v''^2}}{\partial y} - \frac{\partial \overline{\overline{\rho} v'' w''}}{\partial z} + S_{My} \tag{41}$$

$$\frac{\partial \overline{\rho}\widetilde{W}}{\partial t} + \nabla \cdot \overline{\rho}\widetilde{W}\widetilde{\boldsymbol{U}} = -\frac{\partial \overline{P}}{\partial z} + \nabla \cdot \mu \nabla \widetilde{W} - \frac{\partial \overline{\overline{\rho} u'' w''}}{\partial x} - \frac{\partial \overline{\overline{\rho} v'' w''}}{\partial y} - \frac{\partial \overline{\overline{\rho} w''^2}}{\partial z} + S_{Mz} \tag{42}$$

$$\frac{\partial \overline{\rho}\widetilde{\Phi}}{\partial t} + \nabla \cdot \overline{\rho}\widetilde{\Phi}\widetilde{\boldsymbol{U}} = \nabla \cdot \mu \Gamma_{\Phi} \nabla \widetilde{\Phi} - \frac{\partial \overline{\overline{\rho} u'' \Phi''}}{\partial x} - \frac{\partial \overline{\overline{\rho} v'' \Phi''}}{\partial y} - \frac{\partial \overline{\overline{\rho} w'' \Phi''}}{\partial z} + S_{\Phi} \tag{43}$$

The Laudner-Sharma k-epsilon turbulence model is used to represent the Boussinesq turbulent viscosity factor as a balance of conserved energy and it's dissipation in to small eddies. The small length and timescales of those eddies does not have to be considered directly, only the kinetic energy transferred and dissipated through friction resulting from eddy viscosity within the domain fluid.

$$\boldsymbol{T} = -\rho\overline{u_i{}'u_j{}'} = \mu_t\left(\frac{\partial \boldsymbol{U}_i}{\partial x_j} + \frac{\partial \boldsymbol{U}_j}{\partial x_i}\right) - \frac{2}{3}\rho k\boldsymbol{\delta}_{ij}$$

(44)

$$k = \frac{1}{2}\left(\overline{u'^2} + \overline{v'^2} + \overline{w'^2}\right)$$

(45)

$$\frac{\partial pk}{\partial t} + \nabla \cdot \rho k\boldsymbol{U} = \nabla \cdot \left(\frac{u_t}{\sigma_k}\nabla k\right) + 2\mu_t \boldsymbol{S}\cdot\boldsymbol{S} - \rho\varepsilon$$

(46)

$$\boldsymbol{\frac{\partial p\varepsilon}{\partial t} + \nabla \cdot \rho\varepsilon U = \nabla \cdot \left(\frac{u_t}{\sigma_\varepsilon}\nabla\varepsilon\right) + C_{1\varepsilon}\frac{\varepsilon}{k}2\mu_t S\cdot S - C_{2\varepsilon}\rho\frac{\varepsilon^2}{k}}$$

(47)

$$\mu_t = \rho C_\mu \frac{k^2}{\varepsilon}$$

(48)

The turbulent kinetic energy, $k$, and it dissipation rate, $\varepsilon$, are subject to convection and diffusion, as scalars, and their overall rates of change are augmented using several constants. The constants various are $C_\mu = 0.09,\ \sigma_k = 1.00,\ \sigma_\varepsilon = 1.30,\ C_{1\varepsilon} = 1.44$, and $C_{2\varepsilon} = 1.92$.

### 3.2 Spray Modeling

Sprays are some of the most complex phenomenon known and occupy a vast research field of their own. Sprays emitted from diesel injectors can be broken up into fuel material atomization, initial breakup, collision, secondary breakup, and vaporization. It is the spacial distribution of vaporization within the cylinder which primarily affects

combustion. By dividing sprays into separate areas, separate discrete and empirical models can then be interjected to simplify complex aspect of sprays. A quiescent chamber CFD model was used to calibrate the overall injection and breakup models against the liquid and vapor penetration distances provided in the experimental data of Singh [11]. The stand-alone high pressure chamber allowed the parameters of the spray model to be studied and augmented independently of the overall engine model. Figure 15 is a labeled depiction of a mini-sac injector.

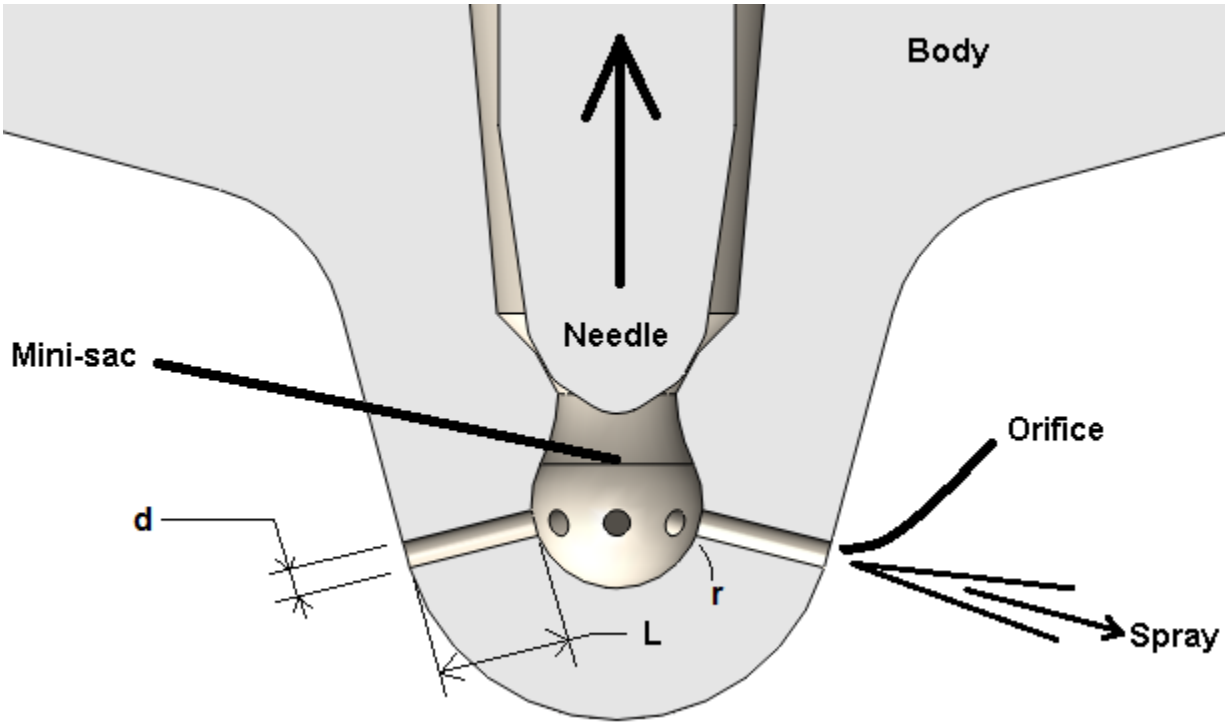


**Figure 15: Mini-sac diesel injector tip**

A phenomenological plain orifice atomization model was utilized to empirically incorporate internal nozzle conditions and their physical effects on the spray angle, droplet geometry, and droplet velocity. High pressure flows through cylindrical nozzles is very complex. In the plain orifice model, the nozzle flow velocity, $u$, coefficient of

discharge, $C_d$, the spray angle, $\theta$, and the cavitation number, $K$, for separate nozzle operation regimes, are calculated using the injection pressure, $P_i$, cylinder pressure near the nozzle orifice, $P_{cyl}$, Reynolds number, $Re_h$, nozzle geometry, area coefficient, $C_a$, and the fuel properties such as liquid density, $\rho_L$, and vapor pressure, $P_v$. Fuel kinematic viscosity, $\mu_L$, mass flow rate, $\dot{m}$, and a proportionality constant, $A$, are also used to calculate injection parameters.

$$K = \frac{P_i - P_v}{P_i - P_{cyl}} \tag{49}$$

$$Re_h = \frac{d\rho_L}{\mu_L}\sqrt{\frac{2\left(P_i - P_{cyl}\right)}{\rho_L}} \tag{50}$$

$$C_a = \frac{1}{\sqrt{\frac{1}{C_t^2} - \frac{11.4r}{d}}} \tag{51}$$

$$C_d = \frac{\dot{m_{eff}}}{A\sqrt{2\rho_L\left(P_i - P_{cyl}\right)}} \tag{52}$$

Nozzle conditions change abruptly during the operation of the injector. Typically as the needle is lifting, the flow is a single liquid phase.

$$C_{d_{lq}} = \frac{1}{\frac{1}{0.827 - 0.0085L/d} + \frac{20(1 + 2.25L/d)}{Re_h}}, K > K_s or K \geq K_{critical}$$

(53)

$$u_{lq} = \frac{\dot{m}_{eff}}{\rho_L A}$$

(54)

{Single Phase Equations}

As the needle continues to lift, the flow transitions to a flipped type of flow and the definition of.

$$C_{d_{flip}} = C_t = 0.611, K < K_{crit}$$

(55)

$$u_{flip} = \frac{\dot{m}_{\text{eff}}}{c_{d_{flip}} \rho_L A}$$

(56)

$$\theta_{flip} \approx 0.02 rad$$

(57)

Because of fuel properties and deviations in injector geometry having an effect on the inception of cavitation, an empirical method is used to test the cavitation number with respect to nozzle inlet rounding. If the critical cavitation number, $K_{crit}$, is reached, and conditions are right, the nozzle spray will result in cavitation.

$$K_s = 1.9\left(1 - \frac{r}{d}\right)^2 - \frac{1000}{Re_h}$$

(58)

$$K_{crit} = 1 + \frac{1}{\left(1 + \frac{L}{4d}\right)\left(1 + \frac{2000}{Re_h}\right)\mathrm{e}^{70r/d}}$$

(59)

$$C_{d_{cav}} = C_a\sqrt{K}, K_{ritc} \leq K \leq K_s$$

(60)

$$u_{cav} = \frac{2C_a\rho_i - \rho_{cyl} + (1 - 2C_a)P_v}{C_a\sqrt{2\rho_L(P_i - P_v)}}$$

(61)

$$\theta_{liquid,cav} = 2\tan^{-1}\left[\frac{2\sqrt{3}\pi}{6 + \frac{1.667L}{d}}\sqrt{\frac{\rho_g}{\rho_L}}\right]$$

(62)

As the needle closes the fuel supply to the mini-sac, the flow transitions back through the modes of flow in reverse. It is the transitional flow phenomenon in concert with fluid properties which leads to the complexity of high pressure orifice sprays. There is a lot of interplay between the cylinder pressure and the spray velocity implied by Bernoulli's equation. It is the increase in cylinder pressure that overcomes liquid fuel viscosity and leads to cavitation and atomization. Droplet breakup, collision, and secondary breakup are simulated using the Kelvin-Helmholtz (KH) aerodynamic drag model, O'Rourke's collision probability algorithm, and the Raleigh-Taylor (RT) instability breakup model. A Lagrangian discrete phase model (DPM) is used to simulate turbulent droplet dispersion. The KH-RT model assumes that fuel droplets are emitted from a column of liquid blobs because of shear forces imparted by the continuous phase.

Those droplets may collide and form larger droplets or travel on being guided by the continuous phase. The smallest discrete droplets, which will no longer collide or breakup, are in the domain after the secondary breakup process, the continuous gas phase interacts with them. The mass and velocity of the droplets is reduced via thermal and momentum energy transfer. The droplets vaporize and deposit their fuel mass into the cells along their path of travel through the combustion chamber and become part of the continuous gas phase. The aggregate continuous gas phase properties go into the finite-rate or eddy dissipation chemistry model and energy equation calculations.

The quiescent spray chamber model consists of one nozzle centered at the top with its spray axis in the downward vertical direction. The initial pressure within the chamber is held at the motored TDC pressure. The entire spray formation is simulated across all degrees of crankshaft angle movement for the DOI at 1200 revolutions per minute. The elapsed time of the spray is approximately 1389 microseconds, at high temperature engine operating conditions, with a 691 microsecond short ignition delay. The shape of the equivalence ratio field, liquid penetration length, and vapor penetration field with petroleum diesel were compared to the experimental data from Singh [11]. The use of a phenomenological spray model, that predicts initial spray distribution based on the injector specifications and fuel fluid properties, allows direct substitution of liquid fuels with slightly different physical properties with adjustments to the breakup model. The breakup model coefficient adjustments were arrived at using trial and error. The mesh used for the quiescent spray chamber is depicted in figure 16.

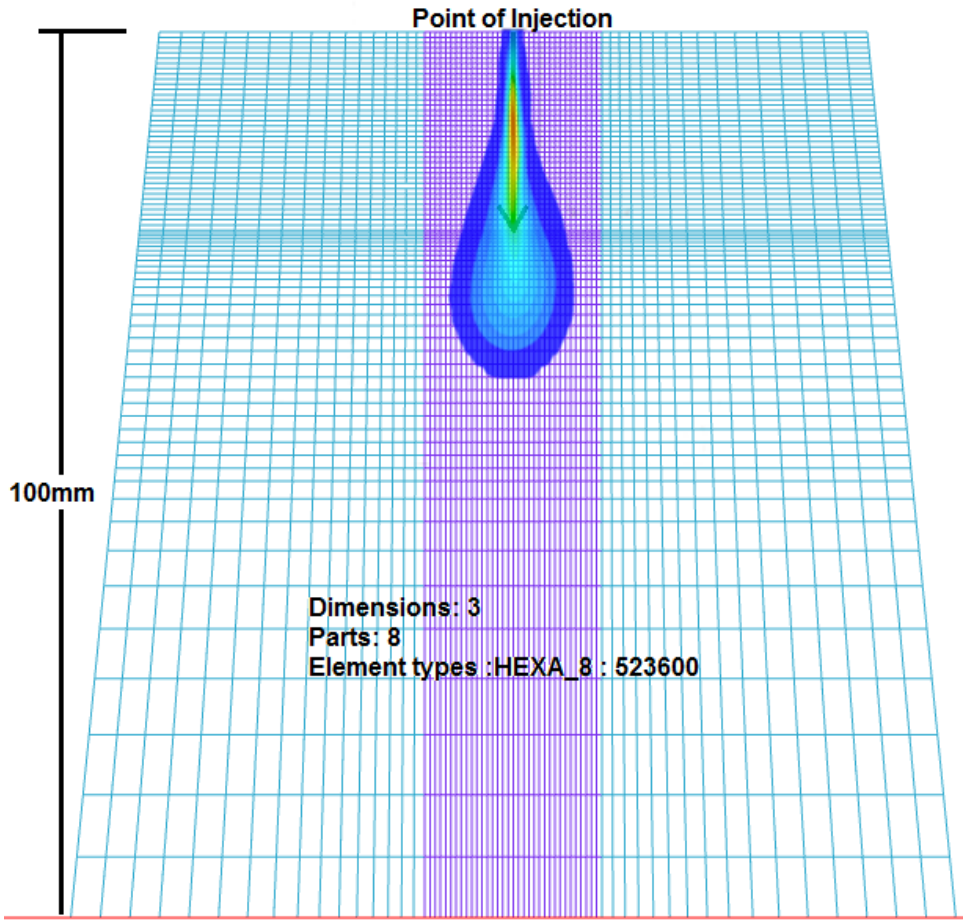


**Figure 16: Quiescent spray chamber mesh**

The specifications of the injector are listed in table 4

**Table 4: Sandia/Cummins N14 Injector Specification**

| Sandia/Cummins N14 Injector Specifications | |
|---|---|
| Type | Common Rail, pilot valve |
| Rail pressure | 120MPa or 160MPa |
| Cup type | Mini sac |
| Number of orifices | 8 - 1/45° |
| Orifice diameter (mm) | 0.196 |
| Orifice Length/Diameter | 5 |
| Included spray angle | 152° |
| Discharge coefficient | 0.67 |
| Area coefficient | 0.93 |
| Velocity coefficient | 0.72 |

### 3.3 Combustion Chamber Mesh Grid

The key geometry that must be reproduced is the piston and the proximity of its crown geometry to the head surface, within the combustion chamber during crankshaft angle change. The overall number of computations is directly related to mesh density, the number of steps during compression, the number of steps during combustion, and the complexity of the solver configuration. The mesh grid geometry of the combustion chamber volume, are pre-generated outside of ANSYS Fluent™ with ANSYS ICEM©. The mesh grids used for this thesis work are shown in Figure 17. The mesh grids are sector meshes that represent one eighth of the cylinder. Only one injection orifice is considered. The crevice measured from the top most surface of the piston down to the first ring was omitted.

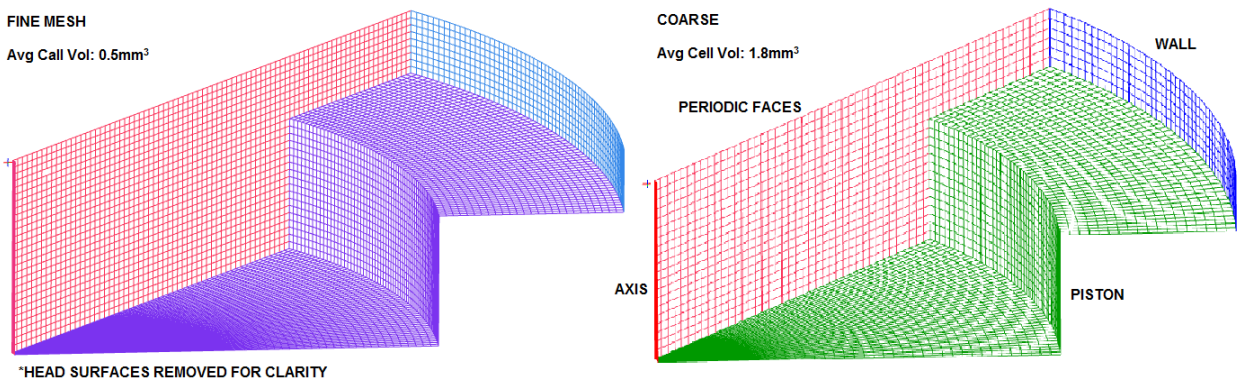


**Figure 17:Cylinder combustion mesh grids**

#### 3.3.1 Dynamic Meshing

The volume and shape of the combustion chamber are augmented along the cylinder axis. It is assumed that the crankshaft's angular velocity is constant which allows the time step size to be constant during the various phases of combustion. The Fluent solver requires that the user provides the number of desired steps. All of the

engine sector mesh grids, used in this thesis, that are read into Fluent, start at TDC and must be manipulated to expand them to the appropriate volume associated with the IVC crankshaft angular position. From that time point forward, the number of time steps required to reach the period just before the exhaust valve opens is defined by the following equation:

$$N_{steps} = \frac{\theta_{inj} - \theta_{IVC}}{\Delta\theta_{comp}} + \frac{\theta_{sc} - \theta_{inj}}{\Delta\theta_{comb}} + \frac{\theta_{EVO} - \theta_{sc}}{\Delta\theta_{ex}} \tag{63}$$

The crank angle step sizes for the compression, $\Delta\theta_{comp}$, combustion, $\Delta\theta_{comb}$,and exhaust, $\Delta\theta_{ex}$, cycles are typically 0.5, 0.1 ,0.2 degrees respectively. The actual value of the timestep, $\Delta t_{step}$, and the magnitude of the cell size can be used to determine the Courant number, $C_{courant}$.

$$\Delta t_{step} = \frac{\Delta\theta_i}{6\dot{\theta}_{cs}} \tag{64}$$

$$C_{courant} = \Delta t_{step} \sum_{i=1}^{3} \frac{u_i}{\Delta x_i} \leq 1 \tag{65}$$

A layering method is applied to collapse volume cells at the head surface as the combustion chamber volume decreases up to TDC. During expansion, volume cells are grown from the head surface. With the head surface fixed in space, the vertical position of the piston boundary surface, $h_p$, is calculated in terms of the crank angle, $\theta_{cs}$, and engine component geometry. The connecting rod length, $L_{con}$, and stroke length, $L_s$, the

crankshaft angular velocity, $\dot{\theta}_{cs}$, and the solution elapsed time, $t$, are needed to calculate $h_p$.

$$h_p = L_{con} + \frac{L_s}{2}\left(1 - \cos(\theta_{cs})\right) - \sqrt{L_{con}^2 - \frac{L_s^2}{4}\sin^2(\theta_{cs})} \tag{66}$$

$$\theta_{cs} = \theta_{IVC} + 6t\dot{\theta}_{cs} \tag{67}$$

Figure 18 is a diagram of equation 66.

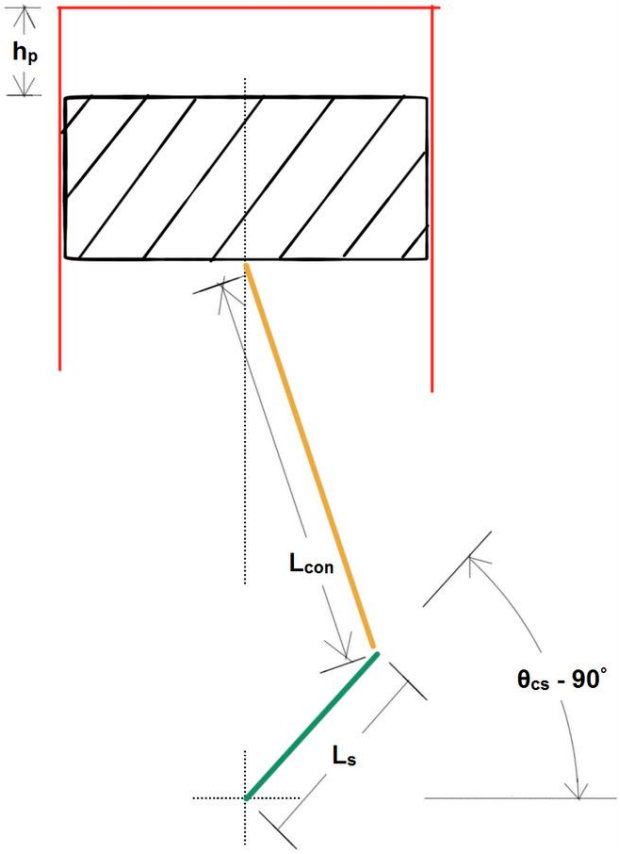


**Figure 18: Diagram depicting all terms in piston position calculation**

The cells are grown from and collapsed into the head boundary during the solution. The result is a separate mesh for each individual timestep. Figure 19 is a depiction of the mesh growth.

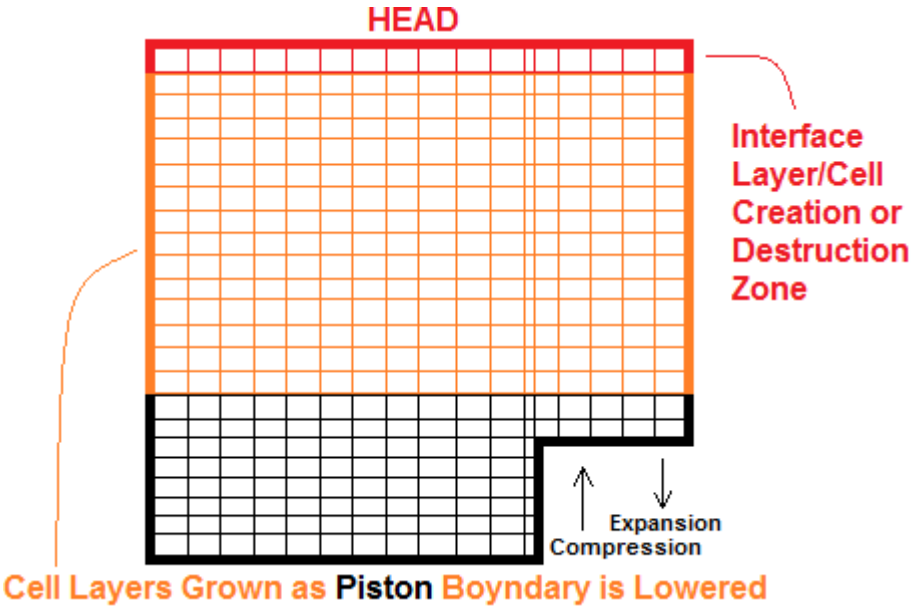


**Figure 19: Mesh grid cell augmentation during the solution process**

## 3.4 CFD Solver Configuration

### 3.4.1 Initial and Boundary Conditions

The typical steps for IC simulation, when the intake, valve, manifold port geometry, and velocity profiles are known, is to setup and solve a cold flow case with no combustion. In a cold flow case, the introduction of charge air through the intake port and valve is considered. The cold flow solution can be applied as the initial conditions of the compression and combustion simulation so that the initial field values at IVC can be made as realistic as possible. If the head port and valve geometry are not known, the initial conditions of swirl and tumble after IVC can be approximated. Because the

detailed cylinder head geometry of the N14 engine is unknown, at this time, all of the simulation in this work omits valve motion by simulating the time period from IVC to EVO. Also, cylinder air swirl and tumble are assumed to occur about cylinder axis. A user defined function, written in C, was used to define the initial velocity field at IVC. Trial and error methods were used to set the swirl ratio number at IVC such that the TDC swirl ratio was about 0.52 as stated by Singh [11]. Figure 20 is a depiction of the swirl phenomenon.

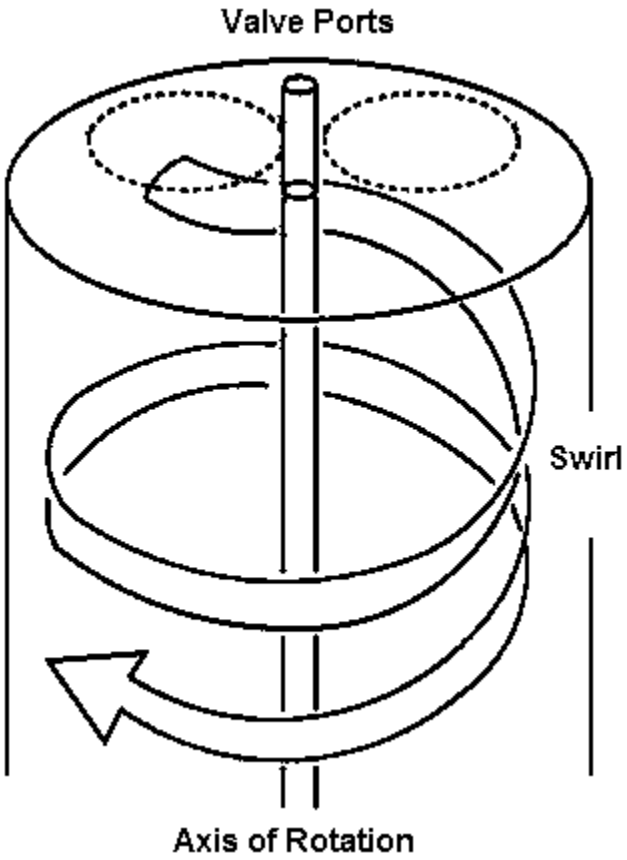


**Figure 20: Intake swirl flow diagram**

The initial air component mass fractions, gauge pressure, and temperature were set according to the specifications given in table 2 within section 1.3. The injection

settings were configured for each case by calculating the effective mass flow rate for one nozzle.

### 3.4.2 Pollutant Formation Modeling

Two pollutants of main concern are $NO_x$ and soot. They are both formed at opposite ends of the combustion operating range. $NO_x$ is typically formed when the combustion equivalence ratio is less than unity and flame temperatures are high. Soot is formed mostly as the result of pyrolysis within fuel rich regions at medium and lower temperatures. Because diesel engines operate at maximum volumetric frequency and rely on turbulent diffusion for reactant mixing, these two major pollutants are formed simultaneously. Figure 21 is a depiction of the soot and $NO_x$ formation zones as functions of equivalence ratio, combustion temperature, and air oxygen volume percentage.

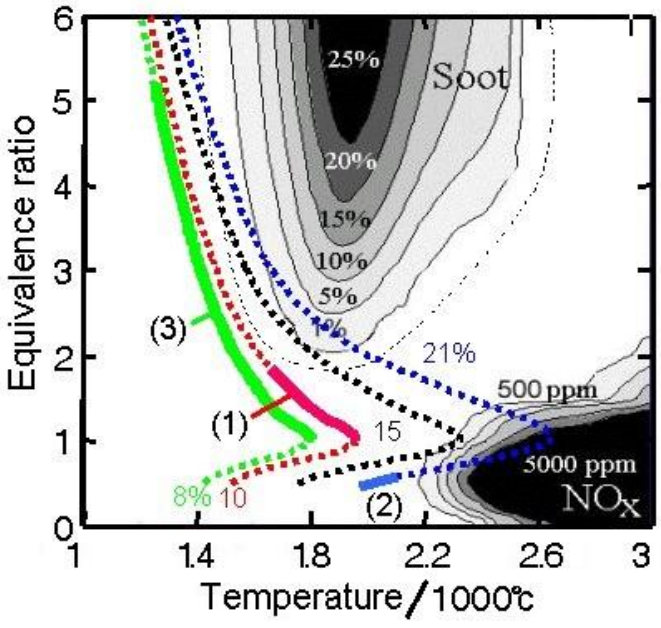


**Figure 21:Soot and NOx production zones typical of diesel engines (Sandia 1993)**

It was assumed that the major component of $NO_x$ emissions was nitric oxide (NO). Several models are used to predict NO formation. NO that is promptly formed in the regions of high equivalence ratio and low temperature can predicted using the Fenimore model. The Fenimore model was not used because the residence time of all species is 0.020seconds, which is particularly long. Without activating a return model, overproduction of NO would be a trend. Thermal NO is modeled using the Zeldovich mechanism correlations for the oxidation of nitrogen within the intake air.

The Tenser model was utilized for soot emission prediction which involves carbon forming on nucleating particles. Soot formation properties were set according to default values The stoichiometric of soot and fuel combustion were set respectively for each fuel based on carbon number.

Several Fluent custom field functions are used to calculate ending pollutant quantities at EVO and other points in the cylinder and are shown as a contiguous file in appendix A.

### 3.4.3 Solution Process

Along with the momentum equations, the pressure based Fluent solver is configured to solve the energy, viscous model, species transport, and reaction equations. Pressure and velocity is coupled using the pressure implicit with splitting of

operators (PISO) scheme. The overall solution process that results from the configuration of ANSYS Fluent™ is depicted in figure 22.

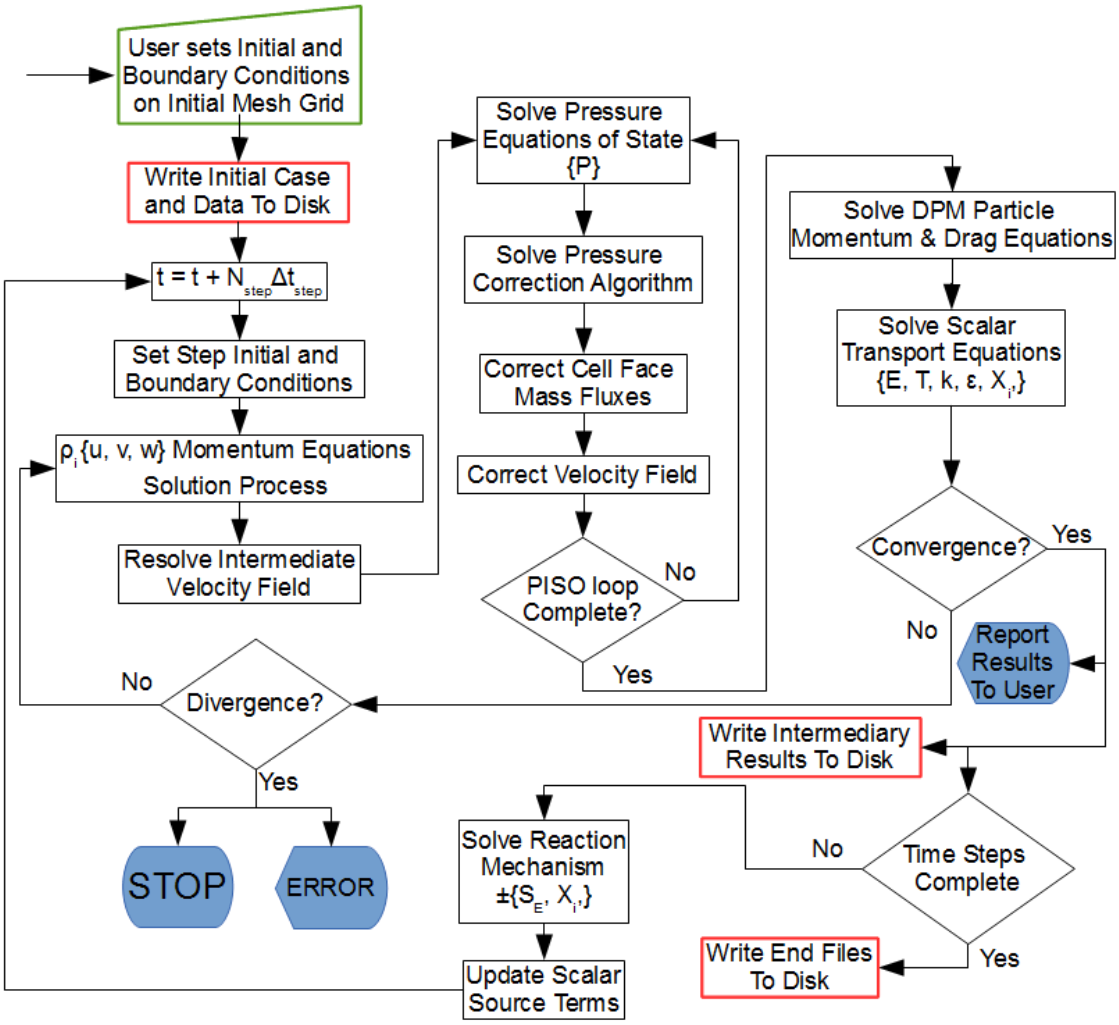


**Figure 22: ANSYS Fluent™ transient solution process after configuration**

### 3.5 Post-processing and Analysis

The was solver configured to output several parameters which allow generation of heat release curves. The apparent heat release rate (AHRR), $\frac{dQ}{d\theta}$, was numerically estimated using the calculated average cylinder pressure as a function of crank angle. The heat release equation in (Heywood 1988) was numerically represented as is the

typical practice to produce an AHRR curve from an experimental pressure trace. The Eichelberg empirical relation for convective heat transfer, out of the continuous phase, into the cylinder wall, was added.

$$\frac{dQ}{d\theta} = \frac{V\frac{dP}{d\theta} + \gamma P\frac{dV}{d\theta}}{\gamma - 1} - \frac{dQ_w}{d\theta} \tag{68}$$

$$\frac{dQ_w}{d\theta} = \frac{h_{conv}A_{wall}\left(T_w - T_j\right)}{24\dot{\theta}_{cs}} \tag{69}$$

$$h_{conv} = 7.67 \times 10^{-3}\sqrt[3]{\frac{L_s\dot{\theta}_{cs}}{30}}\sqrt{\left(P_i T_j\right)} \tag{70}$$

$$\frac{dP}{d\theta} = \frac{\Delta P}{\Delta\theta} = \frac{P_{j-1} - P_j}{\theta_{j-1} - \theta_j} \tag{71}$$

$$\Delta V_i = V_i - V_{i-1} \tag{72}$$

The average cylinder wall temperature, $T_w$, the bulk continuous phase temperature, $T_j$, the cylinder wall area, $A_{wall}$, and the combustion chamber volume, $V$, are obtained at the end of each converged time step. The values of pollutant quantities are only considered at EVO as it is assumed that combustion has concluded prior to that event.

# CHAPTER 4

# RESULTS AND DISCUSSION

## 4.1 Flow Variables

Simulations of diesel combustion were carried out for all five combustion regimes with the calibrated spray model for validation purposes. All pertinent results are compared to the results from Sandia N14 experiment data published by Singh. Ultimately the standard $k-\varepsilon$ turbulence and eddy dissipation species transport models were used for all simulations. The use of the Re-Normalization Group (RNG) $k-\varepsilon$ model was not continued due to negligible effect on the thermodynamics and species transport solution results with an average 30% increase in computation time. The mean cylinder pressure, and temperature near injector across TDC are in the form of curves versus crank angle where 720 crank angle degrees is TDC at the compression cycle. The combustion progress is expressed using grouped contour plots of fuel and $CO_2$ mass fraction at various crank angles during combustion. All contour plots expressing combustion progress are in appendix B.

### 4.1.1 Cylinder Pressure

The mean cylinder pressure is a measure of volume averaged cylinder pressure from IVC to EVO during the simulation. For case one, three diesel and one biodiesel simulations were conducted. The ignition delay is over predicted for case one. The RNG k-e turbulence model was utilized for the first diesel case in conjunction with a laminar finite-rate combustion model and had the longest ignition delay. The first of the diesel simulations also over predicted the peak average combustion pressure. The effect on

combustion because of fuel property, injection rate, and spray formation differences between fuels can be visualized with the pressure curve. Pressure curves for all cases are shown in figures 23 through 27.

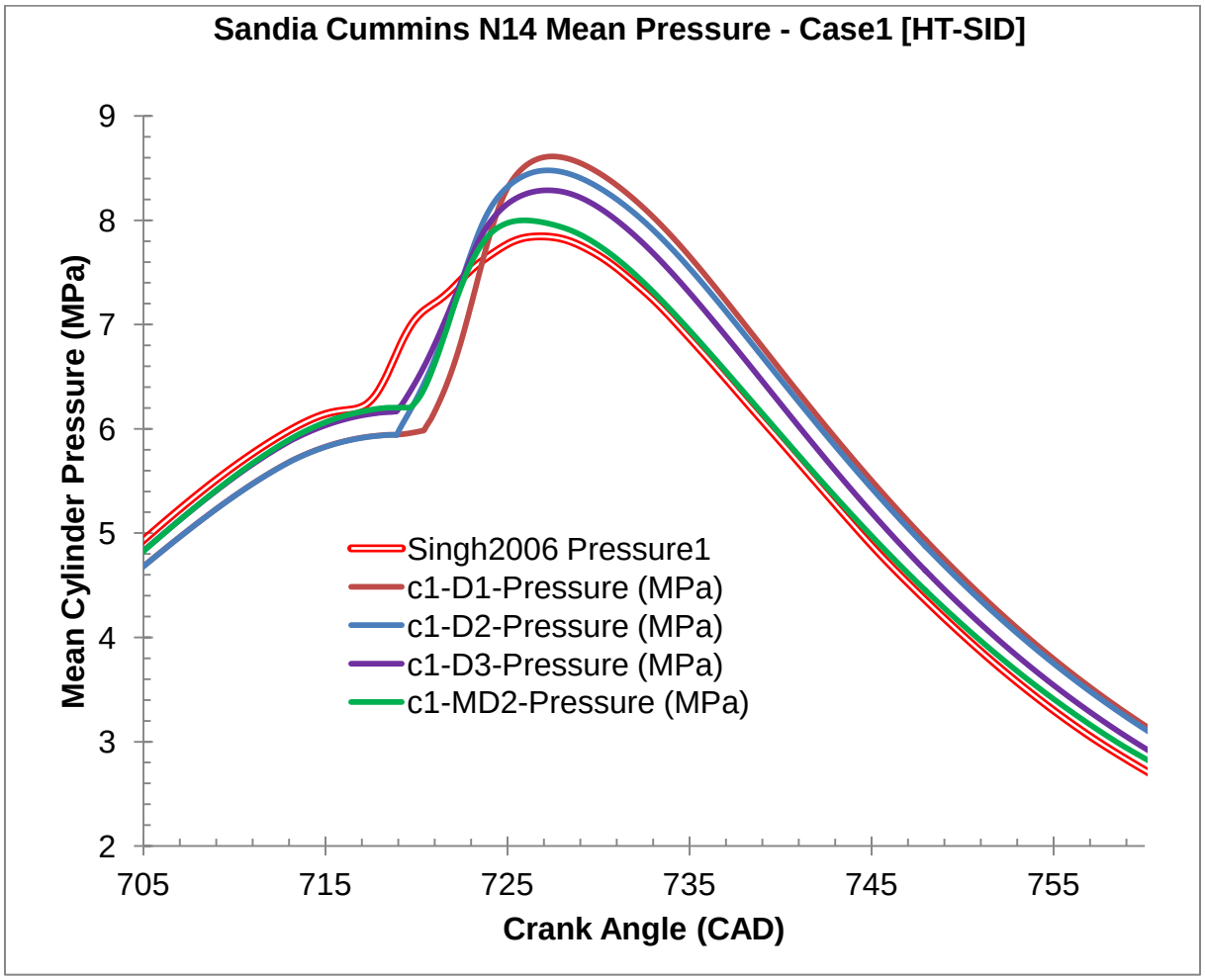


**Figure 23: Case 1, High Temperature, short ignition delay pressure curves**

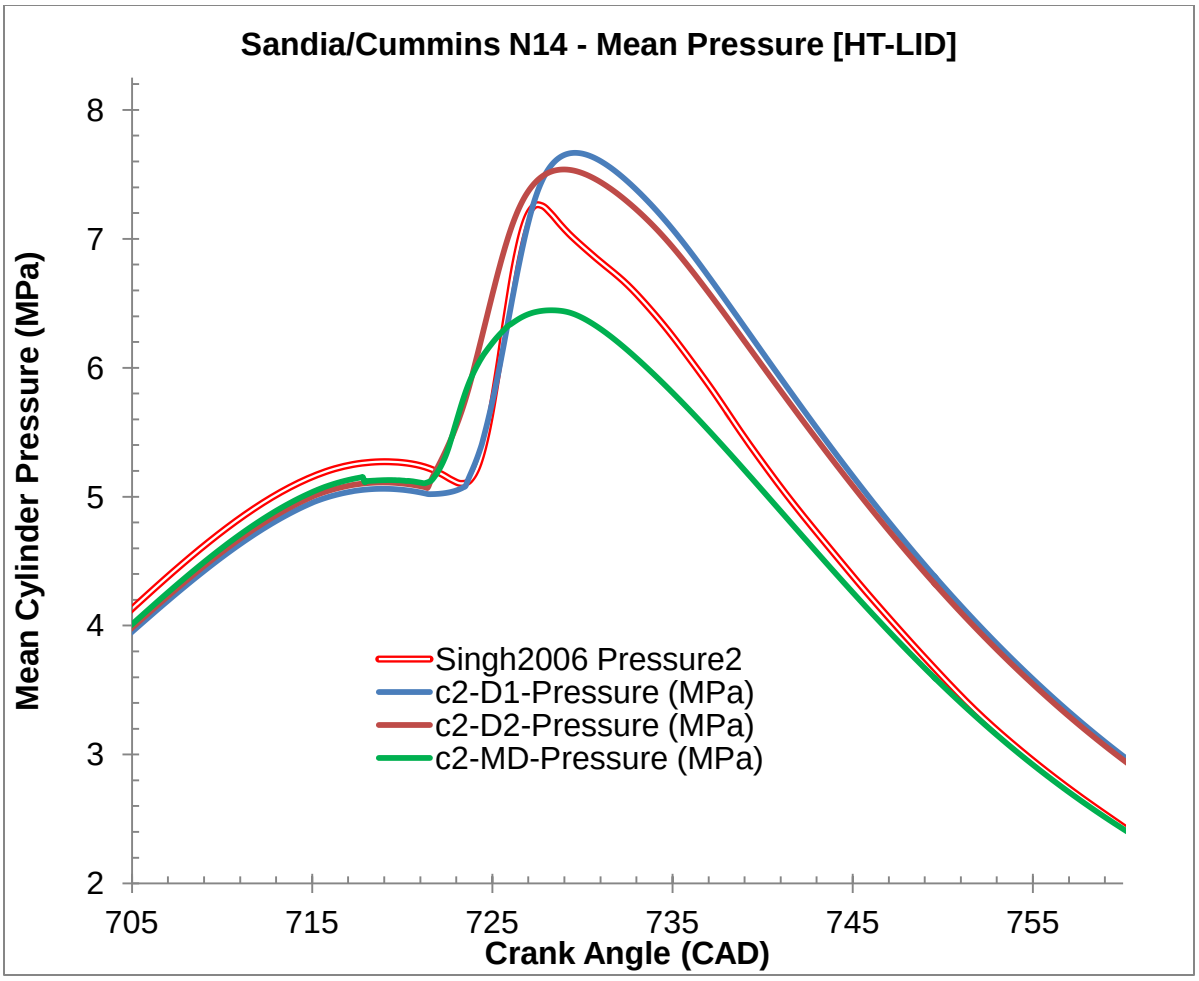


**Figure 24: Case 2, High-temperature, long ignition delay pressure curves**

For case two, the ignition delay was predicted well using the RNG k-e turbulence model for the first diesel simulation. The second diesel and methyl decanoate simulations have shorter ignition delays. Short ignition delay and high peak pressure indicate maladjustment of the autoignition model.

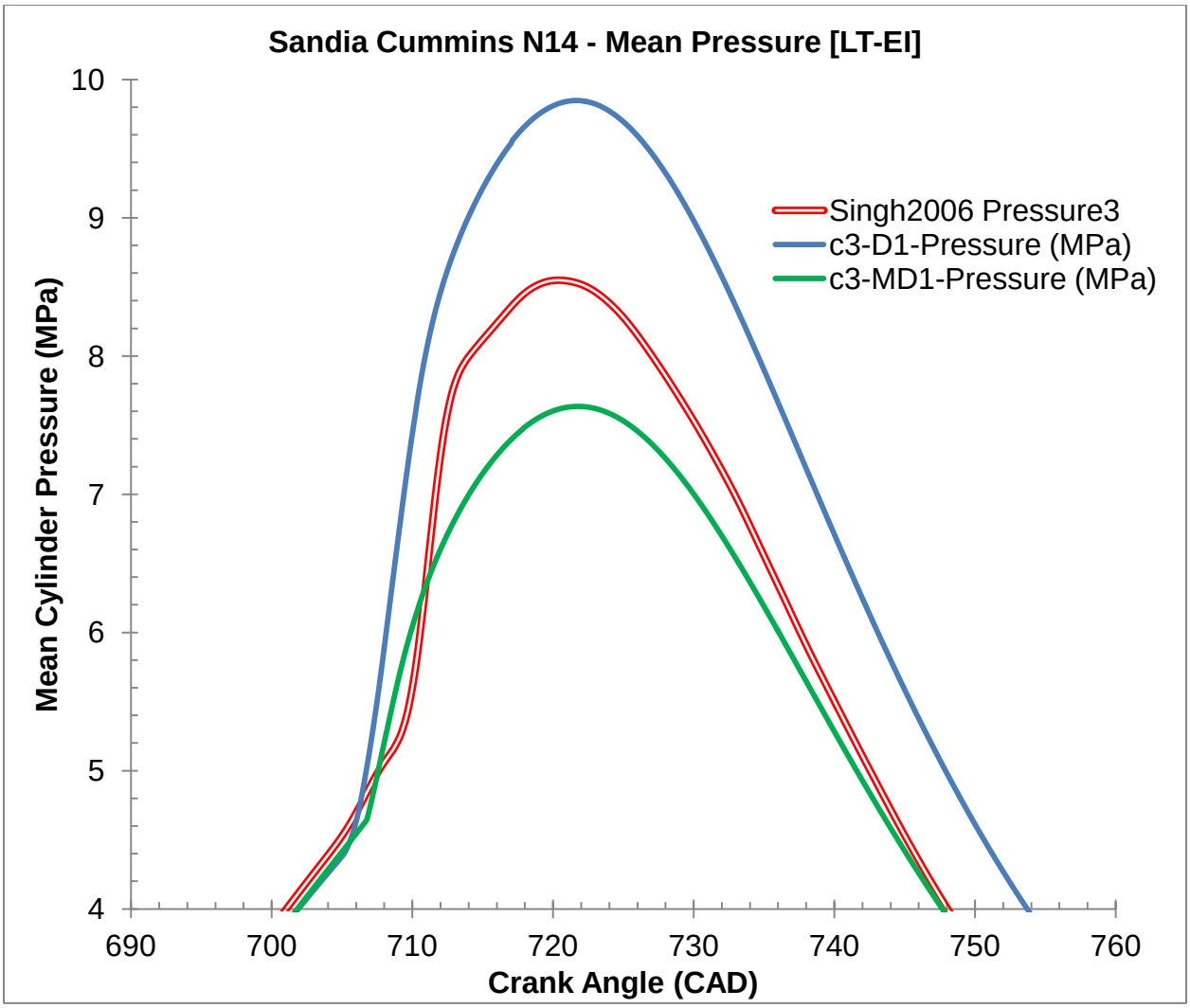


**Figure 25: Case 3, Low-temperature, early injection pressure curves**

Case three ignition delays and peak combustion pressure seem to show the effects of differing physical properties of fuels. The combustion rate of the fuels seems to be higher than the experimental data in all cases leading up to case three.

The pressure level in cases four and five match the experimental pressure curves very well. The ignition delay is smaller than that of the experimental data but, combustion rate seems to match in case  five.

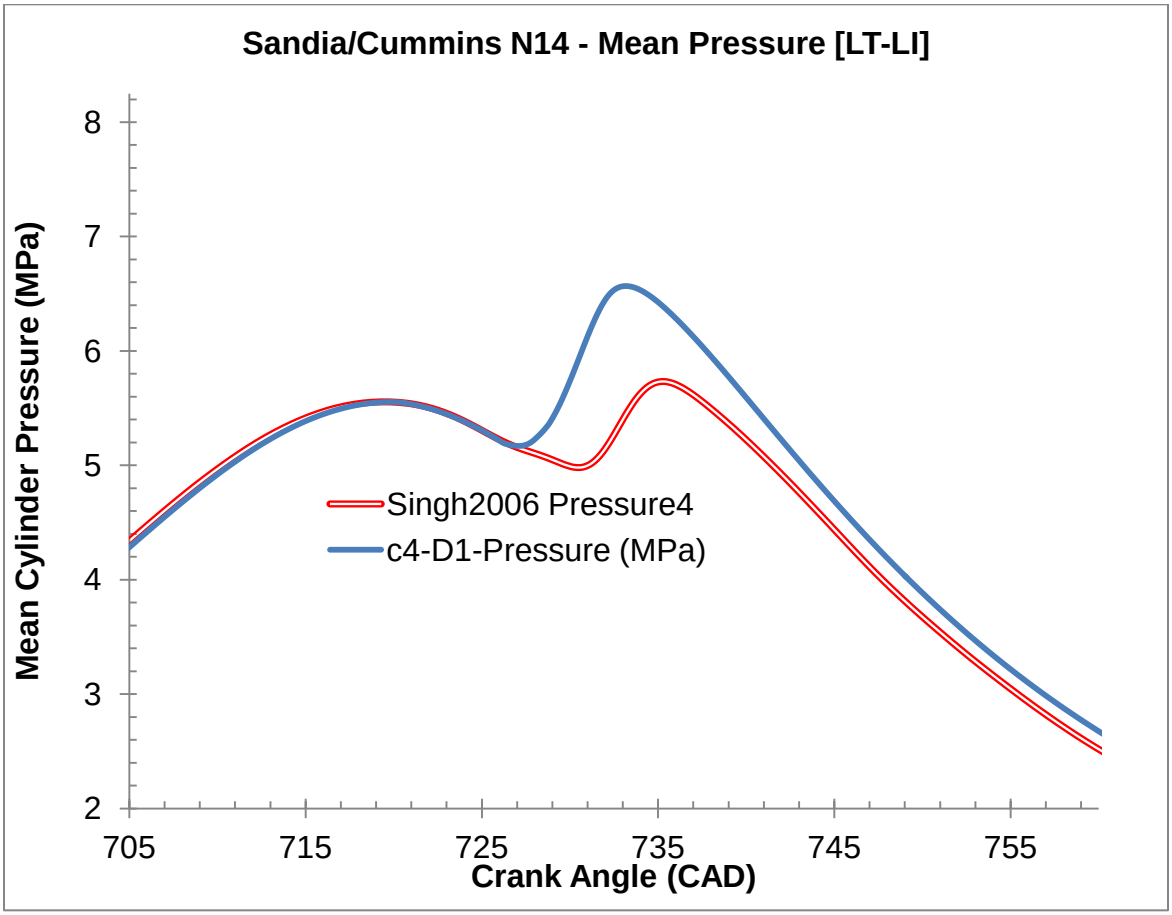


**Figure 26: Case 4, Low-temperature, late injection pressure curves**

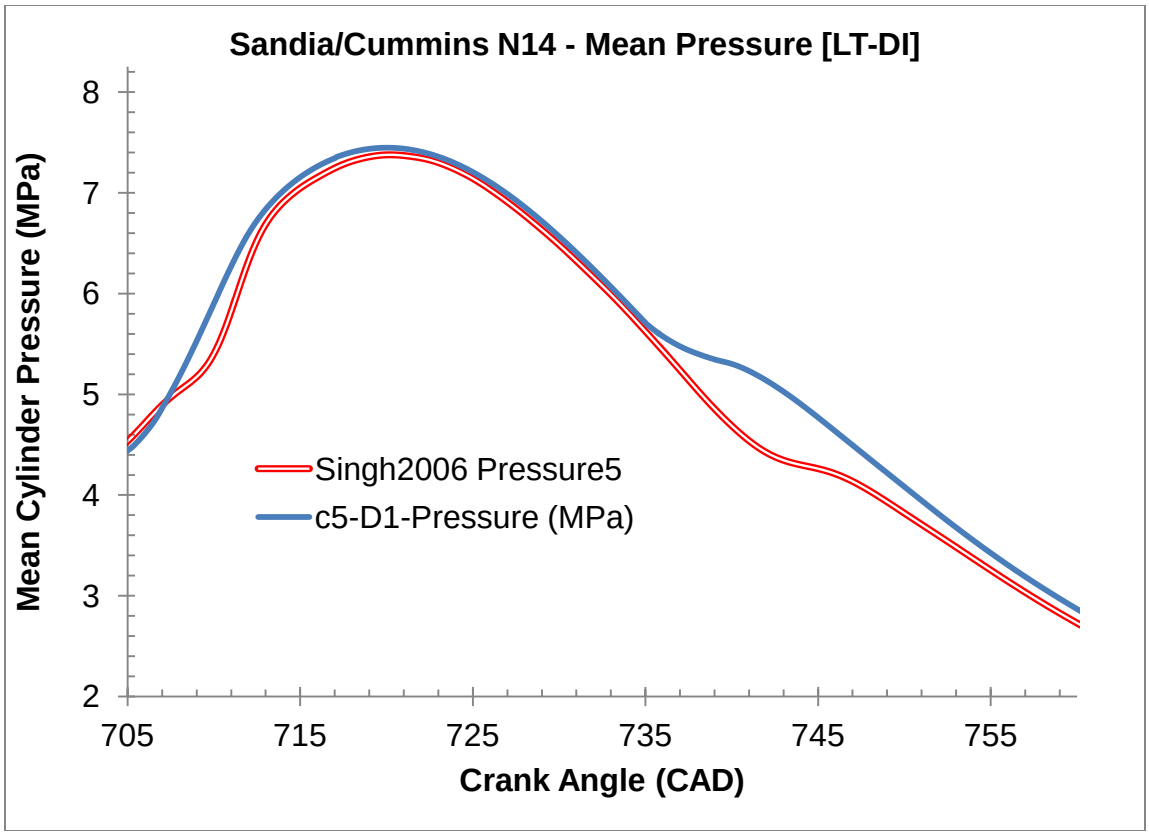


**Figure 27: Case 5, Low-temperature, double injection pressure curves**

All results could be improved by determining a method to match the experimental injection mass flow rate curves, more tuning of the droplet collision breakup model, and having accurate information about the kinematic viscosity of biodiesel. The spray model is very dependent on accurate fuel properties to determine which modes the injector nozzle is operating in. The autoignition energy of the fuels also need to be known more accurately so that the detonation and high a burn rate of the fuel does not occur. Sharp spikes in simulated pressure mean that the injector nozzle may spend more time in the flipped mode than the cavitating mode during the DOI. The accurate simulation liquid spray impingement and subsequent modes of evaporation require very fine wall mesh grids because of interaction with turbulence modeling.

### 4.1.2 Combustion Temperature

The temperature result of the simulations is compared with experimental data from Singh [15]. The adiabatic temperatures in the experimental data are calculated using STANJAN code with optical data during the soot formation and soot combustion as input. Since the experimental data is actually a theoretical calculation of maximum adiabatic flame temperature, simulation results are only provided so that general temperature trends correlations can be identified. Additional Temperature plots are in appendix B

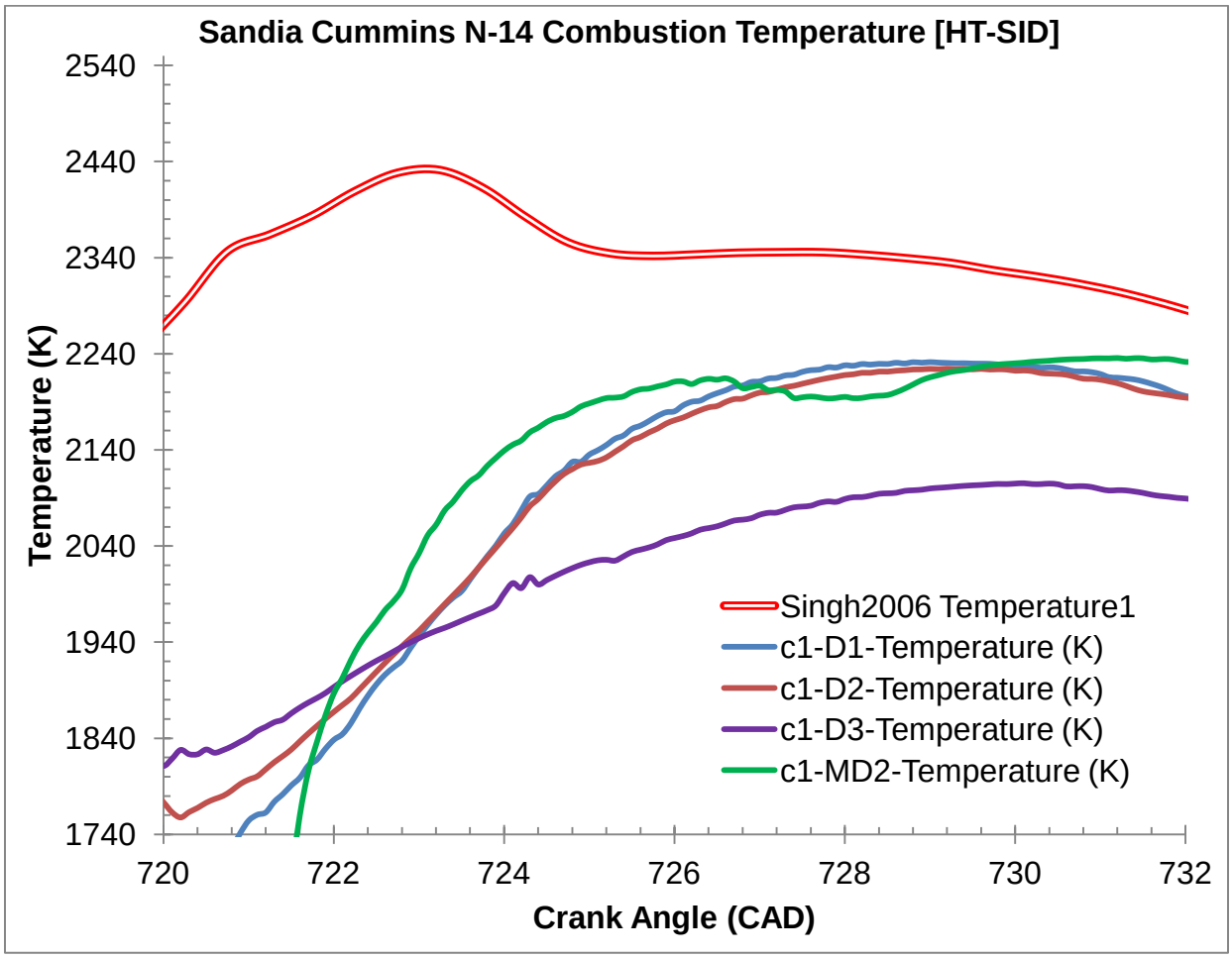


**Figure 28: Case 1, High Temperature, short ignition delay temperature curves**

### 4.2 Apparent Heat Release Rate

The AHRR curves are modeled using a single zone zero-dimensional thermodynamic model. Because of error in the temperature and pressure curves in section 4.1, the calculated maximum AHRR overshoot the experimental data significantly however, trends such as a negative AHRR at the SOI before autoignition are reproduced. Tuning of the autoignition model alone could have positive effects for the increase of accuracy. The AHRR curves for cases two, three, four, and five are in appendix B.

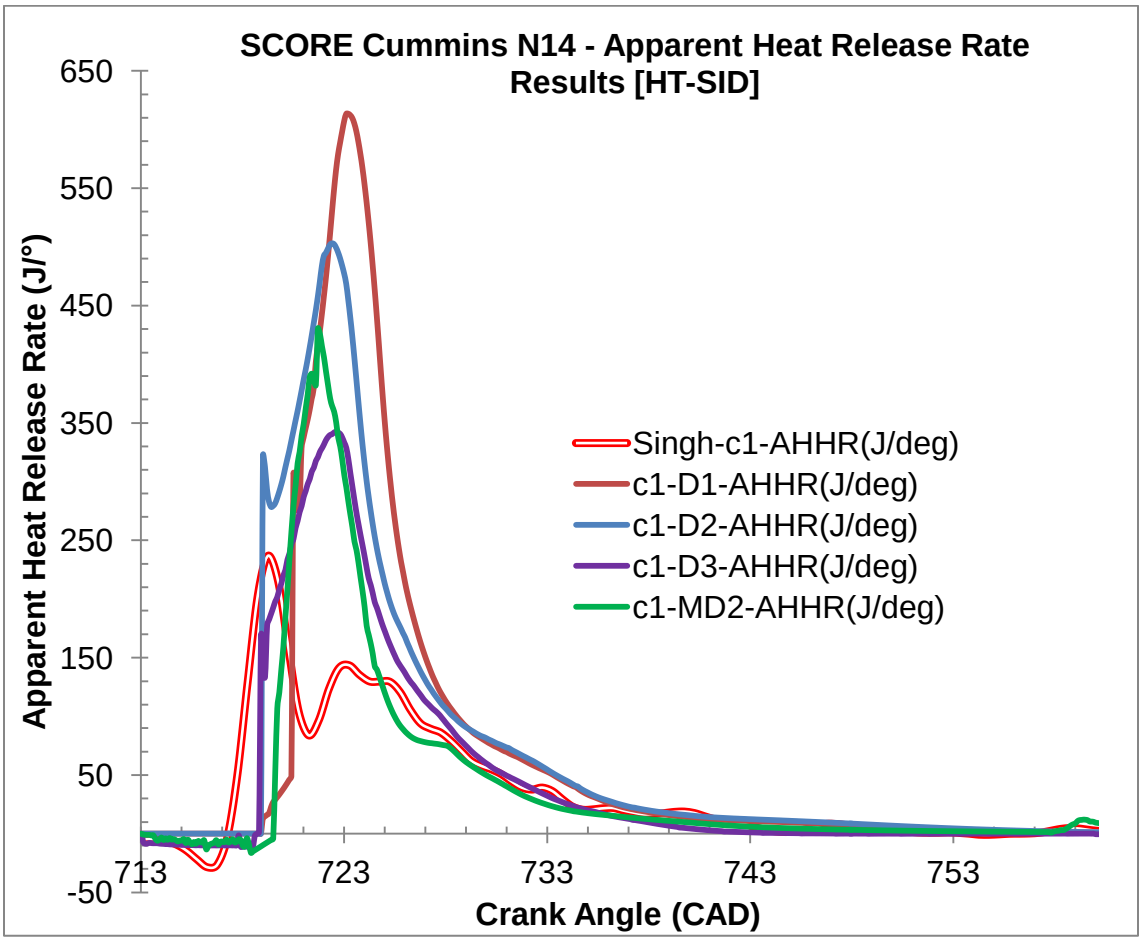


**Figure 29: Case 1, High Temperature, short ignition delay heat release curves**

### 4.3 Combustion Emissions

Given most of the published data at the time, the EPA [52] characterized the overall average trend in reduction of regulated emissions when using soy methyl ester biodiesel in heavy-duty highway engines. Figure 30 is the EPA's published emission impacts of SME on heavy duty highway engines.

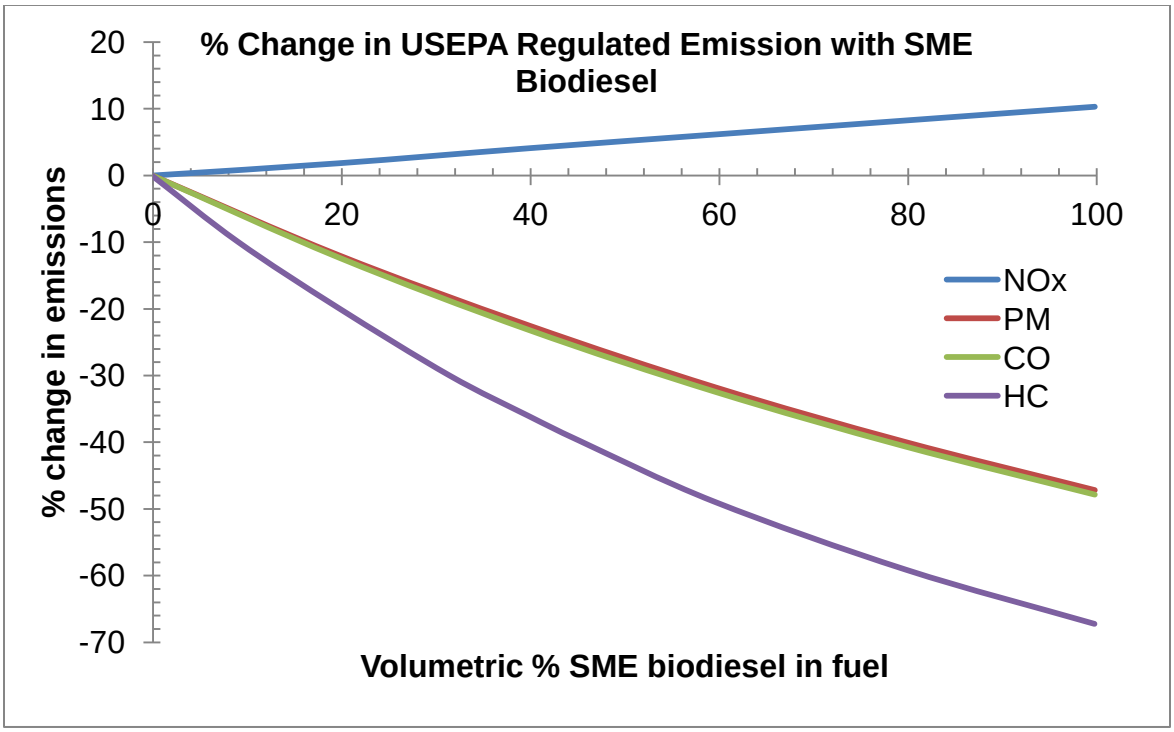


**Figure 30: Percent change in regulated emissions with SME biodiesel**

Table 5 is a comparison of $NO_x$ emissions at EVO between biodiesel and diesel fuel. The high temperature case with long ignition delay is the only case that is somewhat in agreement with the emissions trends.

**Table 5: Percent increase in $NO_x$ between simulated fuels**

| Simulated $NO_x$ at EVO (845deg) [g/(hp*hr)] or [ppm] | | | | | |
|---|---|---|---|---|---|
| | **HT-SID** | **HT-LID** | **LT-EI** | **LT-LI (ppm)** | **LT-DI (ppm)** |
| **Diesel#2** | 29.6 | 16.8 | 1 | 63 | 87.7 |
| **MD** | 5.4 | 20.9 | 0.47 | -- | -- |
| | -452% | 19.8% | -126% | -- | -- |

### 4.3.1 Unconsumed Fuel

Unconsumed fuel is a regulated pollutant in most jurisdictions. In the U.S., the EPA specifies that an on-road heavy truck or combination tractor powered by a heavy-duty compression ignition engine, such as the Cummins N14, can only emit up to $1.3g/(hp * hr)$ of unburned fuel from the exhaust. If an engine produces 100 brake horse power at speed, it could only output up to 130 grams of unconsumed fuel over the course of an hour of operation. Table five and figure 31 each depict the estimated average levels of fuel pollutants.

**Table 6: Fuel emissions at end of simulation**

| Unburnt Hydrocarbons at EVO (845deg) [g/(hp*hr)] | | | | | |
|---|---|---|---|---|---|
| | **HT-SID** | **HT-LID** | **LT-EI** | **LT-LI** | **LT-DI** |
| **Diesel#2** | 4.33E-05 | 5.75E-03 | 1.06E-04 | 1.56E-04 | 5.21E-04 |
| **MD** | 6.18E-05 | 6.87E-05 | 2.56E-02 | -- | -- |

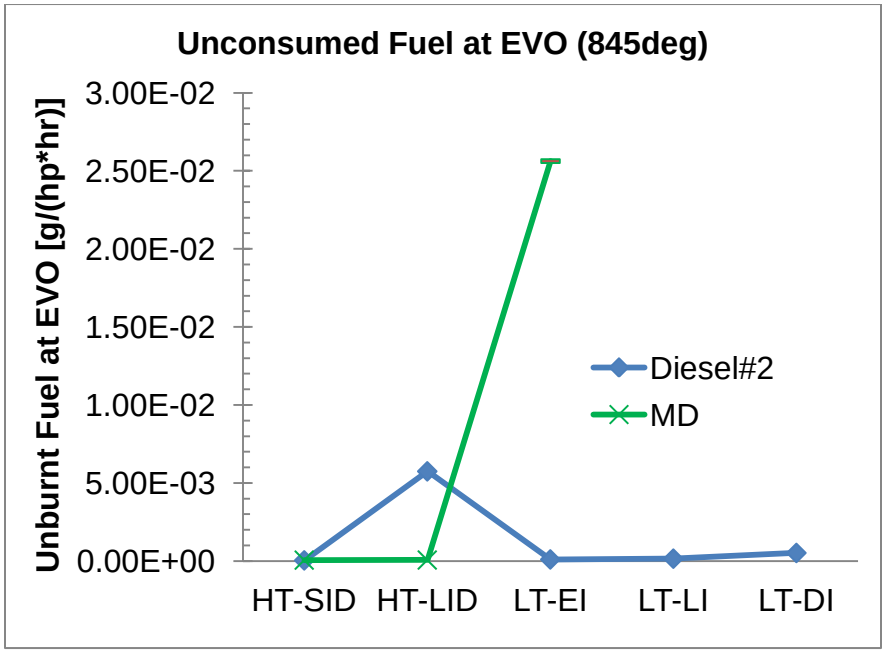


**Figure 31: Unconsumed fuel in domain at EVO**

### 4.3.2 Particulates

Soot luminosity and processing techniques were used by Singh to determine soot volume from optical experiments. The simulation results for all cases match the trend of the experimental results well. Figure 31 and table six depict the volume of soot particulates in the fuel jet.

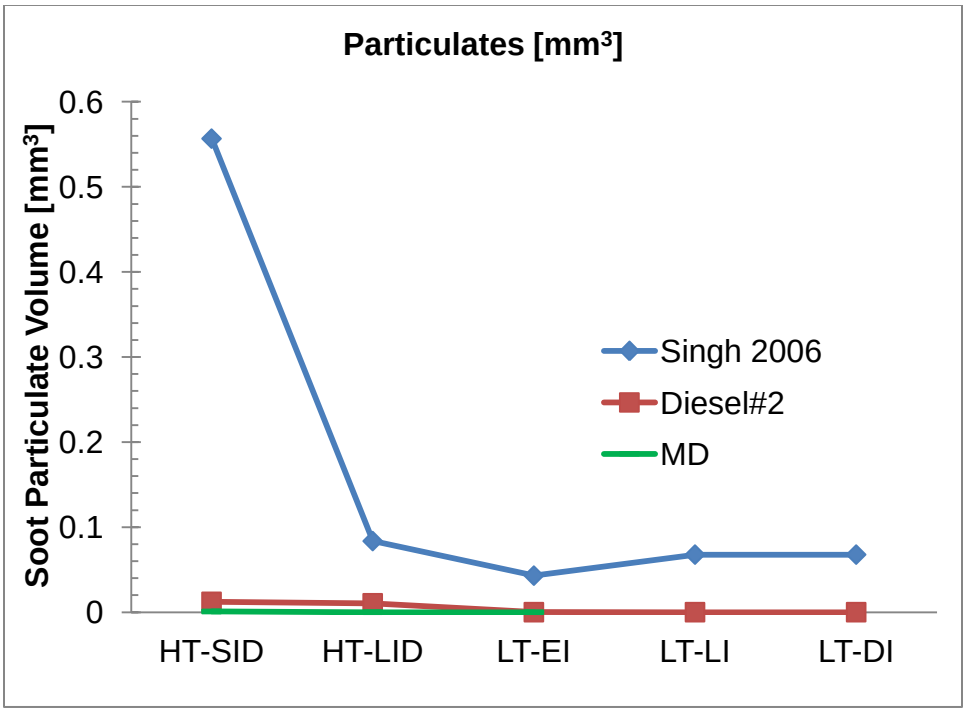


**Figure 32: Particulates in domain at EVO**

**Table 7: Particulate emissions at specified crankshaft angles**

| Particulates [mm³] | | | | | |
|---|---|---|---|---|---|
| | **HT-SID** | **HT-LID** | **LT-EI** | **LT-LI** | **LT-DI** |
| **CAD** | 725 | 728 | 715 | 741 | 755 |
| **Singh 2006** | 0.55667 | 0.08357 | 0.04296 | 0.0677 | 0.0677 |
| **Diesel#2** | 0.01213 | 0.01046 | 2.45E-05 | 1.78E-09 | 1.17E-09 |
| **MD** | 8.41E-04 | 1.18E-05 | 7.90E-09 | -- | -- |

### 4.3.3 Oxocarbons

Estimations of CO and $CO_2$ are necessary to compare combustion between regimes. $CO_2$ won't be regulated by the U.S. EPA until 2013 but, it can be used as a measure of combustion quality and aftertreatment performance during a test cycle. Table seven and figure 32 depict the estimated emitted levels of $CO_2$ from the simulated Sandia/Cummins N14.

**Table 8: Oxocarbon emissions at end of simulation**

| Oxocarbons ($CO_2$) (845deg) [g/(hp*hr)] | | | | | |
|---|---|---|---|---|---|
| | **HT-SID** | **HT-LID** | **LT-EI** | **LT-LI** | **LT-DI** |
| **Diesel#2** | 163.5 | 179.9 | 171.2 | 145.0 | 139.8 |
| **MD** | 143.3 | 144.1 | 110.7 | -- | -- |

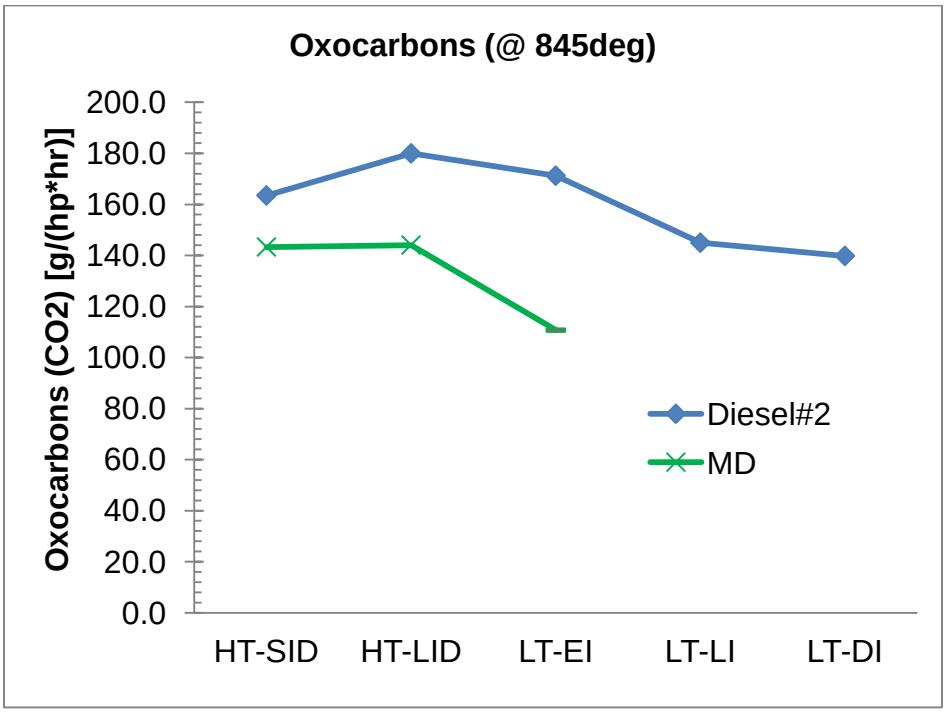


**Figure 33: Carbon dioxide in domain at EVO**

### 4.3.4 Oxides Of Nitrogen

Singh determined NOx concentration around TDC from optical experiments. The simulation results for all cases match the trend of the experimental results well. Figure 33 and table eight depict the concentration of NOx in the cylinder.

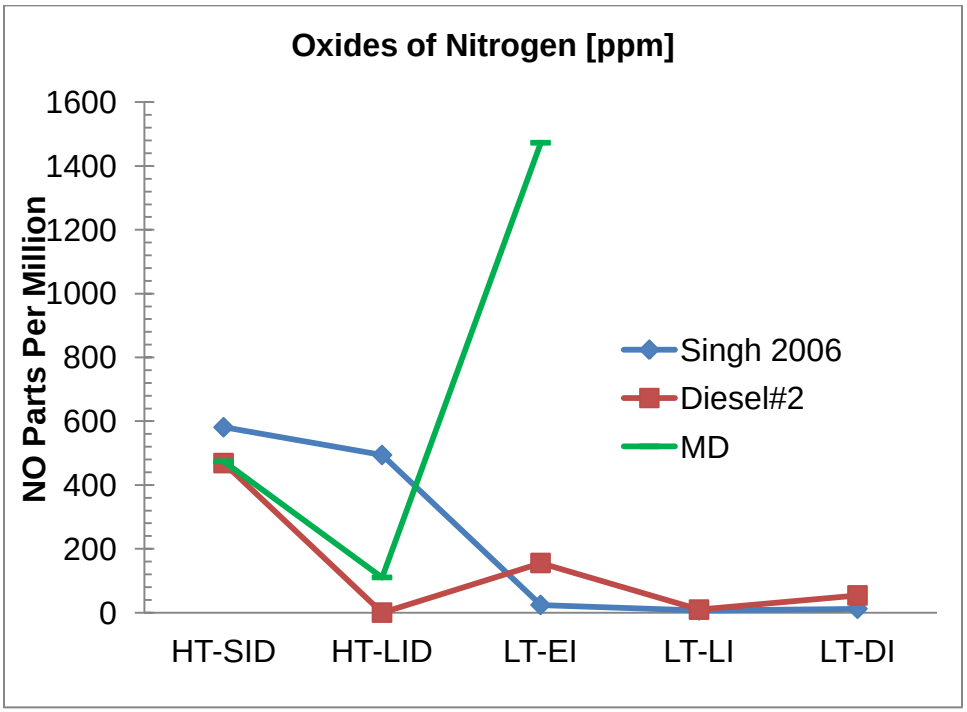


**Figure 34: Nitric oxide in domain at EVO**

**Table 9: Oxide of nitrogen concentration at top dead center**

| Oxides of Nitrogen (NO) [ppm] | | | | | |
|---|---|---|---|---|---|
| | **HT-SID** | **HT-LID** | **LT-EI** | **LT-LI** | **LT-DI** |
| **CAD** | 720 | | | | |
| **Singh 2006** | 581 | 494 | 24 | 7 | 12 |
| **Diesel#2** | 469 | 5.27E-14 | 155 | 9.3 | 53.9 |
| **MD** | 474 | 110 | 1.47E+03 | -- | -- |

It should be noted that the particulate volume predictions are completely erroneous. Adjustments to the model parameters can only be done after conducting

empirical combustion studies. Multi-step reaction mechanisms typically contain all related chemistry for pollutants such as $NO_2$ and Particulate Matter. For the purposes of aftertreatment engineering, it would be more pertinent to calculate the particle size distribution and not just volume or mass.

The mid and end of cycle $NO_x$ predictions for the various diesel cases generally follow the trend of the experimental data but, the error is very large. The mid cycle levels of $NO_x$ in the biodiesel results were consistently higher than the diesel results. It seems as though the coupled nature of all of the sub models leads to systemic error thus the autoignition model is the first on the list for tuning.

# CHAPTER 5

# CONCLUSION

## 5.1 Summary and Closing Statements

For this research work, the modeling of combustion is conducted using one step chemistry and additional pollutant models. Biodiesel physical properties are estimated using fairly sophisticated techniques to so that a model material could be created in ANSYS Fluent™ CFD. Because of the variability in material properties and combustion characteristics of biodiesel, estimations of the material properties are necessary depending on published chemical specifications. Even with more advanced chemical kinetics modeling, direct experimentation to determine fuel properties is required for simple modeling techniques to have fidelity with real engine experimental data. These engineering tools are necessary simply because of the variability of biodiesel in physical and chemical properties precludes extensive physical experimentation. The engineering value of biofuel combustion simulation, as conducted in this work, is valuable for subsystem design, piston topology, and injection strategy decisions. The estimations of $CO_2$ and unburnt hydrocarbon data at EVO can be used to size and design aftertreatment subsystems if validated. The simulation methods and models must be perfected given the large error of some of the results.

The average compute time for one simulation without advanced species transport and kinetics was around 5 weeks given license limitations and turbulence modeling. The requirement of convergence and extended solution stability between timesteps increases overall compute time beyond 5 weeks. In the future, to reduce

costs, more accurate chemical kinetics will need be employed using open source CFD software such as OpenFOAM®. Because the user can alter the code and add sub models, the addition of more advanced injected spray and breakup models such as the one proposed by Turner et al. [66] is possible. The computational resources needed are considerable and such simulations require high performance cluster computers to keep compute times reasonable. The parallel licensing and load control software fees would be reduced or eliminated using open source software. Streamlining and optimization of solver code is also possible so that computational speed can be maintained on cheaper hardware.

## BIBLIOGRAPHY

[1] G. Toscano and D. Duca, "RENEWABLE ENERGY CONTENT OF FATTY ACID METHYL ESTERS (FAME) AND GLYCEROL," *Journal of Agricultural Engineering,* vol. 4, pp. 47-53, 2009.

[2] *EPA and NHTSA Adopt First-Ever Program to Reduce Greenhouse Gas Emissions and Improve Fuel Efficiency of Medium- and Heavy-Duty Vehicles,* 2011.

[3] J. Kortendijk, "Measurement of Piston Ring Temperature," 2005.

[4] G.-J. Wang, C.-J. Chiang, Y.-H. Su and Y.-Y. Ku, *CFD Modeling of a Turbo-charged Common-rail Diesel Engine,* 2013.

[5] T. M. Belal, E. S. M. Marzouk and M. M. Osman, "Investigating Diesel Engine Performance and Emissions Using CFD," *Energy and Power Engineering,* vol. 5, pp. 171-180, 2013.

[6] C. Felsch, "Combustion Modeling for Diesel Engine Control Design," 2009.

[7] L. Liang, C. V. Naik, K. Puduppakkam, C. Wang, A. a. M. E. Modak, H.-W. Ge, R. Reitz and C. Rutland, "Efficient Simulation of Diesel Engine Combustion Using Realistic Chemical Kinetics in CFD," 2010.

[8] J. B. Heywood, Internal Combustion Engine Fundamentals, A. Duffy and J. M. Morriss, Eds., McGraw-Hill, Inc., 1988, pp. 491-566.

[9] R. Demory, "Optical Measurement of Nitric Oxide and Hydroxyl Radicals Distributions in Combusting Diesel Sprays," 2007.

[10] P. F. Flynn, R. P. Durrett, G. L. Hunter, A. O. zur Loye, O. Akinyemi, J. E. Dec and C. K. Westbrook, "Diesel Combustion: An Integrated View Combining Laser Diagnostics, Chemical Kinetics, and Empirical Validation," Lawrence Livermore Natiolnal Laboratory, 1999.

[11] *Health Assessment Document For Diesel Engine Exhaust,* 2002.

[12] D. Videos, 2014. [Online]. Available: https://www.youtube.com/watch?v=-yKGzcv2DyU. [Accessed 28 February 2014].

[13] USA Trucks Direct, "http://www.usatrucksdirect.com/," 2013. [Online]. Available: http://www.usatrucksdirect.com/part/1/CUMMINS+USED+N14. [Accessed 22 January 2013].

[14] J. O'Connor and M. Musculus, "Effect of Load on Close-Coupled Post-Injection Efficacy for Soot Reduction in an Optical Heavy-Duty Diesel Research Engine," *Journal of Engineering for Gas Turbines and Power,* vol. 136, no. 10, 2014.

[15] S. Singh, "Experimental Investigation of Multi-Mode Diesel Engine Combustion and Validation of Advanced Combustion Models," 2006.

[16] John Deere, [Online]. Available: http://www.deere.com/en_US/docs/zmags/agriculture/online_brochures/emissions/ft4.html.

[17] E. Alptekin and M. Canakci, "Determination of the density and the viscosities of biodiesel-diesel fuel blends," *Renewable Energy,* vol. 33, pp. 2623-2630, 2008.

[18] B. R. Moser, "Biodiesel production, properties, and feedstocks," 2009.

[19] Home Biodiesel Kits, [Online]. Available: http://www.homebiodieselkits.com/frfuspl.html.

[20] Y. Li and C. Wan, "Algae for Biofuels," 2011.

[21] A. Keskin, M. Guru, D. Altiparmak and K. Aydin, "Using of cotton oil soapstock biodiesel–diesel fuel blends as an alternative diesel fuel," *Renewable Energy,* vol. 33, pp. 553-557, 2008.

[22] S. Singh and D. Singh, "Biodiesel production through the use of different sources and characterization of oils and their esters as the substitute of diesel: A review," *Renewable and Sustainable Energy Reviews,* vol. 14, pp. 200-216, 2010.

[23] G. Knothe, R. O. Dunn and M. O. Bagby, "Biodiesel: The Use of Vegetable Oils and Their Derivatives as Alternative Diesel Fuels," 2005.

[24] P. Cao, M. A. Dube and A. Y. Tremblay, "High-purity fatty acid methyl ester production from canola, soybean, palm, and yellow grease lipids by means of a membrane reactor," *Biomass and Energy,* vol. 32, pp. 1028-1036, 2008.

[25] W. Ning, R. D. Reitz, A. M. Lippert and R. Diwakar, "Development of a Next-generation Spray and Atomization Model Using an Eulerian-Lagrangian Methodology," 2007.

[26] D. K. Seshadri, "Chemical Kinetic Characterization of Autoignition and Combustion of Diesel and JP-8," 2003.

[27] C. Crua, D. A. Kennaird, S. S. Sazhin, M. R. Heikal and M. R. Gold, "Diesel autoignition at elevated in-cylinder pressures," *International Journal of Engine Research,* vol. 5, pp. 365-374, 2004.

[28] O. Penyazkov, K. Sevrouk1, V. Tangirala and N. Joshi, "Autoignitions of Diesel Fuel/Air Mixtures Behind Reflected Shock Waves," 2009.

[29] J. Farrell, N. Cernansky, F. Dryer, D. Friend, C. Hergart, C. K. Law, R. McDavid, C. Mueller, A. Patel and H. Pitsch, "Development of an Experimental Database and Kinetic Models for Surrogate Diesel Fuels," 2007.

[30] M. R. Harper, "Automated reaction mechanism generation: Data collaboration, Heteroatom implementation, and Model validation," 2011.

[31] R. Seiser and K. Seshadir, "Chemical kinetic charictarization of model fuels for describing combustion of diesel," 2003.

[32] H. J. Curran, P. Gaffuri, W. J. Pitz and C. K. Westbrook, "A Comprehensive Modeling Study of n-Heptane Oxidation," *Combustion and Flame,* vol. 144, pp. 149-177, 1998.

[33] O. Herbinet, W. J. P. a and C. K. Westbrook, "Detailed chemical kinetic mechanism for the oxidation of biodiesel fuels blend surrogate," *Combustion and Flame,* vol. 157, pp. 893-908, 2010.

[34] Z. Luo, M. Plomer, T. Lu, S. Som, D. E. Longman and S. a. P. W. J. Sarathy, "A reduced mechanism for biodiesel surrogates for compression ignition engine applications," *Fuel,* vol. 99, pp. 143-153, 2012.

[35] A. Saha, "VAPORIZATION CHARACTERISTICS OF PURE AND BLENDED BIOFUEL DROPLET INJECTED INTO HOT STREAM OF AIR," 2006.

[36] A. Dorri, A. Lamani and A. Hoxha, "INFLUENCE OF HOLE GEOMETRY IN THE CAVITATION PHENOMENA OF DIESEL INJECTORS, A NUMERICAL INVESTIGATION," *Fuels and Lubricants,* vol. 48(3), pp. 361-371, 2009.

[37] C. Westbrook, C. N. b, O. Herbinet, W. Pitz, M. Mehl, S. Sarathy and H. Curran, "Detailed chemical kinetic reaction mechanisms for soy and rapeseed biodiesel fuels," *Combustion and Flame,* vol. 158, pp. 742-755, 2011.

[38] S. L. Kokjohn and R. D. Reitz, "Investigation of the Roles of Flame Propagation, Turbulent Mixing, and Volumetric Heat Release in Conventional and Low Temperature Diesel Combustion," *Journal of Engineering for Gas Turbines and Power,* vol. 133, p. 10, 2011.

[39] U. Maas and S. B. Pope, "Implementation of simplified chemical kinetics based on intrinsic low–dimensional manifolds.," 1992.

[40] K. E. Niemeyer, M. P. Raju and C. J. Sung, "Skeletal Mechanism Generation for Surrogate Fuels Using Directed Relation Graph with Error Propagation and Sensitivity Analysis," 2009.

[41] T. Nagy and T. Turányi, "Reduction of very large reaction mechanisms using methods based on simulation error minimization," *Combustion and Flame,* vol. 156, p. 417?428, 2009.

[42] H. K. Ng, S. Gan, J.-H. Ng and K. M. Pang, "Development and validation of a reduced combined biodiesel–diesel reaction mechanism," *Fuel,* vol. 104, p. 620–634, 2013.

[43] J. L. Brakora, Y. Ra and R. D. Reitz, "Combustion Model for Biodiesel-Fueled Engine Simulations using Realistic Chemistry and Physical Properties," 2011.

[44] S. Singh, R. Reitz, M. Musculus and T. Lachaux, "Validation of engine combustion models against detailed in-cylinder optical diagnostics data for a heavy-duty compression-ignition engine," *International Journal of Engine Research,* vol. 8, pp. 97-126, 2007.

[45] J. L. Brakora, "A COMPREHENSIVE COMBUSTION MODEL FOR BIODIESEL-FUELED ENGINE SIMULATIONS," 2012.

[46] J.-V. Koo and J. K. Martin, "Droplet Sizes and Velocities in a Transient Diesel Fuel Spray," 1990.

[47] D. Kennaird, C. Crua, J. Lacoste, M. Heikal, M. Gold and N. Jackson, "In-Cylinder Penetration and Break-Up of Diesel Sprays Using a Common-Rail Injection System," 2002.

[48] R. Payri, F. Salvador, J. Gimeno and J. de la Morena, "Effects of nozzle geometry on direct injection diesel engine combustion process," *Applied Thermal Engineering,* vol. 29, p. 2051–2060, 2008.

[49] N. Abani and R. D. Reitz, "A Model to Predict Spray-tip Penetration for Time-varying Injection Profiles," in *ILASS Americas, 20th Annual Conference on Liquid Atomization and Spray Systems*, 2007.

[50] J. Li, W. Yang, H. An, A. Maghbouli and S. Chou, "Effects of piston bowl geometry on combustion and emission characteristics of biodiesel fueled diesel engines," *Fuel,* vol. 120, pp. 66-73, 2014.

[51] L. G. Schumacher, S. C. Borgelt, D. Fosseen, W. G. C and W. G. Hiresa, "HEAVY-DUTY ENGINE EXHAUST EMISSION TESTS USING METHYL ESTER SOYBEAN OIL/DIESEL

FUEL BLENDS," *Bioresource Technology,* vol. 57, pp. 31-36, 1996.

[52] *A Comprehensive Analysis of Biodiesel Impacts on Exhaust Emissions,* 2002.

[53] A. S. Cheng, A. Upatnieks and C. J. Mueller, "Investigation of the impact of biodiesel fuelling on NOx emissions using an optical direct injection diesel engine," *International Journal of Engine Research,* vol. 7, pp. 297-318, 2006.

[54] C. J. Mueller, A. L. Boehman? and G. C. Martin, "An Experimental Investigation of the Origin of Increased NOx Emissions When Fueling a Heavy-Duty Compression-Ignition Engine with Soy Biodiesel," 2009.

[55] W. Yuan and A. C. Hansen, "Computational investigation of the effect of biodiesel fuel properties on diesel engine NOx emissions," *Internationa Journal of Agricultural and Biological Engineering,* vol. 2(2), pp. 41-48, 2009.

[56] M. N. Nabi, M. M. Rahman and M. S. Akhter, "Biodiesel from cotton seed oil and its effect on engine performance and exhaust emissions," *Applied Thermal Engineering,* vol. 29, pp. 2265-2270, 2009.

[57] I. Barabás, A. Todorut and D. Baldean, "Performance and emission characteristics of an CI engine fueled with diesel biodiesel bioethanol blends," *Fuel,* vol. 89, pp. 3827-3832, 2010.

[58] B. Tesfa, R. Mishra, F. Gu and N. Powles, "Prediction models for density and viscosity of biodiesel and their effects on fuel supply system in CI engines," *Renewable Energy,* vol. 35, pp. 2752-2760, 2010.

[59] A. Haseeb, T. Jun, M. Fazal and H. Masjuki, "Degradation of physical properties of different elastomers upon exposure to palm biodiesel," *Energy,* vol. 36, pp. 1814-1819, 2011.

[60] J. Pastor, J. García-Oliver, J.-G. Nerva and B. Giménez, "Fuel effect on the liquid-phase penetration of an evaporating spray under transient diesel-like conditions," *Fuel,* vol. 90, p. 3369–3381, 2011.

[61] R. Tate, K. Watts, C. Allen and K. Wilkie, "The densities of three biodiesel fuels at temperatures up to 300C," *Fuel,* vol. 85, pp. 1004-1009, 2006.

[62] N. D. L. D. Silva, C. B. Batistella, R. M. Filho and M. R. W. Maciel, "Investigation of Biofuels Properties," 2008.

[63] E. Alptekin and M. Canakci, "Characterization of the key fuel properties of methyl ester–diesel fuel blends," *Fuel,* vol. 88, pp. 75-80, 2009.

[64] L. F. Ramírez-Verduzco, B. E. García-Flores, J. E. Rodríguez-Rodríguez and A. del Rayo Jaramillo-Jacob, "Prediction of the density and viscosity in biodiesel blends at various temperatures," *Fuel,* vol. 90, p. 1751–1761, 2011.

[65] R. E. Tate, K. C. Watts, C. A. W. Allen and K. I. Wilkie, "The viscosities of three biodiesel fuels at temperatures up to 300 degC," *Fuel,* vol. 85, pp. 1010-1015, 2006.

[66] Y. Su, "Selection of Prediction Methods for Thermophysical Properties for Process Modeling and Product Design of Biodiesel Manufacturing," 2011.

[67] K. M. Doll, B. R. Moser and S. Z. Erhan, "Surface Tension Studies of Alkyl Esters and Epoxidized Alkyl Esters Relevant to Oleochemically Based Fuel Additives," *Energy \& Fuels,* vol. 21, pp. 3044-3048, 2007.

[68] S. M. Akers, J. L. Conkle, S. N. Thomas and K. B. Rider, "Determination of the Heat of Combustion of Biodiesel Using Bomb Calorimetry," *Journal of Chemical Education,* vol. 83(2), pp. 260-262, 2006.

[69] J. Goodrum, "Volatility and boiling points of biodiesel from vegetable oils and tallow," *Biomass and Energy,* vol. 22, pp. 205-211, 2002.

[70] R. C. Reid, J. M. Prausnitz and B. E. Poling, The Properties of Gases and Liquids 4th Edition, B. Sun and G. H. Fleck, Eds., McGraw-Hill, Inc., 1987.

[71] B. E. Poling, J. M. Prausnitz and J. P. O'Connell, The Properties of Gases and Liquids, Fifth Edition, McGraw-Hill, Inc., 2004.

[72] M. Turner, S. Sazhin, J. Healey, C. Crua and S. Martynov, "A breakup model for transient Diesel fuel sprays," *Fuel,* vol. 97, pp. 288-305, 2012.

# APPENDIX A

Assorted Biodiesel Properties.

**Table 10: Individual boiling points of common biodiesel components**

| Methyl Ester Boiling Point and Molecular Mass | | |
|---|---|---|
| **Methyl Ester CX:Y [a]** | **M(kg/kmol)** | **$T_b$(K)** |
| methyl palmitate C16:0 | 270.450714 | 605.271 |
| methyl stearate C18:0 | 298.503815 | 628.666 |
| methyl oleate C18:1 | 296.487915 | 624.598 |
| methyl linoleate C18:2 [b] | 294.472107 | 667.15 |
| methyl linolenate C18:3 [b] | 292.456207 | 637.56 |
| a:X=# of C atoms in chain : Y=# of double bonds in chain | | |
| b: Boiling Points are estimates based on ACD/PhysChem. All @760mmHg | | |

**Table 11: Common biodiesel component enthalpies of formation**

| SME Enthalpy of Formation | | |
|---|---|---|
| **ME** | **%Moles in SME** | **$\Delta h_f°$(J/kmol)** |
| **C16:0** | 12% | -7.117E+08 |
| **C18:0** | 5% | -7.510E+08 |
| **C18:1** | 25% | -6.280E+08 |
| **C18:2** | 52% | -5.117E+08 |
| **C18:3** | 6% | -3.916E+08 |
| | **M(kg/kmol)** | **$\Delta h_f°$ (J/kmol)** |
| | **292.1** | -1.140E+08 |

**Table 12: Individual biodiesel component critical properties**

| Predicted Methyl Ester Constituent Critical Properties | | | | | |
|---|---|---|---|---|---|
| | **C16:0** | **C18:0** | **C18:1** | **C18:2** | **C18:3** |
| **$T_c$(K)** | 764.2 | 782.6 | 779.4 | 834.6 | 799.6 |
| **$P_c$(Pa)** | 1.399E+06 | 1.270E+06 | 1.295E+06 | 1.322E+06 | 1.350E+06 |
| **$V_c$($m^3$/kg)** | 0.003740 | 0.003764 | 0.003911 | 0.004060 | 0.004211 |

**Table 13: Combined critical properties of SME biodiesel**

| Predicted Critical Properties of SME | |
|---|---|
| $T_{cm}$(K) | 774.8 |
| $P_{cm}$(Pa) | 1.269E+06 |
| $V_{cm}$($m^3$/kg) | 0.003685 |

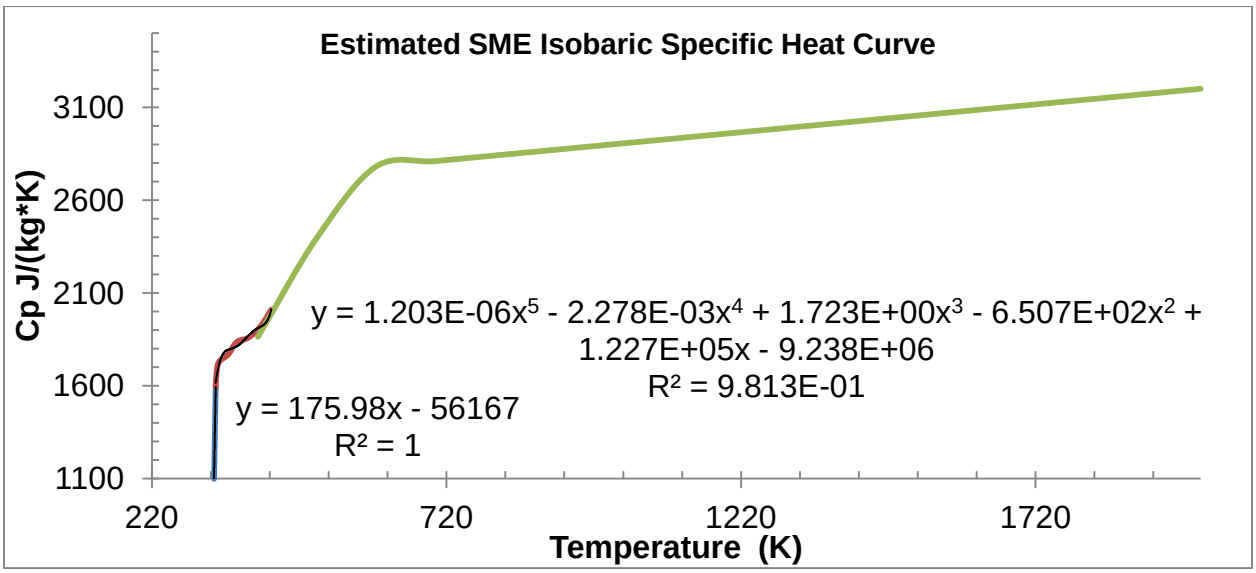


**Figure 35: Predicted SME isobaric specific heat curve**

**Table 14: Fluent material properties for simulated fuels**

| | **methyl decanoate** | **n-decane** | **n-heptane** |
|---|---|---|---|
| | **$C_{11}H_{22}O_2$** | **$C_{10}H_{22}$** | **$C_7H_{16}$** |
| **Droplet Material Properties** | | | |
| **Density (kg/m^3)** | ~860.5 | 730 | 684 |
| **Specific Heat (J/kg*K)** | ~1098 | 2090 | 2219 |
| **Thermal Conductivity (W/m*K)** | ~0.159-0.171 | 0.149 | 0.14 |
| **Dynamic Viscosity (kg/m*s) or (Pa*s)** | 0.0081328 | 0.0024 | 0.000409 |
| **Latent Heat (j/kg) @Vaporization** | ~325000 | 277000 | 320096 |
| **Vaporization Temperature @aP (K)** | ~638 | 341 | 271 |
| **Boiling Point @aP (K)** | 588-623 | 447 | 371 |
| **Volatile Component Fraction (%)** | 95.0-99.5 | 100 | 100 |
| **Binary Diffusivity (m^2/s)** | --- | 3.79E-06 | 6.31E-06 |
| **Saturation Vapor Pressure @STaP (Pa)** | 1950 | 1100 | 5316 |
| **Heat of Pyrolysis (j/kg)** | --- | --- | --- |
| **Droplet Surface Tension (n/m)** | **~0.025801** | 0.0263257 | 0.0198263 |
| | | | |
| | | | |
| **Vapor Material Properties** | | | |
| **Density (kg/m^3)** | 5.22 | 4.5 | 4.25 |
| **Specific Heat (J/kg*K)** | ~1835.0515 | 1555.7 | 2471 |
| **Thermal Conductivity (W/m*K)** | 0.0169 | 0.0178 | 0.0178 |
| **Dynamic Viscosity (kg/m*s) or (Pa*s)** | 0.0027136 | 7.00E-06 | 7.00E-06 |
| **Molecular Weight (kg/kmol)** | 186.291184 | 142.284 | 100.204 |
| **Standard State Enthalpy (j/kg*mol)** | **-1.140E+08** | -2.50E+08 | -1.88E+08 |
| **Standard State Entropy (j/kmol*K)** | 246719.51 | 540531.0 | 428006.3 |
| **Reference Temperature (K)** | 298.15 | 2.9815E+02 | 298.15 |
| **Critical Temperature (K)** | **774.8** | 617.7 | 617.7 |
| **Critical Pressure (Pa)** | **1.2686E+06** | 2110000 | 2110000 |
| **Critical Specific Volume (m^3/kg)** | **0.0036947** | 0.004386 | 0.004386 |
| **Acentric Factor** | **0.23** | 0.49 | 0.49 |

Custom Field Function .scm file text:

```
(custom-field-function/define
 '(((name swirl-number) (display "tangential-velocity / sqrt (x ^ 2 + y ^ 2) / 125.66") (syntax-tree ("/" ("/" "tangential-velocity" ("sqrt" ("+" ("**" "x-coordinate" 2) ("**" "y-coordinate" 2)))) 125.66)) (code (field-/ (field-/ (field-load "tangential-velocity") (field-sqrt (field-+ (field-** (field-load "x-coordinate") 2) (field-** (field-load "y-coordinate") 2)))) 125.66)))
   ((name nox-ppm) (display "(molef-pollut-pollutant-0 * 10 ^ 6) / (1 - (soot-mole-fraction + molef-co2 + molef-h2o + molef-n2))") (syntax-tree ("/" ("*" "molef-pollut-pollutant-0" 1000000.) ("-" 1 ("+" ("+" ("+" "soot-mole-fraction" "molef-co2") "molef-h2o") "molef-n2")))) (code (field-/ (field-* (field-load "molef-pollut-pollutant-0") 1000000.) (field-- 1 (field-+ (field-+ (field-+ (field-load "soot-mole-fraction") (field-load "molef-co2")) (field-load "molef-h2o")) (field-load "molef-n2"))))))
   ((name adj-pressure) (display "p + 101325") (syntax-tree ("+" "pressure" 101325)) (code (field-+ (field-load "pressure") 101325)))
   ((name soot-vol) (display "soot-volume-fraction * cell-volume") (syntax-tree ("*" "soot-volume-fraction" "cell-volume")) (code (field-* (field-load "soot-volume-fraction") (field-load "cell-volume"))))
   ((name heat-release-rate) (display "heat-of-reaction * (8 / 7200)") (syntax-tree ("*" "heat-of-reaction" 0.001111111111111111)) (code (field-* (field-load "heat-of-reaction") 0.001111111111111111)))
   ((name co2-mass) (display "(co2 * density * cell-volume)") (syntax-tree ("*" ("*" "co2" "density") "cell-volume")) (code (field-* (field-* (field-load "co2") (field-load "density")) (field-load "cell-volume"))))
   ((name fuel-mass) (display "(c11h22o2 * density * cell-volume)") (syntax-tree ("*" ("*" "c11h22o2" "density") "cell-volume")) (code (field-* (field-* (field-load "c11h22o2") (field-load "density")) (field-load "cell-volume"))))
   ((name no-mass) (display "(mf-pollut-pollutant-0 * density * cell-volume)") (syntax-tree ("*" ("*" "mf-pollut-pollutant-0" "density") "cell-volume")) (code (field-* (field-* (field-load "mf-pollut-pollutant-0") (field-load "density")) (field-load "cell-volume"))))
   ((name pm-mass) (display "soot-mass-fraction * cell-volume * density") (syntax-tree ("*" ("*" "soot-mass-fraction" "cell-volume") "density")) (code (field-* (field-* (field-load "soot-mass-fraction") (field-load "cell-volume")) (field-load "density"))))
   ((name soot-mass) (display "cell-volume * density * soot-mass-fraction") (syntax-tree ("*" ("*" "cell-volume" "density") "soot-mass-fraction")) (code (field-* (field-* (field-load "cell-volume") (field-load "density")) (field-load "soot-mass-fraction"))))
   ((name d-mass) (display "c10h22 * density * cell-volume") (syntax-tree ("*" ("*" "c10h22" "density") "cell-volume")) (code (field-* (field-* (field-load "c10h22") (field-load "density")) (field-load "cell-volume"))))
   ((name nhep-mass) (display "c7h16 * density * cell-volume") (syntax-tree ("*" ("*" "c7h16" "density") "cell-volume")) (code (field-* (field-* (field-load "c7h16") (field-load "density")) (field-load "cell-volume"))))
   ))
```

# APPENDIX B

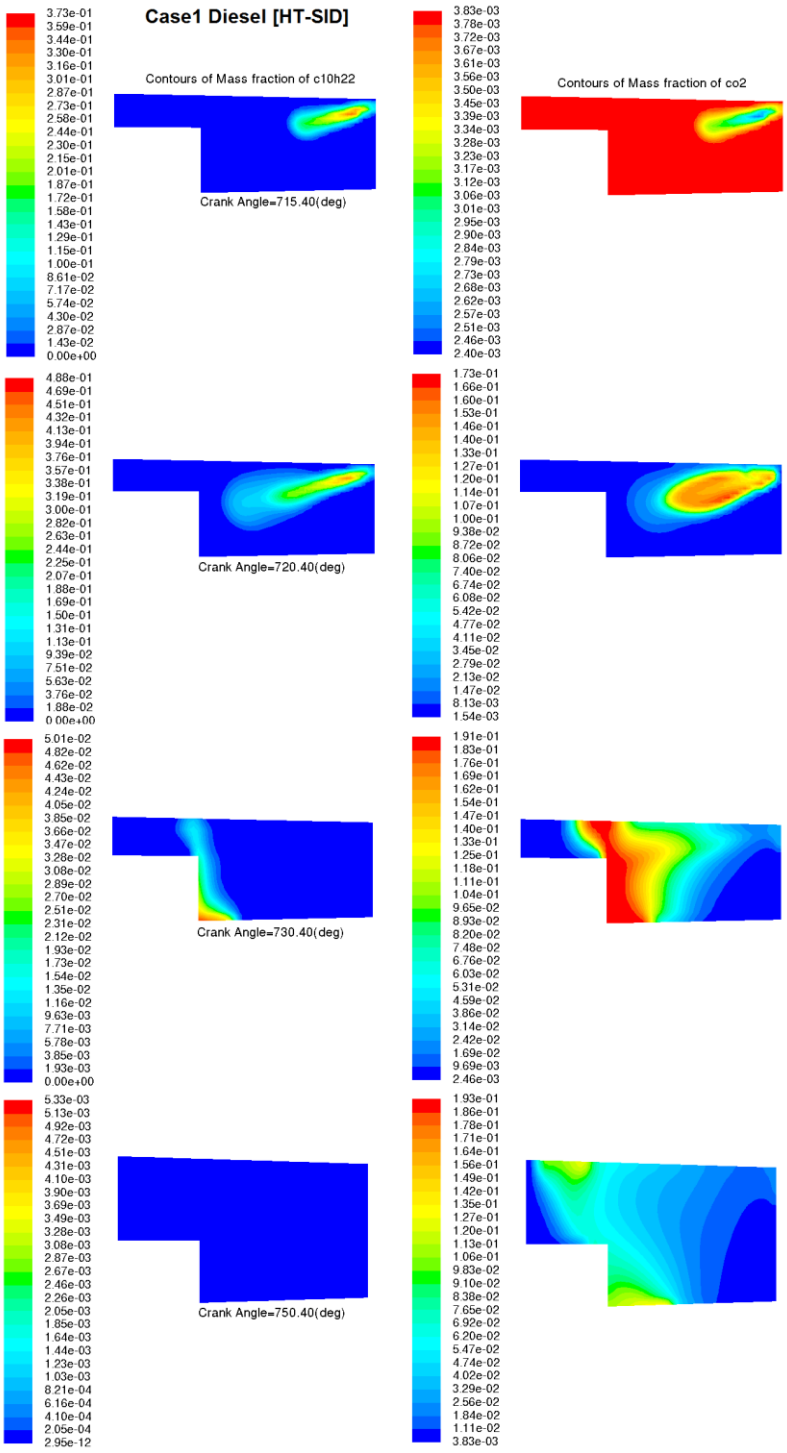


**Figure 36: Case 1 diesel fuel and oxocarbon mass fraction contours**

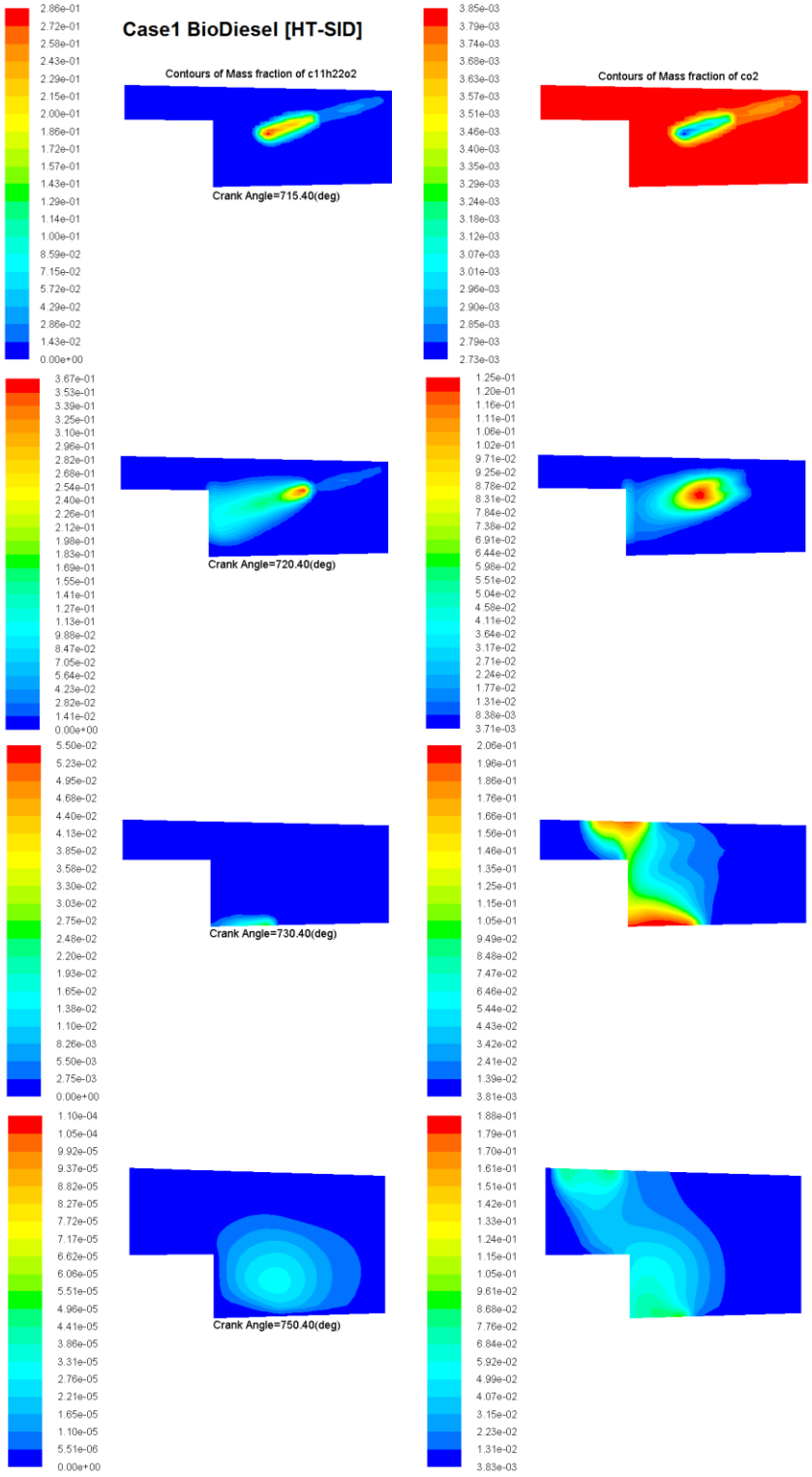


**Figure 37: Case 1 biodiesel fuel and oxocarbon mass fraction contours**

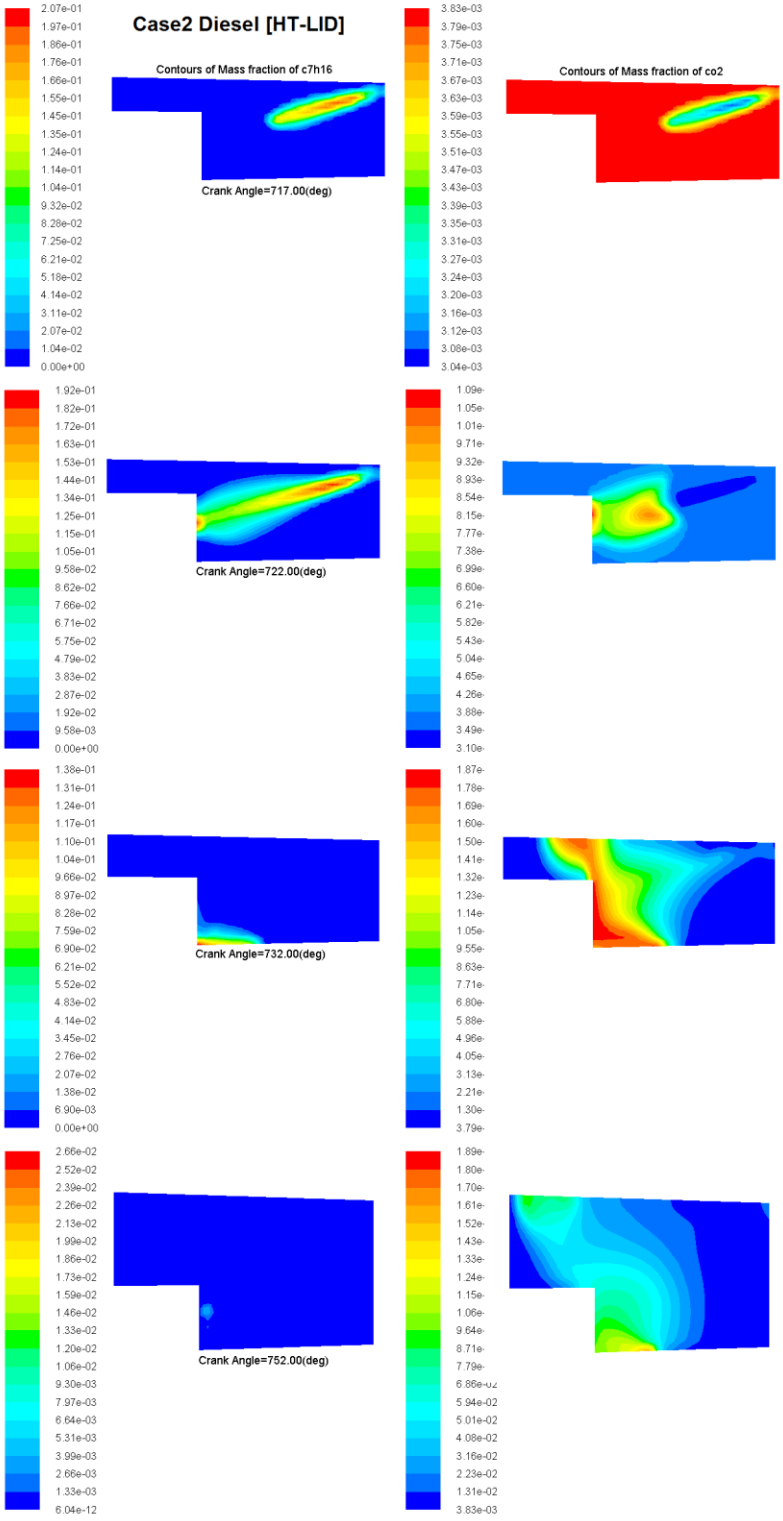


**Figure 38: Case 2 diesel fuel and oxocarbon mass fraction contours**

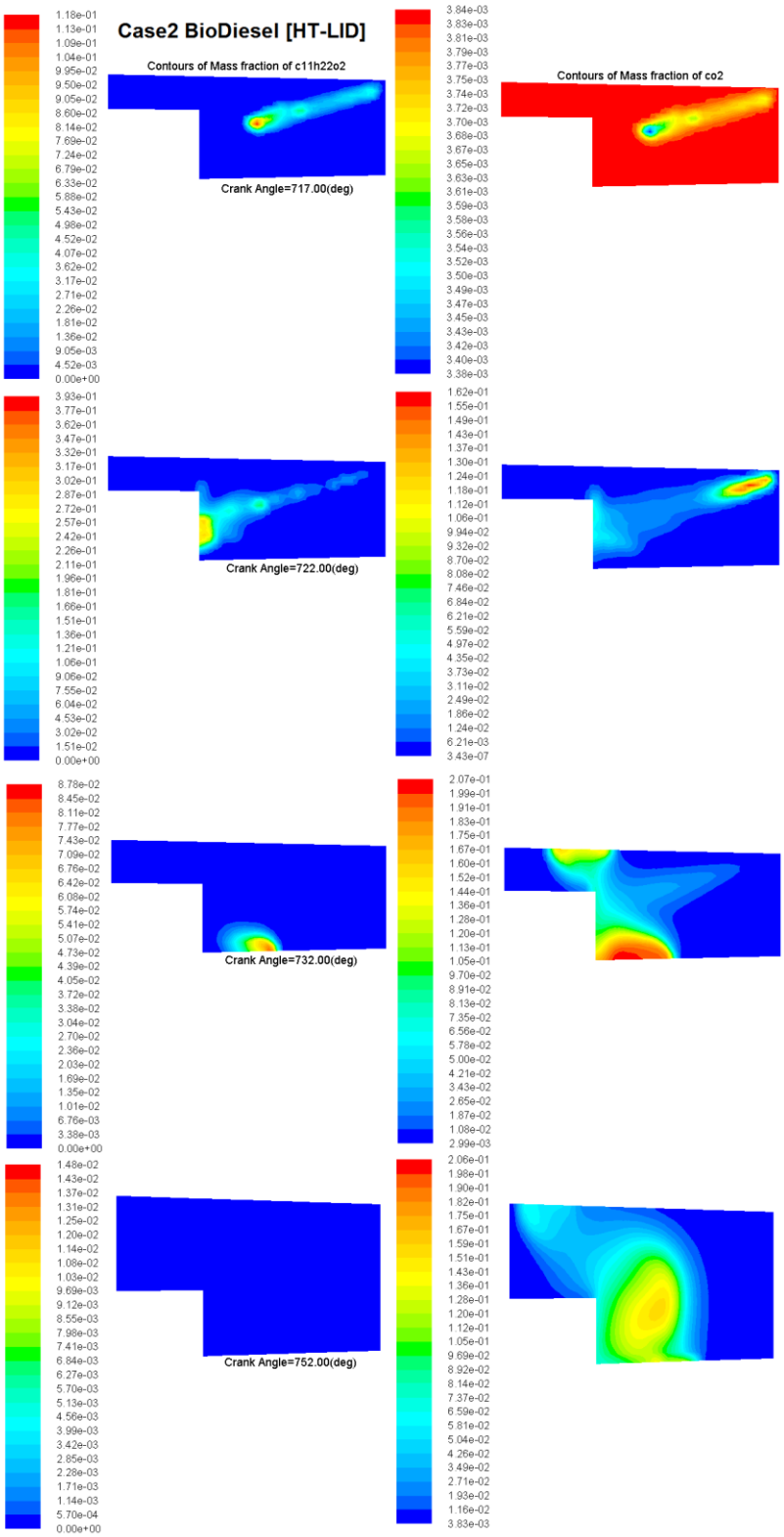


**Figure 39: Case 2 biodiesel fuel and oxocarbon mass fraction contours**

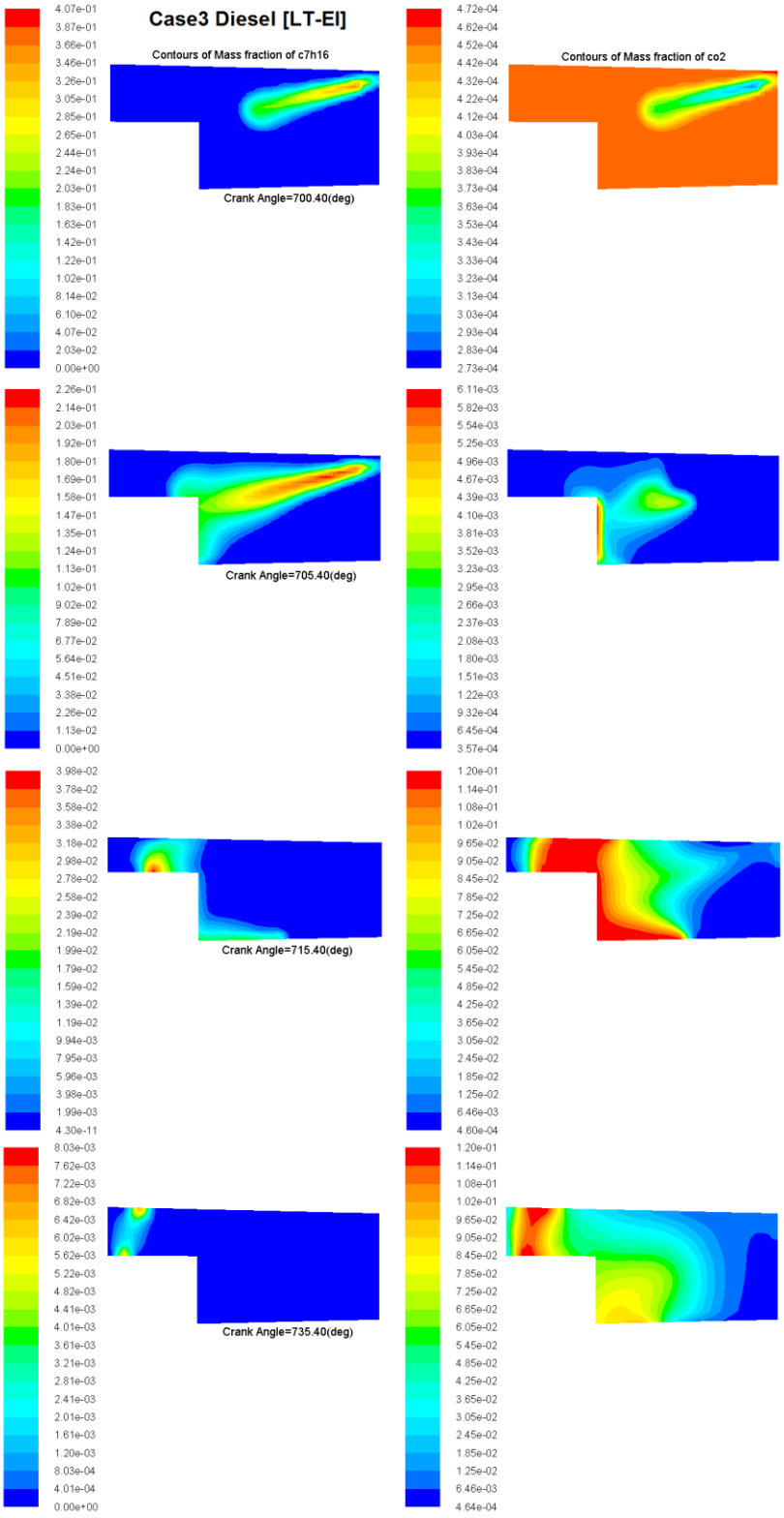


**Figure 40: Case 3 diesel fuel and oxocarbon mass fraction contours**

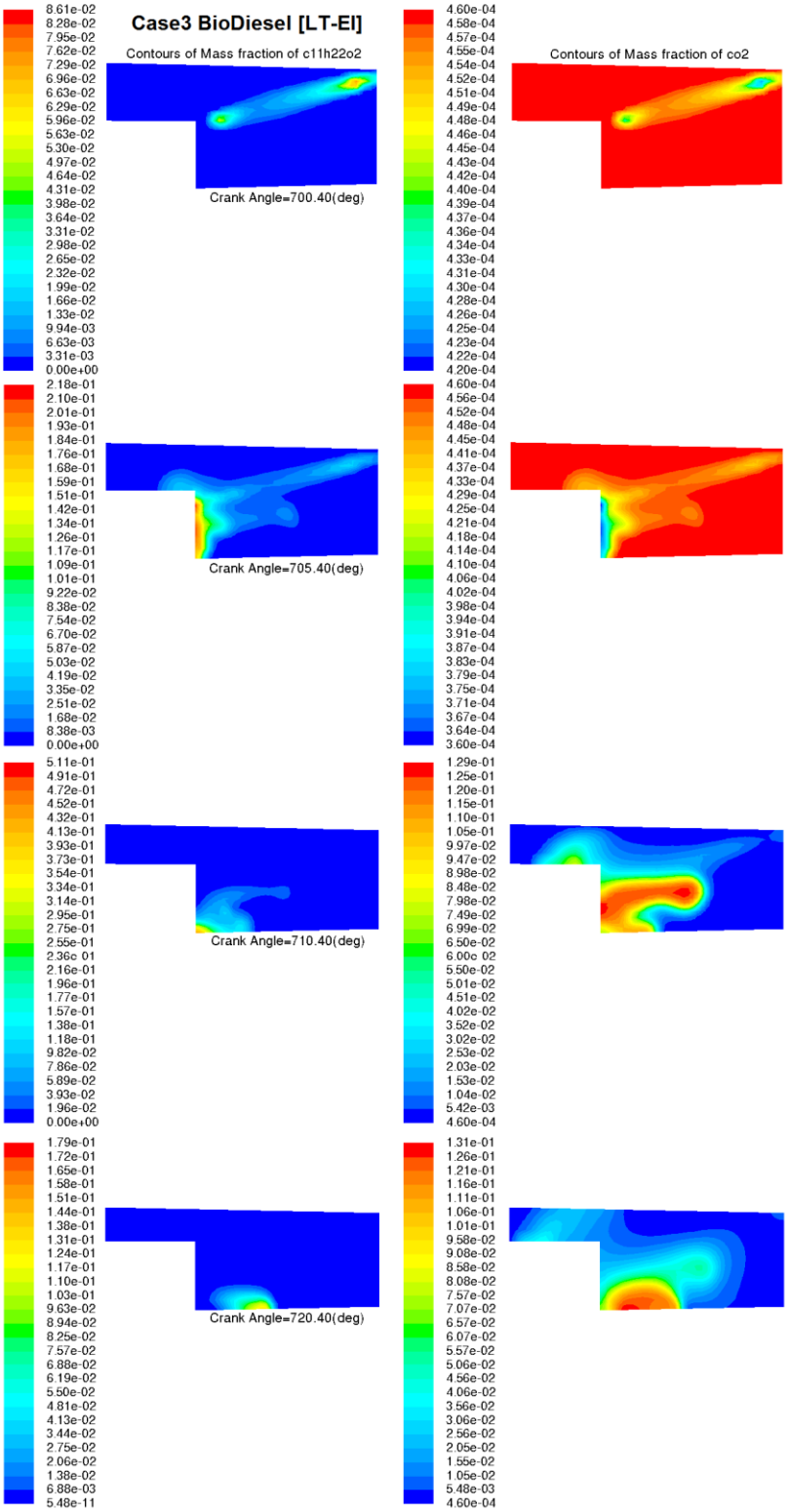


**Figure 41: Case 3 biodiesel fuel and oxocarbon mass fraction contours**

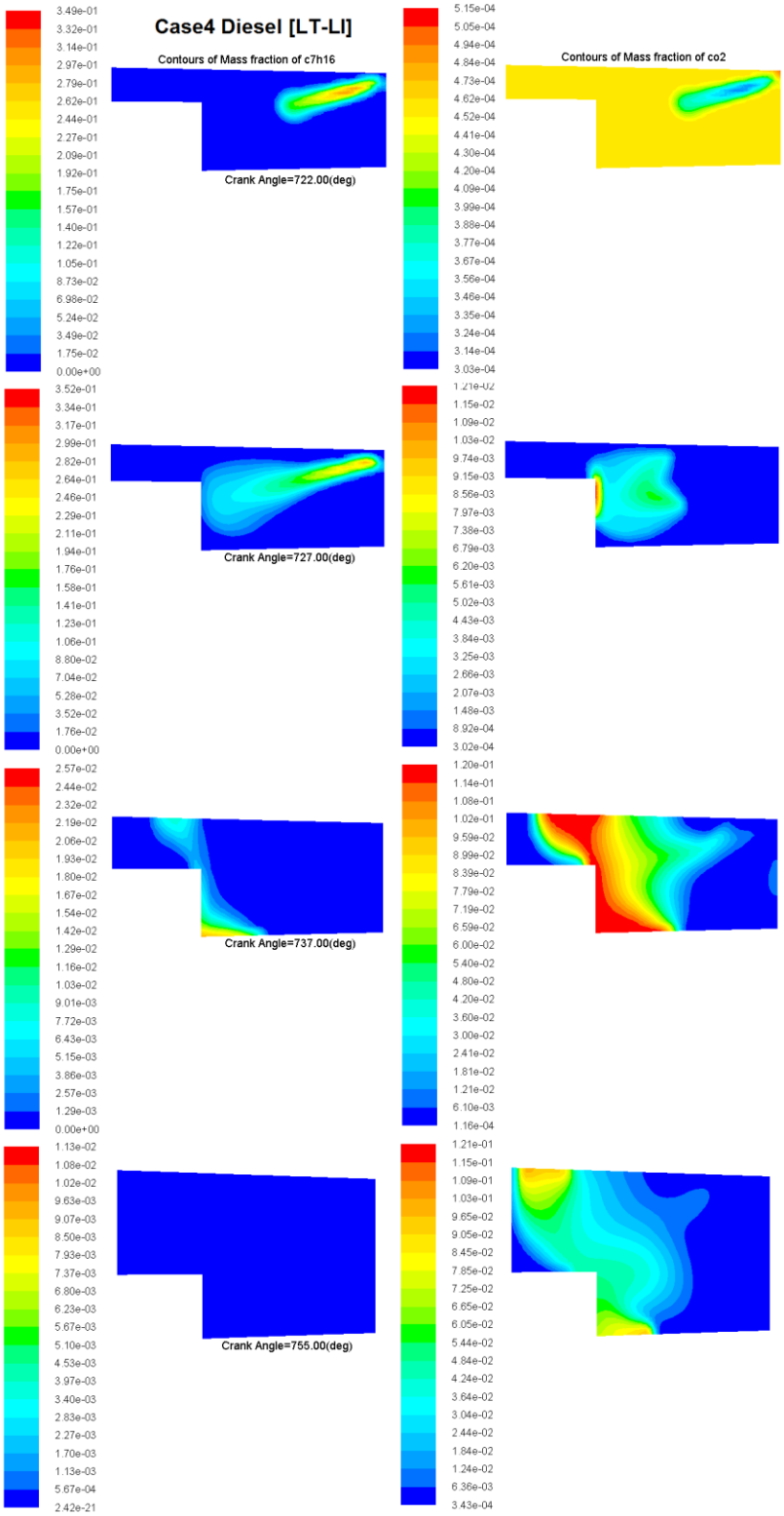


**Figure 42: Case 4 diesel fuel and oxocarbon mass fraction contours**

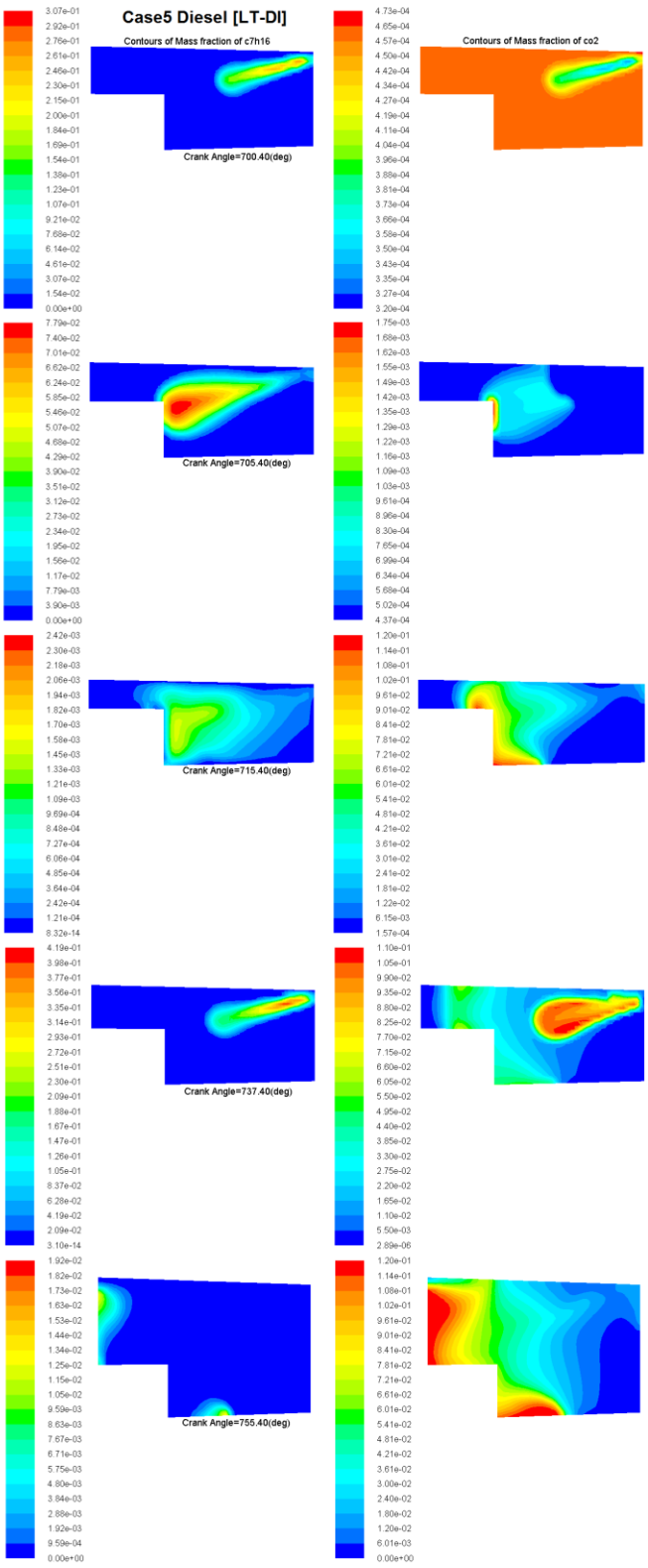


**Figure 43: Case 5 diesel fuel and oxocarbon mass fraction contours**

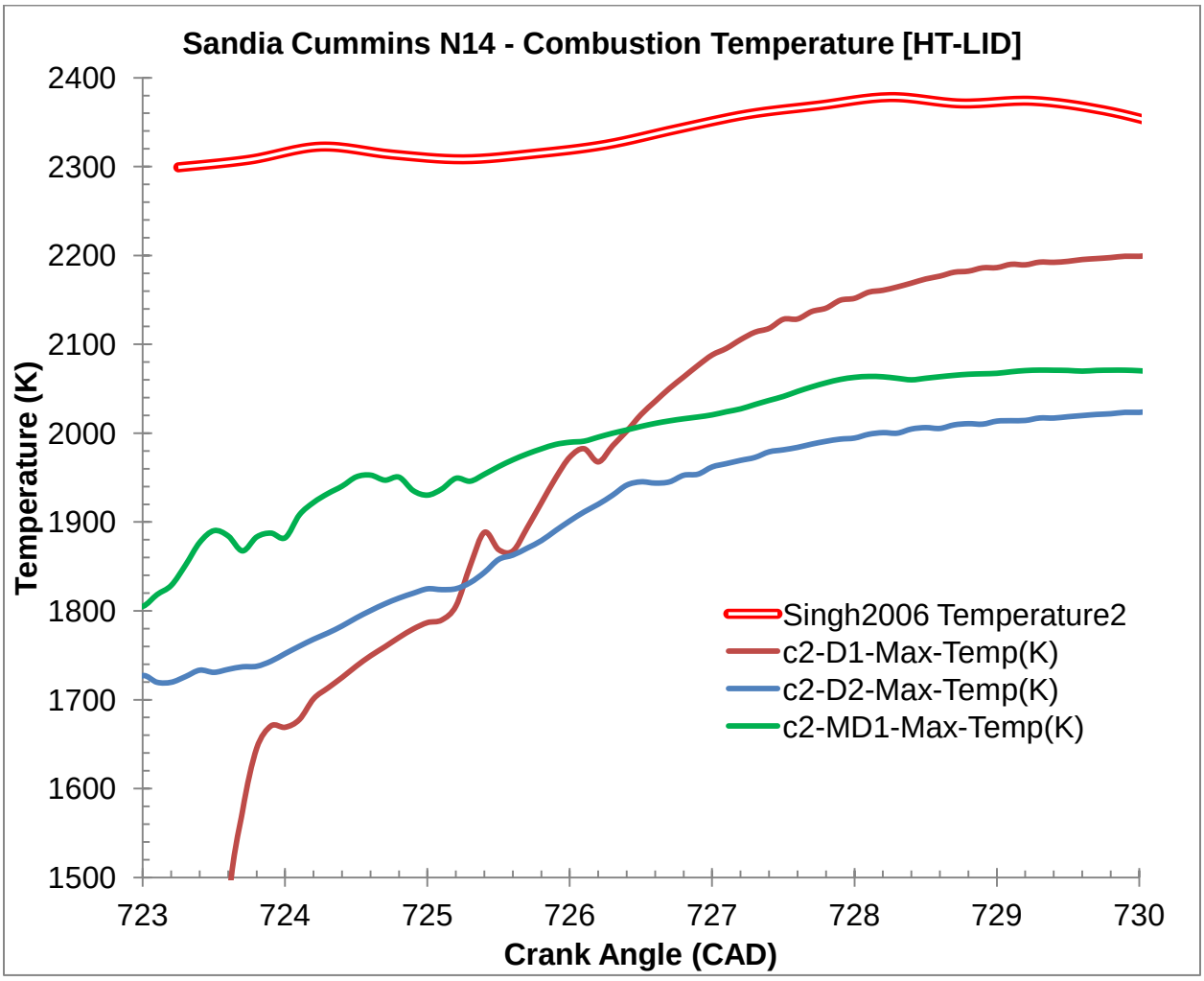


**Figure 44: Case 2, High-temperature, long ignition delay temperature curves**

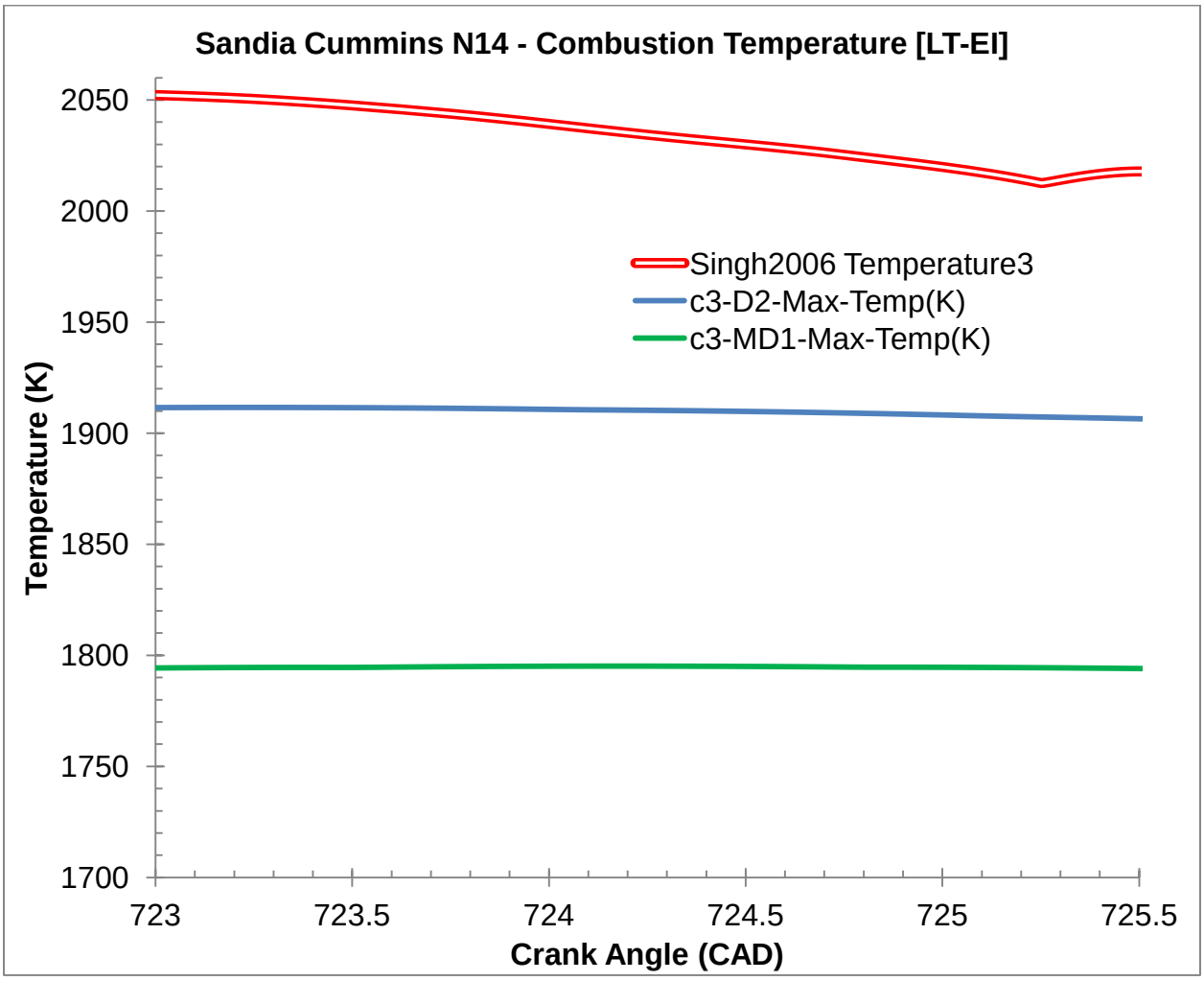


**Figure 45: Case 3, Low-temperature, early injection temperature curves**

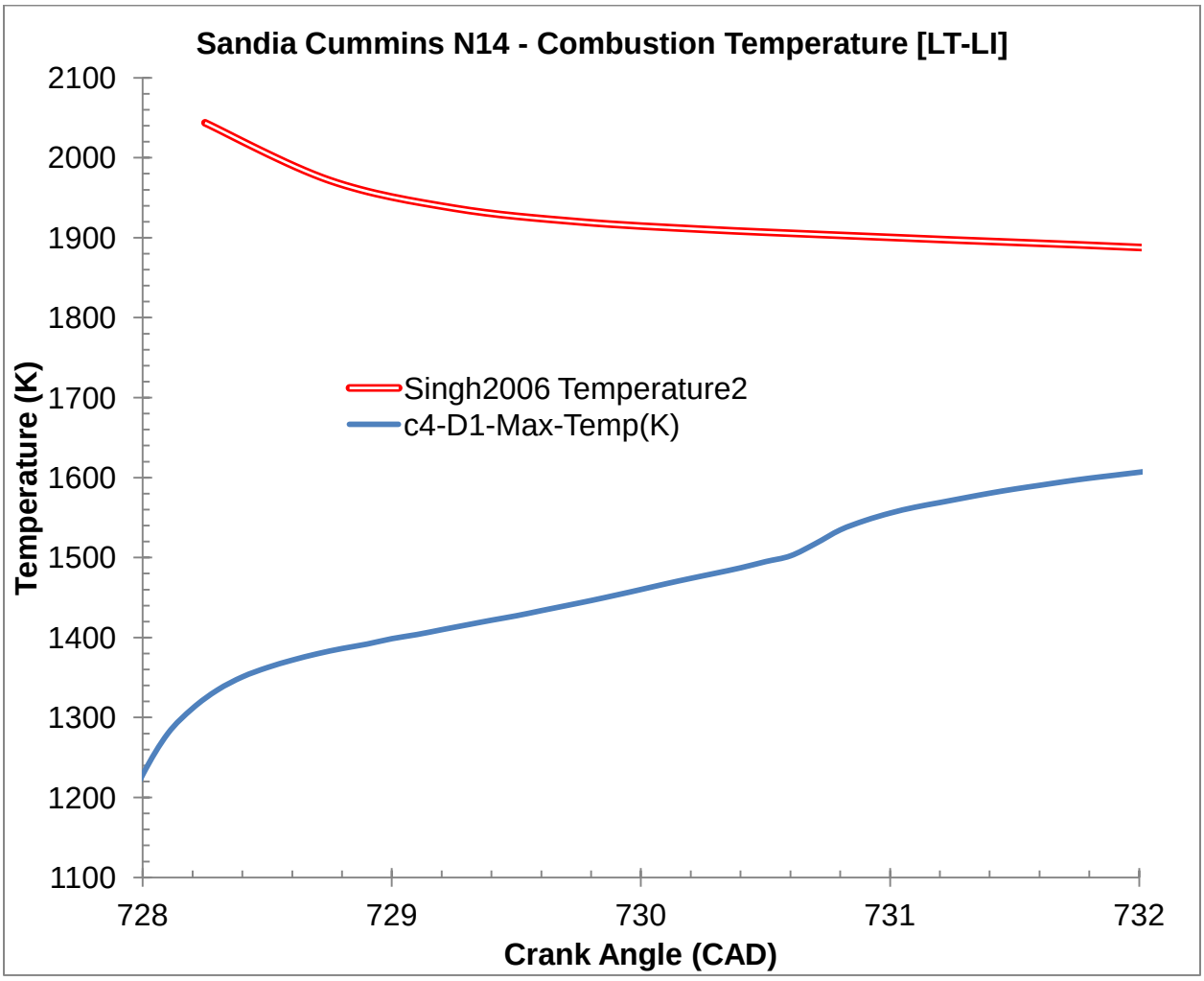


**Figure 46: Case 4, High-temperature, late injection temperature curves**

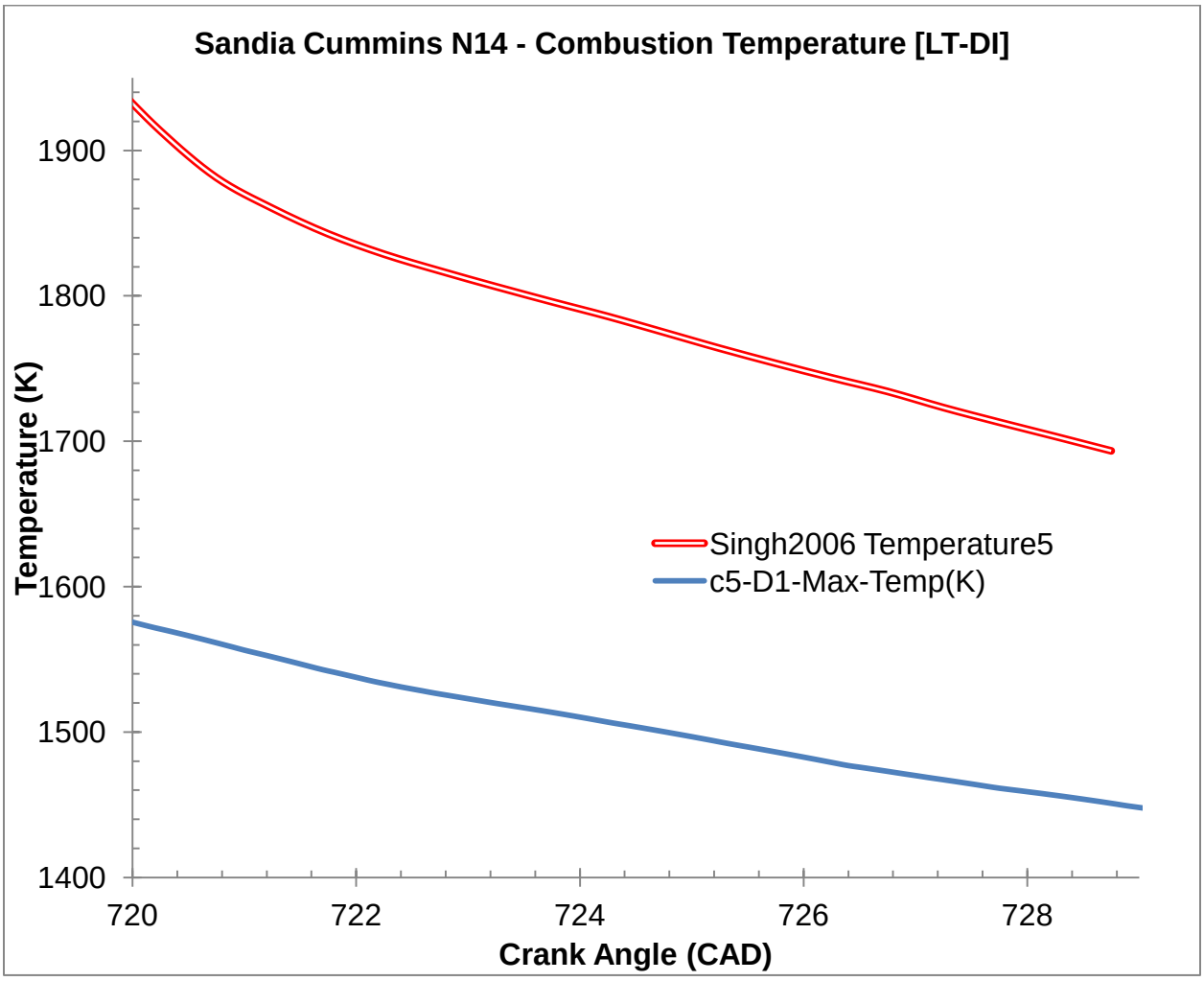


**Figure 47: Case 5, High-temperature, double injection temperature curves**

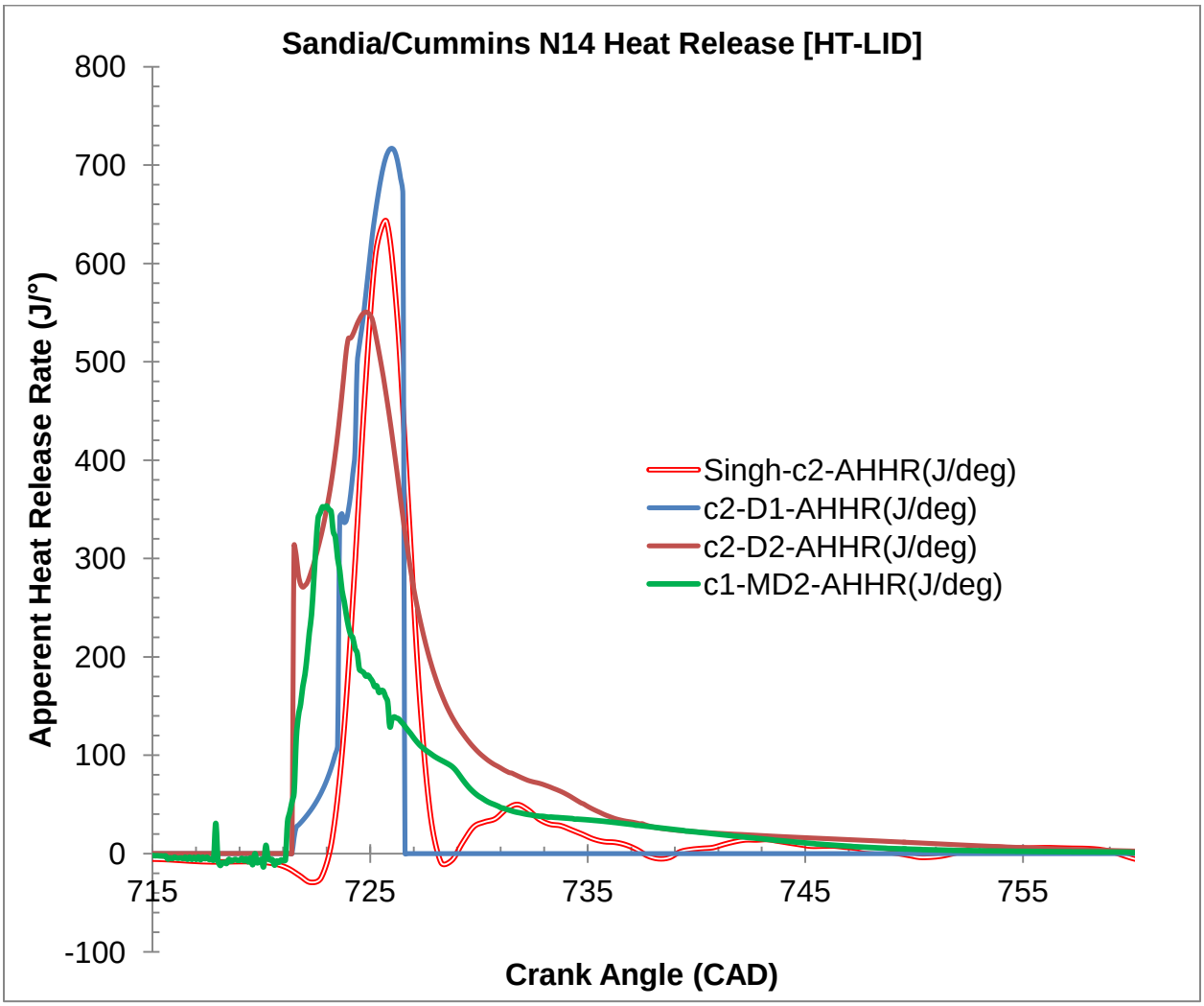


**Figure 48: Case 2, High-temperature, long ignition delay heat release curves**

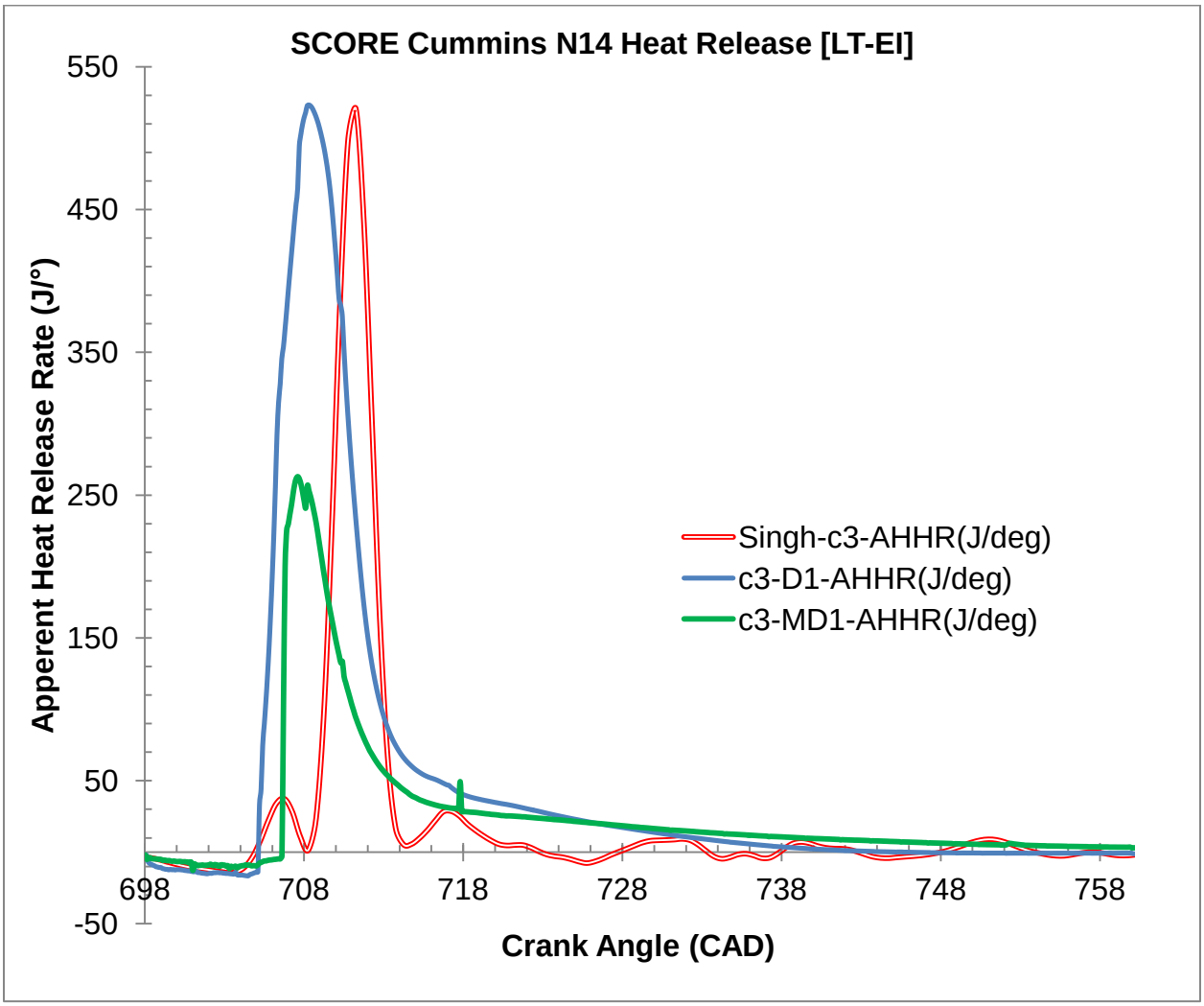


**Figure 49: Case 3, Low-temperature, early injection heat release curves**

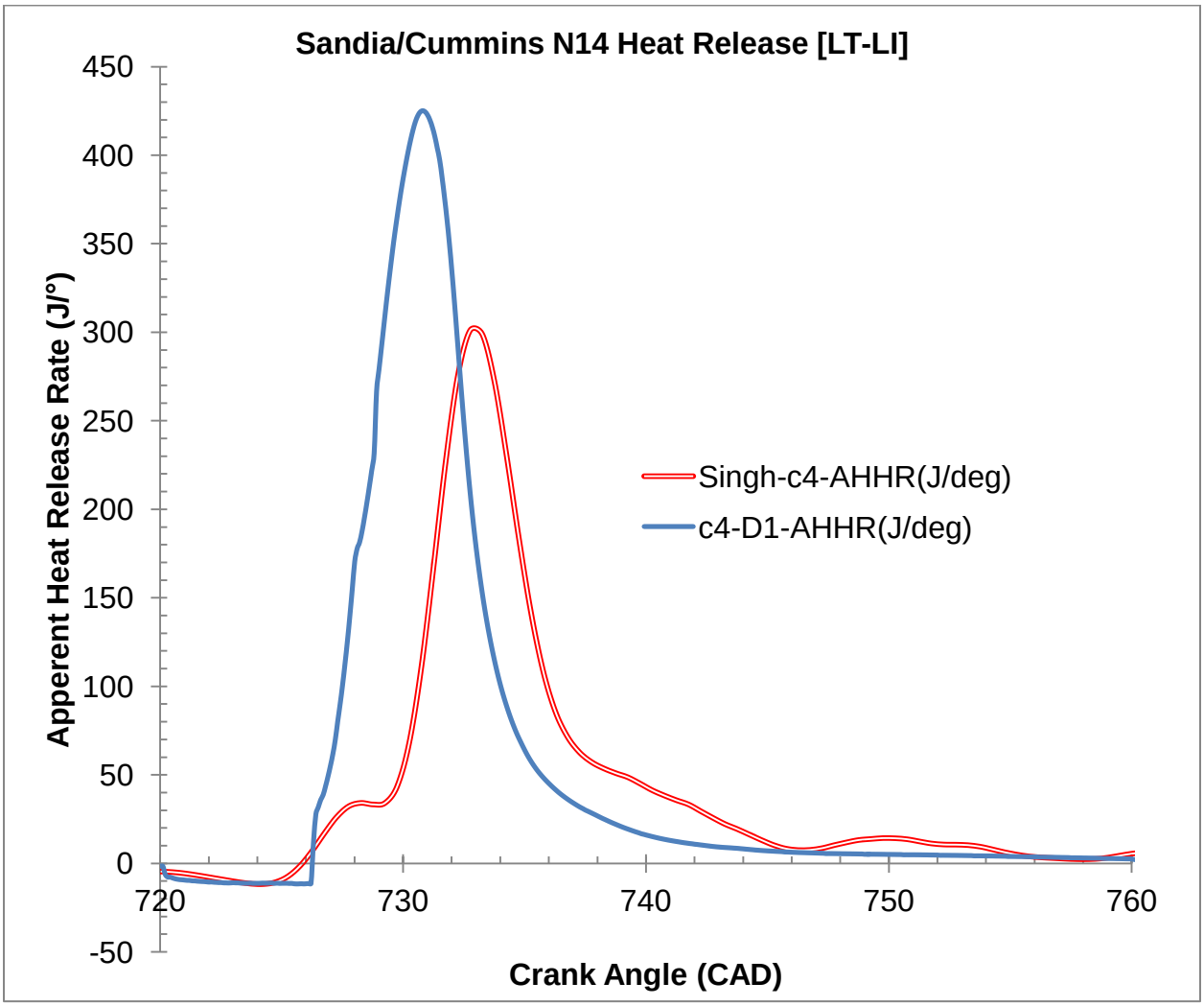


**Figure 50: Case 4, Low-temperature, late injection heat release curves**

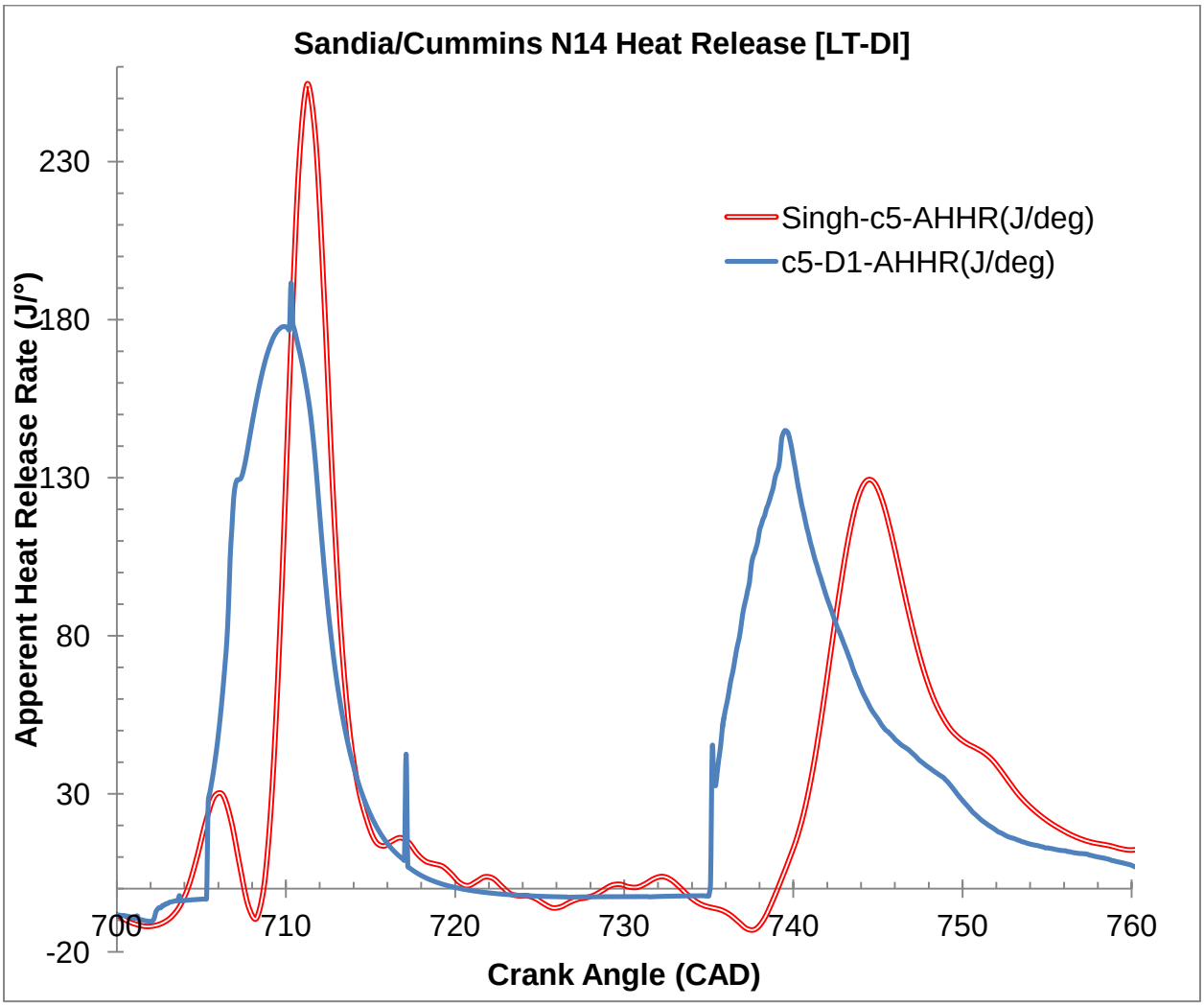


**Figure 51: Case 5, Low-temperature, double injection heat release curves**